INFORMATION TO USERS

This manuscript has been reproduced from the microfilm master. UMI films the text directly from the original or copy submitted. Thus, some thesis and dissertation copies are in typewriter face, while others may be from any type of computer printer.

The quality of this reproduction is dependent upon the quality of the copy submitted. Broken or indistinct print, colored or poor quality illustrations and photographs, print bleedthrough, substandard margins, and improper alignment can adversely affect reproduction.

In the unlikely event that the author did not send UMI a complete manuscript and there are missing pages, these will be noted. Also, if unauthorized copyright material had to be removed, a note will indicate the deletion.

Oversize materials (e.g., maps, drawings, charts) are reproduced by sectioning the original, beginning at the upper left-hand corner and continuing from left to right in equal sections with small overlaps. Each original is also photographed in one exposure and is included in reduced form at the back of the book.

Photographs included in the original manuscript have been reproduced xerographically in this copy. Higher quality 6" x 9" black and white photographic prints are available for any photographs or illustrations appearing in this copy for an additional charge. Contact UMI directly to order.

UMI

A Bell & Howell Information Company
300 North Zeeb Road, Ann Arbor MI 48106-1346 USA
313/761-4700 800/521-0600

SEISMICITY ANALYSIS: NEW TECHNIQUES AND CASE STUDIES

A

THESIS

Presented to the Faculty

of the University of Alaska Fairbanks

in Partial Fulfillment of the Requirements

for the Degree of

DOCTOR OF PHILOSOPHY

By

Stefan Wiemer, Dipl. Geophys.

Fairbanks, Alaska

December 1996

SEISMICITY ANALYSIS: NEW TECHNIQUES AND CASE STUDIES

By

Stefan Wiemer

RECOMMENDED:

Dr. Douglas Christensen

Dr. Stephen R. McNutt

Dr. Hans Pulpan

Dr. Max Wyss, Advisory Committee Chair

Dr. Paul Layer, Head
Department of Geology and Geophysics

APPROVED:

Dr. Paul Reichardt, Dean, College of Science, Engineering and Mathematics

Dr. Joseph Kan, Dean of the Graduate School

11-26-96

Date

Abstract

Seismicity parameters can be visualized as an almost continuous function of space and time by using dense grids. This mapping technique is used to: (1) Study the seismic quiescence preceding the 1992 Landers earthquake sequence. Both the Landers and Big Bear earthquake were found to be preceded by periods of significant seismic quiescence lasting 2-4 years. (2) Image the frequency-magnitude distribution in the subducting slab underneath Alaska and New Zealand. A high b-value anomaly at 100 km depth on the top of the slab suggests that slab dehydration causes an increase in the pore pressure. (3) Investigate the plumbing system of Mt. St. Helens and Mt. Spurr. This study suggests that the detailed spatial mapping of the frequency-magnitude distribution is potentially capable of resolving the location of magma chambers and the depth of vesiculation underneath volcanoes. (4) Map out the spatial distribution of asperities along the San Andreas fault in California. Based on the observation that the Parkfield and Morgan Hill asperities show an extremely low b-value (b<0.5), a new model to calculate recurrence times for moderate size earthquakes is proposed. (5) Investigate the correlation between a currently observed period of seismic quiescence in the Tokyo region and the frequency-magnitude distribution. A modification to the seismic quiescence hypothesis is proposed, which uses the frequency-magnitude distribution as a tool to distinguish between precursory seismic quiescence and false alarms not followed by a main shock.

All of these case studies show that applying these new tools in seismicity analyses can advance the understanding of a variety of complex and heterogeneous tectonic regimes in the seismogenic part of the earth's crust and upper mantle.

Table of Contents

List of Figures

List of Tables

Acknowledgments

A number of people, both scientists and friends, have contributed in different ways to the writing of this thesis. First of all I would like to thank my advisor, Max Wyss, who probably was the best advisor I could have wished for. His encouragement, enthusiasm, criticism, deep understanding of science and especially his unmatched support for his students have made a lasting impression on me. I also would like to thank the other members of my committee: Douglas Christensen, Steve McNutt, and Hans Pulpan. They never failed to give advice and support, and I have learned from all of them.

I was fortunate to be part of an inspiring group of students, in seismology and beyond, that helped to make my Ph.D program in Alaska a lifetime experience. Dominique Gillard, John Benoit and Zhong Lu helped me with numerous problems and we spend many hours discussing scientific questions. Ramon Zúñiga and Alexander Allmann shared my interest in ZMAP, and wrote a part of the code. Thanks also to all friends inside and outside the Geophysical Institute. And, of course, to Hilary Fletcher.

Chapter 1. Introduction

1.1 Seismicity studies

Humans have searched for patterns in the occurrence of earthquakes for millennia. Although divine powers were generally thought to be the cause of earthquakes throughout most of history, there has always been the attempt to understand and ultimately to predict the occurrence of hazardous earthquakes. Earthquake catalogs in their most primitive form were created shortly after the invention of the written language. But only over the last 100 or so years, since seismic instruments have provided a tool to reliably locate and classify earthquakes, have earthquake catalogs become increasingly valuable. We have learned that earthquakes are more abundant in some regions than others. Plate tectonics has been identified as the driving force behind most of the earthquakes we experience. In the 1970's many people were optimistic about the future of earthquake prediction. The leading opinion was that within 25 years a reliable earthquake prediction method would be achieved. However, today in 1996 we seem to be further away from reaching this goal than ever. In the 1990's many seismologists believe that earthquake prediction is intrinsically impossible and studies of the seismicity cannot reveal new information about the rupture mechanics of earthquakes.

This thesis reports on recent progress made in quantitative seismicity analysis. This progress was in part made possible by two ongoing developments: 1) Progress in computer technology: fast and cheap computers permit the analysis of vast amounts of data in a short time. Data can be visualized and explored interactively and software development in general has become much easier and more efficient; 2) improved earthquake catalogs: Since the 1980's, the number of seismic stations has increased in many regions of the world, and along with the more widespread use of digital recording and high dynamic range stations this development has dramatically improved the quality and quantity of located earthquakes. Many earthquake catalogs are now complete down to smaller magnitudes. As a result we can now analyze seismicity in unprecedented detail. Several case studies are presented in this thesis, and more sophisticated analysis techniques are introduced which enable the investigation of the behavior of seismicity in multiple-dimensions (space, time and magnitude).

A number of publications have been inspired by the techniques described in this thesis. All of these studies use the software package ZMAP, and can be classified in several groups: 1) Studies investigating seismicity rate changes and the precursory seismic quiescence hypothesis (*Wiemer and Wyss*, 1994; *Wyss and Wiemer*, 1996ab; *Wyss et al.*, 1996b); 2) Studies focusing on catalog homogeneity and artificially introduced seismicity rate changes (*Zúñiga and Wyss*, 1995; *Zúñiga and Wiemer*, 1995); 3) Studies exploiting the capability of ZMAP to resolve and visualize variations of the frequency-magnitude distribution as a function of space (*Wiemer and Benoit*, 1996; *Wiemer and McNutt*, 1996; *Wiemer and Wyss*, 1996; *Wyss et al*, 1996a). 4) Studies investigating earthquake clustering (*Allmann*, 1996).

1.2 Overview of the chapters

This thesis is divided into six chapters, plus a general introduction, general conclusions, and one appendix. Five of these chapters have been published or submitted for publication (chapters 2, 4, 5, and 6). In this thesis, two different parameters that describe seismicity are investigated. In chapters two and three we investigate seismicity rate changes and the precursory seismic quiescence hypothesis. The next three chapters (4, 5, and 6) study the frequency-magnitude distribution in the crustal strike-slip regime of the San Andreas fault in California, the subduction zones of Alaska and New Zealand, and in the volcanic systems of Mt. St. Helens (Washington) and Mt. Spurr (Alaska). In chapter 7 we combine the results from both the study of the frequency-magnitude distribution and the precursory seismic quiescence hypothesis.

Chapter 2 introduces the seismic quiescence hypothesis and explores the hypothesis for the 1992 Landers earthquake sequence that occurred in California. We show that precursory seismic quiescence did exist in the 2-4 years prior to the Landers and Big Bear main shocks, but not prior to the Joshua Tree main shock. The technique presented in Chapter 2 to investigate seismicity rate changes is a significant improvement over previous seismic quiescence studies (such as *Wyss and Burford*, 1987; *Wyss and Fu*, 1989; *Reasenberg and Matthews*, 1988; *Kisslinger*, 1988) in that it uses a grid approach to investigate all of space-time for anomalies. By placing a dense grid over the area to be investigated and sampling the N closest earthquakes to each grid-point, we have introduced a more objective approach to seismicity analysis. The same spatial gridding technique will be used in the following chapters and in essence represents the backbone of the advanced seis-

micity analysis techniques presented.

Chapter three will give some additional insight into the precursory seismic quiescence prior to the Landers earthquake sequence. The extent of the quiescent volume is mapped in more detail by using vertical cross-sections along and across the strike of the fault. The correlation of the quiescent patches on the fault and the areas of high moment release during the ruptures allows us to draw some conclusions about the physical mechanism that causes the precursory phenomena. In addition, we will introduce the alarm cube method, a technique to identify all periods of decreased seismicity above a given significance threshold.

The next chapter (Chapter 4) investigates the frequency-magnitude distribution in the subduction zones of Alaska and New Zealand. We will show that, by using high quality, regional earthquake catalogs combined with high resolution gridding techniques, a high *b*-value anomaly at the top of the subducting slab at a depth of about 100 km can be identified. This anomaly directly underlies the volcanic arc and may thus be associated with the mechanism that creates arc-like volcanism on the surface.

In chapter five we take a closer look at the frequency-magnitude distribution within two volcanic regions: Mt. St. Helens (Washington) and Mt. Spurr (Alaska). We document that for these two volcanoes the location of high *b*-value anomalies appears to correlate with the locations of magma chambers and with the depth of magma vesiculation. This result suggests that the frequency-magnitude distribution contains important information about the plumbing system of volcanoes.

Chapter six takes us back to California, where we investigate the frequency-magnitude distribution in asperities. For two asperities in Central California (Parkfield and Morgan Hill) we find that these asperities (hard spots on the fault) stand out as the patches with the lowest *b*-values (b~0.5). The observed strong differences in the frequency-magnitude distribution with depth and along the strike of the fault lead us to suggest a new model to explain the recurrence time of moderate to large earthquakes.

Finally, chapter seven makes an attempt to combine the information contained in the two seismicity parameters investigated in chapters 2-6. We propose that we can use the frequency-magnitude distribution to estimate the probability that an observed seismic quiescence is a precursor to a

large earthquake. If indeed, as proposed in chapter 6, large earthquakes have a higher probability of occurring in low *b*-value volumes, then a quiescence observed in a high *b*-value volume should be less likely to be a precursor than a quiescence observed in a low *b*-value region. This hypothesis is so far supported by little data, and additional case studies are necessary to draw more definitive conclusions.

Chapter eight presents general conclusions, along with suggestions for future research. Lastly, appendix A gives a short description of ZMAP, the software developed to do most of the analyses.

1.3 References

Allmann, A. (1996). Characteristics of clustered seismicity in Alaska, Diplomarbeit, University Munich.

Habermann, R.E. (1982). Consistency of teleseismic reporting since 1963, Bull. Seism. Soc. Am, 72, 93-112.

Habermann, R.E. (1983). Teleseismic detection in the Aleutian Islands arc, J. Geophys. Res., 88, 5056-5064.

Habermann, R.E. (1987). Man-made changes of seismicity rates, Bull. Seism. Soc. Am., 77, 141-159.

Habermann, R.E. (1991). Seismicity rate variations and systematic changes in magnitudes in teleseismic catalogs, Tectonophysics, 193, 277-289.

Kisslinger, C. (1988). An experiment in earthquake prediction and the 7 May 1986 Andreanof Islands earthquake, Bull. Seism. Soc. Am., 78, 218-229.

Reasenberg, P.A., and M.V. Matthews (1988). Precursory seismic quiescence: A preliminary assessment of the hypothesis, PAGEOPH, 126, 373-406.

Wiemer, S., and J. Benoit (1996). Mapping the b-value anomaly at 100 km depth in the Alaska and New Zealand subduction zones, Geophys. Res. Lett., 23, 1557-1560.

Wiemer, S. and M. Wyss; (1994). Seismic Quiescence before the 1993 M = 7.5 Landers and M = 6.5 Big Bear (California) earthquakes, Bull. Seism. Soc. Am., Vol. 84, No. 3, pp. 900-916.

Wiemer, S., and S. McNutt (1996). Variations in the magnitude-frequency distribution in two volcanic regions: Mt. St Helens (Washington) and Mt. Spurr (Alaska), Geophys. Res. Lett., in press.

Wiemer, S., and R. F. Zúñiga (1994). ZMAP - a software package to analyze seismicity, EOS, Transactions, Fall Meeting, AGU, 75, 456.

Wyss, M. (1991). Reporting history of the central Aleutians seismograph network and the quiescence preceding the 1986 Andreanof Island earthquake, Bull. Seism. Soc. Am., 81, 1231-1254.

Wyss, M., and R.O. Burford (1987). A predicted earthquake on the San Andreas fault, California, Nature, 329, 323-325.

Wyss, M. and Z-X. Fu (1989). Precursory seismic quiescence before the January 1982 Hilea, Hawaii, earthquake, Bull. Seism. Soc. Am., 79, 756-773.

Wyss, M. and S. Wiemer (1996a). Two Precursory Seismic Quiescences near Priest Valley, California, Bull. Seism. Soc. Am., in review.

Wyss, M. and S. Wiemer (1996b): Two current seismic quiescences within 40 km of Tokyo, Geophy. J. Intern., in press.

Wyss, M., K. Shimazaki, and S. Wiemer (1996a). Maping active magma chambers by b-values, J. Geophys. Res., in preparation.

Wyss, M., S. Wiemer, and S. Tsuboi (1996b). Magnitude distribution anomalies in the WBZ beneath Japan, J. Geophys. Res., in preparation.

Zúñiga, F.R. and S. Wiemer (1995). Variaciones artificiales de sismicidad y su aplicacion. Algunos ejemplos en Mexico. In "La Sismologia en Mexico", Monograph No.2, Union Geofisica Mexicana. F. Medina, G. Suarez and L. Delgado, editors, pp 100-110.

Zúñiga, F.R., and M. Wyss (1995). Inadvertent changes in magnitude reported in earthquake catalogs: Influence on b-value estimates, Bull. Seism. Soc. Am., 85, 1858-1866.

Chapter 2. Seismic Quiescence before the Landers (M = 7.5) and Big Bear (M = 6.5) 1992 Earthquakes[1]

2.1 Abstract

The Landers earthquake of 28 June 1992 was preceded by a seismicity rate decrease of 75% in a volume approximately 11 km x 23 km x 15 km, located adjacent to and north of the epicenter. This anomaly started, for all magnitude bands, in January 1988, lasting 4.5 years up to the main-shock. A smaller volume (7x14x15 km), to the south of the epicenter, showed a seismicity rate decrease of 75% starting in November 1989. The Big Bear earthquake of the same day was preceded by a 100% decrease of the seismicity rate, within a volume of approximately 13 km x 22 km x 15 km around the hypocenter. This volume contained 192 earthquakes of M $\geq$1.6 during the background period of 9 years, but none during the 1.6 years from December 1990 to 27 June 1992. The standard deviate z-values characterizing these rate changes are very high, 6.3 and 12.3 respectively, and the anomalies are unique, not surpassed in significance by any other rate decrease in the portion of the southern California earthquake catalog examined (117° 06' W - 115° 40' W and 33° 45' N - 35° 10' N). No seismicity rate change was found in the vicinity of the M=6.1 Joshua Tree earthquake of 23 April 1992. Based on magnitude signatures and frequency-magnitude analyses, we conclude the two quiescence anomalies could not have been due to a shift or a compression of the magnitude scale, and we interpret them as precursor anomalies. This analysis was carried out using the declustered earthquake catalog for the Landers area with corrections of 0.2 and 0.1 (August 1985 and May 1990) for two suspected magnitude shifts. With a new visualization technique we can investigate the stability, and changes, of the seismicity rate as a function of time and space. By mapping z-values for rate changes at every time interval, and in volumes centered on a dense grid of points (lat., long.), this computer code furnishes an almost continuous sequence of smooth contour maps of the degree of rate changes. Any anomalies, artificial or real, may thus be defined accurately.

---

1. Wiemer, S. and M. Wyss; (1994): Seismic Quiescence before the 1993 M = 7.5 Landers and M = 6.5 Big Bear (California) earthquakes, *Bull. Seism. Soc. Am.*, Vol. 84, No. 3, pp. 900-916.

2.2 Introduction

The Landers 28 June 1992 M_s = 7.5 earthquake, together with the Big Bear M_s = 6.5 'after-shock' on the same day and the M = 6.1 Joshua Tree earthquake on April 23, represents the most extensive and well recorded sequence of major seimicity in southern California (*Hauksson et al.* 1992; various articles in this volume). The right lateral slip on the 85 km long fault (Figure 2.1) was typically 2-5 m (*Hauksson et al.*, 1992). This sequence of events provided an opportunity to test the seismic quiescence hypothesis on three large earthquakes in the same area. The earthquakes ruptured different faults and therefore might show independent precursory quiescence. They occurred within an area less than 100 km x 100 km, which is small enough for studying seismicity patterns using a single catalog.

We define the precursory quiescence hypothesis in the following way (*Wyss*, 1986a; *Wyss and Habermann*, 1988a): a statistically significant decrease of the seismicity rate that occurs in a restricted segment of a seismogenic zone. The rate decrease is terminated by a mainshock and the quiescent volume covers all or a major parts of the source volume. Previous case studies (*Wyss and Burford*, 1985, 1987; *Wyss*, 1986a; *Wyss and Habermann*, 1988b; *Wyss and Fu*, 1989) show typically a decrease in the seismicity rate of 50-70%, with anomaly durations of one to several years. The rate decrease should be present in all magnitude bands above the minimum magnitude useful for analysis, otherwise it is suspected that the anomaly may be artificial. It has also been proposed that the quiescence may be restricted to the larger magnitudes of the background activity (e.g. *Cao and Aki*, 1987). The 1982 M = 5.0 Stone Canyon earthquake was actually predicted based on seismic quiescence prior to the mainshock (*Wyss and Burford*, 1985, 1987). Nevertheless the quiescence hypothesis seems to be applicable only to some and not all mainshocks. For example the Loma Prieta earthquake was apparently not preceded by quiescence. Little is known about the physical processes leading to quiescence, although reasonable models have been proposed (see for example *Scholz et al.*, 1973; *Scholz*, 1988; *Rudnicki*, 1988; *Stuart*, 1979, 1991).

We performed our analysis of seismicity patterns in the Landers and Big Bear areas in the following steps: (1) Investigate the catalog homogeneity in southern California. Decluster the catalog and identify significant rate changes that can be explained by magnitude shifts. Define the minimum magnitude of homogenous reporting. (2) Identify significant rate changes in the corrected

catalog. (3) Define anomalous volumes in space, time and magnitude band. (4) Investigate the nature of the rate change (artificial or natural). (5) Estimate the significance of anomalies.

2.3 Data

Our experience with earthquake catalogs from California, Hawaii, the Aleutians, Japan, Turkey, and the world suggests that the heterogeneity of earthquake catalogs is the greatest obstacle for identifying precursory seismic quiescence. The percentage of small earthquakes reported changes as a function of space and time. Changes in the number of stations reporting, the density of stations, the algorithm used to compute location and magnitude and, the number of workers available for routine processing have a noticeable impact on catalog homogeneity. The problem of heterogeneity of earthquake reporting, and methods to deal with it, has been studied extensively in the past (e.g. *Habermann*, 1981, 1982, 1983, 1986, 1987, 1988, 1991; *Perez and Scholz*, 1984; *Wyss and Habermann*, 1988b; *Wyss and Fu*, 1989; *Wyss and Burford*, 1985, 1987; *Wyss*, 1991; *Wyss et al.*, 1992). A shift in the magnitude can also change the number of events reported with M $\geq M_{min}$, and the introduction or removal of a single station in the network can lead to a significant shift in the reported magnitude (*Wyss*, 1991). A magnitude shift of -0.3, for example, would lead to an apparent seismicity rate decrease of 50%. A compression of the magnitude scale that was detected later, led to a false interpretation of the quiescence at Parkfield (*Wyss et al.*, 1990). We used the magnitude signature technique (*Habermann*, 1983; *Wyss and Habermann*, 1988a,b) together with the frequency-magnitude relationship to evaluate rate changes.

In this studywe used the southern California earthquake catalog provided by the California Institute of Technology for studying the seismicity rate in the area 17° 06' W - 115° 40' W and 33° 45' N - 35° 10' N from January 1975 to June 27 1992. To separate the dependent earthquakes (aftershocks and swarms) from the independent earthquakes, an algorithm by *Reasenberg* (1985) was used. The algorithm removes the clustered events and replaces them with one event with a magnitude equivalent to the total cluster. After declustering the catalog the significant rate changes in the catalog were identified using the computer code GENAS (*Habermann*, 1981). Fitting the observed magnitude signatures of these rate changes with a synthetic signature enabled us to determine the minimum magnitude of homogenous reporting (M_{min}) and to identify existing magnitude shifts (DM). This technique of calculating synthetic magnitude signatures and fitting them to the

observed signature is described in detail by *Habermann* (1981, 1983). The detection of seismic quiescence, and its definition in space and time, is best achieved if numerous earthquakes are available for the analysis and the investigated time series is as long as possible. Therefore, we were interested in including the smallest events which are reported homogeneously. M_{min} may be smaller than the smallest magnitude of complete reporting, provided that the percentage of reported events does not fluctuate as a function of time. There is usually a trade-off between a desirable length of the time series and a low M_{min}.

As a result of our investigation, we corrected the catalog for two suspected magnitude shifts. We applied corrections of: (1) +0.2 for all magnitudes between August 1985 and May 1990, and (2) +0.1 for all magnitudes after May 1990. These corrections cannot introduce seismic quiescence in the later part of the catalog, because both shifts increase the number of earthquakes above a magnitude threshold M_{min} in the recent part of the catalog, and therefore they work against quiescence before the Landers earthquake sequence. In addition we will verify that detected anomalies are present in the uncorrected catalog as well. After applying these corrections, we considered the reporting rate in the study area as relatively homogenous for magnitudes $M \geq 1.6$ beginning in March 1981. The declustered and shifted catalog we used for the further analysis contains 11.3 years of data with a total of 5655 earthquakes. The seismicity rate was sampled in 295 subsequent intervals of 14 days, and in 5396 overlapping volumes, containing 130 earthquakes each. Figure 2.1 shows the locations of all earthquakes in the corrected catalog.

2.4 Method

Different techniques have been used in the past to identify and describe seismic quiescence. Visual inspection of epicenter maps and time-distance plots were used by early investigators (e.g. *Mogi*, 1969; *Ohtake et al.*, 1977; *Kanamori*, 1981). *Habermann* (1981, 1982, 1983) designed a number of algorithms to investigate quiescence quantitatively, based on the standard deviate z-test. *Reasenberg and Matthews* (1988) used the b-statistic to investigate the seismicity from a depth of 0 to 20 km in a circular region centered on the epicenter location. The radii r of the circles ranged from 2.0 to 15 km and were a function of magnitude of the mainshock. *Habermann* (1988) and *Wyss* (1986a, 1993) argued that circles do not take into account the known location and shape of the mainshock source. They might contain areas showing quiescence, as well as areas outside the

source-volume without quiescence. In the volumes surrounding the source an increase in activity is expected (e.g. *Mogi*, 1969; *Sykes and Jaume*, 1990) and thus it is not surprising that *Reasenberg and Matthews* did not find quiescence along the Calaveras fault. A study by *VonSeggern et al.* (1981) used 2 by 2 degree squares surrounding each mainshock. *Habermann* (1988) argued that averaging over such large areas introduces so much noise, that a possible signal cannot be detected. Wyss and Habermann in past studies used polygons reflecting the tectonic structure of the area (e.g. polygons aligned along the fault). The polygons were then divided into sub-polygons containing an equal number of earthquakes, therefore the size of the polygons was variable. A disadvantage of this method is the arbitrary location of the polygons, as their design and location might influence the results of the analysis. *Wyss* (1986a) constructed a randomly selected, non overlapping grid of rectangular cells over the area of the 1983 Kaoiki earthquake. The size of the grid-cells was constant while the number of earthquakes in each cell varied. He studied the seismicity rate changes in each cell and shifted the grid once by a vector half of the cell-size. This approach allowed him to approximately define areas of high and low seismic rate changes.

A new computer tool (ZMAP) to investigate and visualize seismicity rate changes in earthquake catalogs as a function of space and time was developed to improve the resolution of potential anomalies and to avoid the necessity of arbitrarily defining volumes for study. We defined a rectangular grid with a spacing of 2 km, which equals approximately the epicenter accuracy. With this new method rate changes will be resolved as an almost continuous function of space. For the Landers case this 2 km grid contains 5396 points. For a statistical analysis of seismicity rate changes it is more useful to consider areas of varying size with a constant number of earthquakes, instead of equal sized areas with a varying number of earthquakes. Therefore we selected for each grid-point (x,y) the N_i nearest epicenters from the catalog March 1981 to June 27 1992. These N_i earthquakes define, to a first approximation, a cylindrical volume of radius $r(N_i)$ with no depth constraint, where $r(N_i)$ is the maximum distance of an earthquake from the i-th grid-point. The value of r is a function of space and inversely proportional to the local density of earthquakes. Figure 2.2 shows examples for N_i = 130. An area with a higher density of earthquakes results in smaller cylinders than an area of low seismicity. In the northeast, where only few earthquakes are located (see Figure1), the circles in Figure 2.2 are significantly larger than in the central area. We use r as a measure of the spacial resolution of our method: the smaller r, the better the resolution.

The seismicity rate, sampled in two week intervals, can now be studied in each of these volumes. We applied several statistical functions designed for different purposes. Each of these functions calculates a z-value, a statistical measurement of the significance of a rate change at time t. This time t is then moved through the whole period of the catalog from March 1, 81 to June 27, 92. To identify significant rate changes prior to the Landers and Big Bear earthquakes we used the AS(t) function (*Habermann*, 1983, 1987, 1991). This function was designed to answer a very specific question: Where in time are the strongest single rate changes between two specific endpoints? In the past we have found the AS(t) function useful for the identification of an anomaly at the end of a time series, and for the identification of its onset-time. However, AS(t) is not capable of detecting anomalies when two or more rate changes occur in a time series. For an unbiased statistical test of the significance of an anomaly as well as to detect anomalies within a time series we used the LTA-function (Long Term Average: *Habermann*, 1988, 1991).

To visualize the changes of the seismicity we assigned each z-value a color, and plotted these at time t on a map (e.g. Figure 2.3). All grid-points (x,y) at time t define an image or contour plot (time slice), and we can visualize the change in the seismicity rate as a function of latitude and longitude for different times. In this representation, the z-value at one grid-point (x,y) corresponds to an integral over an area with a size inversely proportional to the local density of earthquakes. Since the volumes containing N_i earthquakes overlap, the z-values at two adjacent grid-points do not vary significantly, and for a specific time-slice t the z-values show a smooth variation over the map. This is especially true in low seismicity areas where neighboring volumes sample only a slightly changed subset of earthquakes. An additional interpolation was applied to smooth the images (*Wessel and Smith*, 1991). The size of an anomaly can not be judged directly by the size of an anomalous area on the map. A z-value is assigned only to each grid-point regardless of the size of the volume sampled and, thus, an anomaly represents only the center of the volume. The resolution could be increased by decreasing N_i, but there is a trade-off between resolution and significance: the smaller the number of earthquakes in each volume, the less significant are the observed rate changes.

Our new method to detect and present quiescence anomalies provides several advantages: (1) It gives a more precise location of the anomaly, as well as information about its extent and shape, possibly giving further insight into the physical processes leading to precursory seismic quies-

cence (e.g. *Scholz*, 1988). In addition, artificial seismicity rate changes can be detected, even when they occur only in a sub-area of the catalog under investigation. (2) The rather complex changes in the seimicity rate in an extended area can be visualized over the whole area at once. Possible patterns in seismicity rate changes (e.g. decrease in the source area and increase in surrounding areas) can be recognized. Because of the dense grid, with a spacing of the grid-points equal to or smaller than the average error in epicenter location, the change in the seimicity rate as a function of space can be understood as a continuum. (3) Through viewing several time-slices (as an animation) the investigator can easily and rapidly identify rate changes, their location and relative significance. A significant anomaly at any location in space, and occurring at any time, can be identified, therefore allowing detection of potential false alarms.

2.5 Results

The first objective of this study was to determine whether there was a significant rate decrease prior to the Landers or Big Bear earthquake. We used a grid-spacing of 2 km resulting in 5396 grid-points over the whole area of study. The minimum magnitude of the corrected catalog of the Landers area was $M_{min} = 1.6$ and we chose N_i, the number of earthquakes in each volume, equal to 130. We varied M_{min}, as well as N_i, to ensure that the results did not depend on the parameters used for the analysis. We applied the AS(t) function between the two endpoints t_0 = March 1, 1981 and t_e= June 27, 1992 to each of the volumes. The z-value at time t at each grid point was calculated using the following equation (*Habermann*, 1983):

$$z(t) = \frac{R_1 - R_2}{\sqrt{\frac{s_1^2}{n_1} + \frac{s_2^2}{n_2}}}$$

R_1 is the mean rate in period 1 (from t_0 to t), R_2 the mean rate in period 2 (from t to t_e), where t is the 'current' time ($t_0 < t < t_e$). s_1 and s_2 are the standard deviations in these periods, and n_1 and n_2 the number of samples. We assigned each z-value a color, and plotted these on a map for each time t. The maps of z-values were viewed stepping through time with a two week increment, to identify any outstanding anomalies that might occur at the end of the data set. The first significant rate change can be identified in January 1988. In the upper frame of Figure 2.3 one can easily identify high z-values (up to 6.5) in an area 10 km north of the epicenter, along the rupture of the 1992

Landers earthquake. High z-values signify a decrease in the seimicity rate. This anomaly is the most significant in this time slice, and precedes the Landers earthquake by 4.5 years. The anomaly is surrounded by much lower, even negative z-values, indicating an unchanged or increased seimicity rate in the surrounding volumes. The lower frame of Figure 2.3 shows typical background conditions: no significant anomaly exists in the time slice of March 1984. Proceeding in time, a second anomaly can be found in December 1990 (upper frame of Figure 2.4). This anomaly occurs precisely at the epicenter of the 1992 Big Bear earthquake, preceding the event by 1.6 years. Again this anomaly is the most significant in this time slice. The locations of the anomalies in Figures 2.2. 2.3 and 2.4 identify only the center of a seismicity decrease and do not map their true size. The lower frame in Figure 2.4 shows a view of the background condition at a time when the Landers anomaly begins to be noticeable in the AS(t) representation of the data, but no other significant rate decreases are present. Measured by the z-values of the AS(t) function, the two anomalies near the Landers and Big Bear epicenters are the most outstanding rate decreases in the entire catalog. Figure 2.5 shows time slices of the AS-function at 5 different times in a color representation. High z-values, indicating seimicity rate decreases, are visible as hot color spots in the last two time-slices, 4.5 and 1.6 years before the Landers and Big Bear earthquakes, respectively. No anomaly occurs in the vicinity of the April 1992 Joshua Tree earthquake. The cumulative number versus time plot, as well as the AS(t) function (Figure 2.6), show a stable seimicity rate, without significant changes in this area.This data set shows how remarkably constant the rate of earthquakes can be in some crustal volumes.

To obtain a more detailed view of the two anomalies, we reduced the grid spacing from 2 km to 1 km and decreased N_i from 130 to 50. We calculated the seismicity rate change, DR, in percent in each of these overlapping volumes. To map out the spacial extent of the anomaly, we did not only assign a value DR to the center of each volume, but to the whole area sampled. Where volumes overlapped, the maximum value (i.e. the highest seimicity rate decrease) was assigned. The upper frame of Figure 2.7 shows a contour-map of the seismicity rate decrease in the vicinity of the 1992 Landers epicenter comparing the periods March 81-January 88 and February 88-June 92. In an area 10 km north of the epicenter, on the eastern side of the fault the decrease is 93%. The size of the anomaly is approximately 23 km x 11 km. The optimized quiescence near the Landers epicenter is shown in the cumulative seismicity curves of Figure 2.8A. Comparing the period March 81- November 89 and December 89 to June 92 (lower frame in Figure 2.7) shows a second

area of high seismicity decrease (up to 88%) to the south of the Landers epicenter. The two lobes of decreased seismicity are interrupted by the epicenter region where foreshock activity was observed prior to the Landers earthquake (Figure 2.8 C and D).

The northern volume defined by the 75% decrease (upper frame of Figure 2.7) contained a total of 161 events with a magnitude $\geq$1.6. The onset of the quiescence is simultaneous in January 1988 for all M_{min} (Figure 2.8A). The change in the slope indicating the onset of the quiescence in January 1988 is sharp; before and after January 1988 the seismicity rates are approximately constant. These observations fit the description of other case-studies of precursory seismic quiescence (*Wyss*, 1986a; *Wyss and Habermann*, 1988a, b). In the epicenter volume a decrease in the seismicity rate occurs in late 1989, at the same time as in the southern lobe, but its significance is degraded because of the foreshocks and relatively large variations during the early record (Figure 2.8C).

The seismicity rate decrease before the Big Bear earthquake was even more dramatic. Figure 2.9 compares the rates before and after December 1990. Within a region of 20 km x 12 km the seismicity rate dropped by 100%. This area contains in total 192 earthquakes with M $\geq$1.6, none of which occurred after December 1990. Plots of the cumulative number of earthquakes versus time for the volumes with the 75% and 100% rate decrease are shown in Figure 2.10. The onset of the anomaly scores a z-value of the AS(t) function of 12.3, the highest z-value ever published for a seismic quiescence. Because we optimized the shape of the anomaly we cannot calculate the exact statistical significance of this z-value.

2.6 Discussion and Conclusions

After reinvestigation, several published cases of seismic quiescence turned out to be false alarms due to artificial rate changes in earthquakes catalogs (*Habermann*, 1987, 1988). In our understanding of precursory seismic quiescence it is not enough to only identify seismicity rate changes prior to a major earthquake. In addition, one has to show that this rate change is most likely natural, and that it is significant compared to other rate changes in the catalog.

To test whether the two observed anomalies are artificial or natural changes in the seismicity rate, we used the magnitude signature method as described by *Habermann* (1981, 1983, 1987, 1991) and frequency-magnitude plots. The magnitude signature method was successfully used to

identify artificial rate changes due to magnitude shifts in earthquake catalogs (*Wyss*, 1991), and the analysis of frequency-magnitude plots help to identify a stretching of the magnitude scale as a source of the rate change.

For these tests we used the anomalous volume defined by the 75% contour line for the Landers case (Figure 2.7). This area contains 268 earthquakes with M > 0 (Figure 2.11). The catalog used was declustered, no magnitude correction was applied. In Figure 2.11 the quiescence before the Landers earthquake is clearly visible, showing that we did not introduce the anomaly by the catalog corrections we applied. The periods compared by the magnitude signature technique were March 81 - December 87 and January 88 - June 92. Figure 2.12 shows positive standard deviate z-values in all magnitude bands, which are best modeled by postulating a uniform decrease of 60% in all magnitude bands. The observed 'umbrella shaped' magnitude signatures for both the Landers and Big Bear cases (Figure 2.12) show the pattern that one would expect for precursory quiescences (e.g. *Habermann*, 1991). Using the same catalog we compared the frequency-magnitude distribution during the anomalous period with that of the background period (Figure 2.13). The numbers during the anomalous time were normalized to the length of the background period. This presentation of the data shows that the rate decreased uniformly in all magnitude bands for which significant numbers of earthquakes are reported. A comparison of the Landers 1988 rate change with the artificial Parkfield rate changes present in the newly revised catalog in 1986 and 1991 shows that their characteristics are completely different. In the new Parkfield catalog the rate for all M > 0 earthquakes remained constant, while the rate for large events decreased and the rate of small events increased in 1986 (Figures 2.12 and 2.13). In 1991 a rate change with the opposite characteristics of the 1986 change occurred (the rate of large events increased and that of small events decreased), resulting in a magnitude signature symmetrical to the earlier one with respect to the z = 0 line (Figure 2.12). This means that a stretching of the magnitude scale in 1991 undid the effect of a compression of the scale in 1986. The Landers case (Figure 2.13) is different: the rates in all magnitude bands, including the total rate, decreased uniformly, with the b-value remaining approximately constant. A magnitude transformation cannot achieve the change in the Landers case.

The magnitude signature for the 1991 change in the Big Bear area (Figure 2.12) uses the 265 M > 0 earthquakes within the 100% contour line shown in Figure 2.9. The catalog was declustered

but no corrections were applied. The cumulative number versus time plot (Figure 2.14) shows a significant decrease of the seismicity rate for all earthquakes with M > 0. The magnitude signature for this case (Figure 2.12) is best modeled by a seismicity rate decrease of 50% in all magnitude bands. Because of the smaller number of earthquakes in the shorter anomalous period in the Big Bear case we do not calculate the normalized b-values. We conclude that magnitude signatures (Figure 2.12) and the frequency-magnitude plots (Figure 2.13) for the Landers and Big Bear rate changes support the hypothesis that these anomalies were due to precursory seismic quiescence, rather than to artificial changes in the catalog.

It has been suggested that the duration of precursory quiescence should increase with increasing magnitude of mainshock (e.g. *Kanamori*, 1981; *Scholz*, 1988). The data indicate that this may be so, but they are not conclusive. In Hawaii an increase of one in magnitude increases the duration of quiescence by about 1.5 years (*Wyss and Habermann*, 1988a). In the Landers and Big Bear cases an increase of one in the magnitude of the mainshock is associated with an increase in the duration of quiescence of about 3 years.

The location of the northern lobe of the seismicity rate decrease (Figure 2.7) correlates with the March 15, 1979 M = 5.3 Homestead Valley earthquake (*Stein and Lisowski*, 1983). This earthquake preceded the Landers earthquake by 13.3 years. The declustering of the catalog is designed to remove aftershock sequences. therefore the observed anomaly should not be influenced by aftershock activity of the Homestead Valley mainshock. In addition, two further arguments support the fact that the influence of the Homestead Valley earthquake on our analysis is negligeable: (1) Looking at the cumulative number curves (Figure 2.8A and 8B, Figure 2.11) one can observe a stable seismicity rate between March 81 and December 87 for events with a magnitude $\geq$ 1.6. The onset of the anomaly is sharp and not a general decline as expected for an aftershock sequence. (2) We extracted the aftershocks of the Homestead Valley earthquake from the complete catalog, using a program described by *Reasenberg* (1985). No aftershock with a magnitude M $\geq$1.6 was detected later than 78 days (June 1, 1979) after the Homestead Valley earthquake. We also modeled the aftershock sequence, using *Utsu's* (1961) modified Omori relation for the rate of occurrence of aftershocks as a function of time after the mainshock (see also *Kisslinger and Jones*, 1991). In the period between March 1981 and June 1992 less than five events with a magnitude $\geq$1.6 are expected due to the aftershock sequence of the Homestead Valley earthquake. We conclude that

the observed quiescence was not due to a decreasing aftershock sequence at Homestead Valley.

The remaining question is: how significant is the quiescence prior to the Landers and Big Bear earthquakes, compared to other rate changes in the catalog? Using the described visualization gives a qualitative answer to this question by comparing the significance, number, and brightness of 'hot spots' in different time slices (Figures 2.3, 2.4, and 2.5). A more quantitative answer to this question, using statistical tests, is essential in defining the significance and false alarm rate of the anomalies. The AS(t) function has a tendency to overestimate rate changes at the end of a time series. An unbiased test of the significance of the rate changes is possible using the LTA function (Long Term Average: *Habermann*, 1988, 1991):

$$z(t) = \frac{R_{all} - R_{wl}}{\sqrt{\frac{s_{all}^2}{n_{1all}} + \frac{s_{wl}^2}{n_{2wl}}}}$$

The LTA function compares the overall mean rate R_{all} to the mean rate R_{wl} in a window of length wl (n indicates the number of samples, s the standard deviation). This window is moved over the entire period in 2 week steps. The length of the LTA window adds another dimension to the analysis. We calculated the LTA-function, using several window lengths. Three representative calculations with lengths of 4.5 years (Figure 2.15), 3.0 (Figure 2.16) and 1.5 years (Figure 2.17) are shown here. We used a grid with a spacing of 2 km and volumes of variable size containing 130 earthquakes as described in detail above. The variation of the LTA function over time can be visualized as an animation in the same way as described for the AS(t) function. We found it helpful to view the LTA-function compressed in time by plotting on a map only the maximum value over all times at each grid point. This approach is useful, if one is interested in comparing the significance of rate changes for a specific window length. The concept of maximum LTA maps provides a powerful tool to investigate seismicity rate changes, especially when combined with the ability to interactively view cumulative number curves at each point on the map.

For a window length of 4.5 years, the most outstanding anomaly in the whole catalog is the previously described Landers anomaly (onset January 1988, Figure 2.15). If we define an alarm level of z = 2.5 (e.g. *Wyss*, 1992), more than 10 false alarms are detected. Increasing the alarm level to z = 3.0 reduces the number of false alarms to 4, for z = 3.4 no false alarm occurs. The his-

togram of all z-values (Figure 2.15) demonstrates how outstanding the Landers anomaly is. The z-values of the Landers anomaly occur at the right end of an approximately normal distribution of all calculated z-values for this window length.

LTA is a function of the window-length, the shorter the window the higher the LTA values (e.g. *Wyss*, 1992). For an intermediate window-length of 3 years the Landers anomaly shows the highest z-values (Figure 2.16). The second outstanding anomaly visible in Figure 2.16 started in February 1986 and was terminated in June 1989 by a M = 4.3 earthquake. The magnitude signature of this anomaly does not indicate any artificial rate changes, the seismicity rate is reduced for all magnitude bands. At first we were not aware of the M = 4.3 mainshock and therefore thought we should interpret this quiescence as a false alarm. However, the 36 month duration as well as the approximately 10 km length of this anomaly are almost identical to these parameters (35 month and 8 km, respectively) observed for the Stone Canyon earthquake (M = 4.7). This earthquake was actually predicted by *Wyss and Burford* (1985, 1987). Therefore, we interpret the observed anomaly prior to the M = 4.3 earthquake as possible seismic quiescence. In our analysis of the Landers area we found several other moderate earthquakes that appear to be preceded by seismic quiescence. However, in this study we focused on the three mainshocks with magnitudes greater than 6. The question of quiescence anomalies before smaller mainshocks in Southern California will be investigated in the future.

The third highest anomaly for a window length of 3 years must be interpreted as a false alarm (labeled in Figure 2.16). No major earthquake occurred at the end of this quiescence, but the volume over which it extended is small (less than 5 km). Using a window of 1.5 years the most outstanding anomaly is correlated in space and time with the Big Bear quiescence (Figure 2.17). With an alarm level of z = 6.8 this anomaly is unique, therefore no false alarms occur. Decreasing z to 6.0 results in 6 alarms, the Big Bear, the Landers and four false alarms. For z = 5.0 more than 10 false alarms occur.

The case of the Joshua Tree earthquake shows that precursory seismic quiescence is not always observed before major earthquakes. A possible explanation for the missing quiescence might be that the Joshua Tree earthquake is the smallest event of the three (M = 6.1). As stated earlier precursory seismic quiescence is not restricted to large earthquakes, but for larger events with

larger source volumes one might expect a more readily definable quiescence anomaly.

There have been four earlier studies of precursory seismic quiescence in which the seismicity rate was high enough to allow separate studies of sub-volumes of the source. These are the Kalapana (Hawaii, November 1975, Ms = 7.2; *Wyss et al.*, 1981), the Kaoiki (Hawaii, 16 November 1983, Ms = 6.6; *Wyss*, 1986b), the Andreanoff Islands (Aleutians, 7 May 1986, Ms = 7.7; *Kisslinger*, 1988) and Stone Canyon (California, August 1982, M_L = 5.0, *Wyss and Habermann*, 1988b) studies. In all of these case studies the initial rupture occurred in a volume of constant seismicity rate, surrounded by volumes containing quiescence. The precursory seismic quiescence before the Landers mainshock shows similar behavior: the volumes that turned quiescent are centered 10 km north and to the south of the rupture initiation. The volume around the rupture initiation shows a decrease in the seismicity rate beginning in November 1989 (Figure 2.8C) which is 1.8 years after the onset of the quiescence 10 km north of the rupture initiation. This seismicity rate decrease ends 0.5 years before the Landers earthquake and one might speculate that this is due to foreshock activity. *Wyss* (1986a) and *Wyss and Habermann* (1988b) suggested that this behavior might be a general pattern of precursory seismic quiescence, in which major asperities do not turn quiet while the rest of the source does. The Landers case supports this idea while the Big Bear case does not, as the Big Bear quiescence occurs at the epicenter and covers most of the fault area (Figure 2.9). No foreshock activity was observed prior to the Big Bear earthquake in its source volume.

The moment release of the Landers earthquake has been discussed by several authors (e. g. *Wald et al.*, 1992; *Kanamori et al.* 1992; *Cohee and Beroza*, 1992). Based on long period regional seismograms, *Campillo and Archuleta* (1992) divide the Landers earthquake into two sub-events, one on the epicenter location, the other one along the Camp Rock-Emerson fault approximately 30 km north of the epicenter. Models of the moment release, and the dynamic slip distribution over the Landers fault, show approximately 1/3 of the moment released in the initial rupture whereas the greatest part of the moment release is approximately 30 km north of the epicenter (*Wald et al.*, 1992; *Kanamori* et al. 1992; *Cohee and Beroza*, 1992). *Abercrombie and Mori* (1994) have investigated the slip history of the Landers earthquake. Their analysis uses the onset of large amplitude waves 2.5 seconds after the first sub-event of M_w = 4.4, to place the main hypocenter a few kilometers to the north and at greater depth than the initial focus. Thus, the source of the main quiescence correlates with the location of the greatest moment release. Our results indicate that rupture

zones undergo a final quiescent stage a few years prior to the main rupture. In our understanding, triggering of large events by moderate earthquakes (as suggested by *Brune* (1979) and *Abercrombie and Mori* (1994)) might occur when a moderate event occurs in the vicinity of a quiescent volume.

The factors that support the hypothesis that the described anomalies before the Landers and Big Bear earthquake were caused by precursory seismic quiescence are the following:

(1) The anomalies correlate in space and time with the Landers and Big Bear earthquakes. The durations of the anomalies are in good agreement with earlier case studies.

(2) Anomalies occur only in areas related to the main-shock rupture and correlate well with areas of high moment release on the fault. Outside these areas the seimicity rate remains stable or increases.

(3) The decrease in the seimicity rate of 75 - 100% is statistically highly significant.

(4) The rate decrease does not show the characteristics of an artificial rate change. The rates are reduced in all magnitude bands. The rate changes were present in the original data, as well as in the data corrected for inadvertent magnitude shifts.

(5) The Landers and Big Bear anomalies are the most outstanding in the whole catalog. They could be detected without false alarms.

In this paper we propose that we have identified two cases of precursory quiescence to two major Californian earthquakes. One smaller mainshock was not preceded by quiescence. These results support findings that the hypothesis of precursory seismic quiescence is applicable in southern California.

2.7 Acknowledgments

This work was supported by the U.S. Geological Survey by grant No. 1408-0001-G1306 and the Wadati endowment at the University of Alaska, Fairbanks. We would like to thank J. Savage, R. Habermann, J. Lahr, J. Benoit, H. Fletcher, and an anonymous reviewer for comments and crit-

icism that helped to improve the paper. We also thank the operators of the Southern California seismograph network (Caltech and the USGS) for making available their earthquake catalog.

2.8 References

Albercombie, R. and J. Mori (1994). Local Observations of the onset of a large earthquake: 28 June 1992 Landers, California, *Bull. Seism. Soc. Am.*, Vol. 84, No. 3, 725-734.

Brune, J.N. (1979). Implications of earthquake triggering and rupture propagation for earthquake prediction based on premonitory phenomena, J. Geophys. Res., 84, 2195 - 2198.

Campillo, M. and R. Archuleta (1992). A rupture model for the 28 June 1992 Landers, California. earthquake, EOS (Transactions, American Geophysical Union), 73, 374.

Cao, T. and K. Aki (1987). Physical basis for the magnitude cut-off dependence of seismic quiescence, U.S. Geol. Surv. Open File Report, 87-591, 934-957.

Cohee, B.H. and G.C. Beroza (1992). Inversion for Slip of 1992 Landers Mainshock Using Broadband TERRAscope Seismograms, EOS (Transactions, American Geophysical Union), 73, 357.

Habermann, R.E. (1981). Precursory seismicity patterns: stalking the mature seismic gap, in: Earthquake Prediction, eds. D.W. Simpson and P.G. Richards, Maurice Ewing Series, Amer. Geophys. Union, 4, 2942.

Habermann, R.E. (1982). Consistency of teleseismic reporting since 1963, Bull. Seism. Soc. Am, 72, 93-112.

Habermann, R.E. (1983). Teleseismic detection in the Aleutian Islands arc, J. Geophys. Res., 88, 5056-5064.

Habermann, R.E. (1986). A test of two techniques for recognizing systematic errors in magnitude estimates using data from Parkfield, California, Bull. Seism. Soc. Am., 76,1660-1667.

Habermann, R.E. (1987). Man-made changes of seismicity rates, Bull. Seism. Soc. Am., 77, 141-159.

Habermann, R.E. (1988). Precursory seismic quiescence: past, present and future, PAGEOPH, 126, 279-318.

Habermann, R.E. (1991). Seismicity rate variations and systematic changes in magnitudes in teleseismic catalogs, Tectonophysics, 193, 277-289.

Hauksson, E., and nine others (1992). Overview over the 1992 (M6.1, 7.5, 6.6) Landers Earthquake Sequence in the San Bernadino County, California, EOS (Transactions, American Geophysical Union), 73, 357.

Kanamori, H. (1981). The nature of seismicity patterns before large earthquakes, in: Earthquake prediction, Maurice Ewing Series, Amer. Geophys. Union, 4, 1-19.

Kanamori, H., Hong-Kie Thio, D. Dreger, E. Hauksson, T. Heaton (1992). Investigation of the Landers, California, Earthquake of 28 June 1992 Using TERRAscope, EOS (Transactions, American Geophysical Union), 73, 357.

Kisslinger, C. (1988). An experiment in earthquake prediction and the 7 May 1986 Andreanof Is-

lands earthquake, Bull. Seism. Soc. Am., 78, 218-229.

Kisslinger, C. and L.M. Jones (1991). Properties of Aftershock Sequences in Southern California, J. Geophys. Res., 97, 11947-11958.

Mogi, K (1969). Some features of recent seismic activity in and near Japan (2), Activity before and after great earthquakes, Bull. Earthq. Res. Inst., Univ. of Tokyo, 47, 395-417.

Ohtake, M., T. Matumoto, and G.V. Latham, (1977). Seismicity gap near Oaxaca, Southern Mexico, as a probable precursor to a large earthquake, PAGEOPH, 115, 375-385.

Perez, O.J. and C.H. Scholz (1984). Heterogeneities of the instrumental seismicity catalog (1904-1980) for strong shallow earthquakes, Bull. Seism. Soc. Am., 74, 669-686.

Reasenberg, P.A (1985). Second-order moment of Central California seismicity, 1969-1982, J. Geophys. Res., 90, 5479-5495.

Reasenberg, P.A., and M.V. Matthews (1988). Precursory seismic quiescence: A preliminary assessment of the hypothesis, PAGEOPH, 126, 373-406.

Rudnicki, J.W. (1988). Physical Models of earthquake instability and precursory processes, PAGEOPH, 126, 531-554.

Scholz, C.M., L.R. Sykes, and Y.P. Aggarwal (1973). Earthquake prediction: a physical basis, Science, 181, 803-810.

Scholz, C.M. (1988). Mechanism of seismic quiescence, PAGEOPH, 126, 701-707.

Stein, R.S. and M. Lisowski(1983). The 1979 Homestead Valley Earthquake Sequence, California: Control of Aftershocks and Postseismic Deformation, J. Geophys. Res., 88, 6477-6490.

Stuart, W.D. (1979). Strain softening prior to two-dimensional strike slip earthquakes, J. Geophys. Res., 84, 1063-1070.

Stuart, W. D. (1991). Seismic quiescence at Parkfield due to detachment faulting, Nature, 349, 58-61.

Sykes, L.R. and S.C. Jaumé, (1990). Seismic activity on neighboring faults as a long-term precursor to large earthquakes in the San Francisco Bay area, Nature, 348, 595-599.

Utsu, T., (1961). A statistical study on the occurrence of aftershocks, Geophys. Mag,. 30, 521-605.

VonSeggern, D., S. Alexander and C. Baag (1981). Seismicity parameters preceding moderate to major earthquakes, J. Geophys. Res., 86, 9325-9351.

Wald, D.J., D. Helmberger, H. K. Thio, D. Dreger (1992). On Developing a Single Rupture Model for the 1992 Landers, California, Earthquake Consistent With Static, Broadband Teleseismic, Regional and Strong Motion Data Sets, EOS (Transactions, American Geophysical Union), 73, 358.

Wessel, P. and W.H.F. Smith (1991). Free software helps map and display data, EOS Trans. AGU. 72, 441.

Wyss, M. (1986a). Seismic quiescence precursor to the 1983 Kaoiki (Ms = 6.6) Hawaii, earthquake, Bull. Seism. Soc. Am., 76, 785-800.

Wyss, M. (1986b). Regular intervals between five Hawaiian earthquakes: Implications for predict-

ing the next event, Science, 234, 726-728.

Wyss, M. (1991). Reporting history of the central Aleutians seismograph network and the quiescence preceding the 1986 Andreanof Island earthquake, Bull. Seism. Soc. Am.,81, 1231-1254.

Wyss, M., and R.O. Burford (1985). Current episodes of seismic quiescence along the San Andreas Fault between San Juan Bautista and Stone Canyon, California: Possible precursors to local moderate mainshocks, U.S. Geol. Survey open-file report, 85-754, 367-426.

Wyss, M., and R.O. Burford (1987). A predicted earthquake on the San Andreas fault, California, Nature, 329, 323-325.

Wyss, M. and Z-X. Fu (1989). Precursory seismic quiescence before the January 1982 Hilea, Hawaii, earthquake, Bull. Seism. Soc. Am., 79, 756-773.

Wyss, M., and R.E. Habermann (1988a). Precursory quiescence, PAGEOPH, 126, 319-332.

Wyss, M., and R.E. Habermann (1988b). Precursory quiescence before the August 1982 Stone Canyon, San Andreas fault earthquakes, PAGEOPH, 126, 319-332.

Wyss, M., P. Bodin, and R.E. Habermann (1990). Seismic quiescence at Parkfield: An independent indication of an imminent earthquake, Nature, 345, 426-428.

Wyss, M., R.E. Habermann, and P. Bodin (1992). Seismic quiescence: A test of the hypothesis and a precursor to the next Parkfield, California, earthquake, Geophys. J. Int., 110, 518-536.

Wyss, M., F.W. Klein and A.C. Johnston (1981). Precursors to the Kalapana M = 7.2 earthquake, J. Geophys. Res., 86, 3881-3900; also see M. Wyss (1986), Bull. Seism. Soc. Am., 76, 785-800.

2.9 Figures

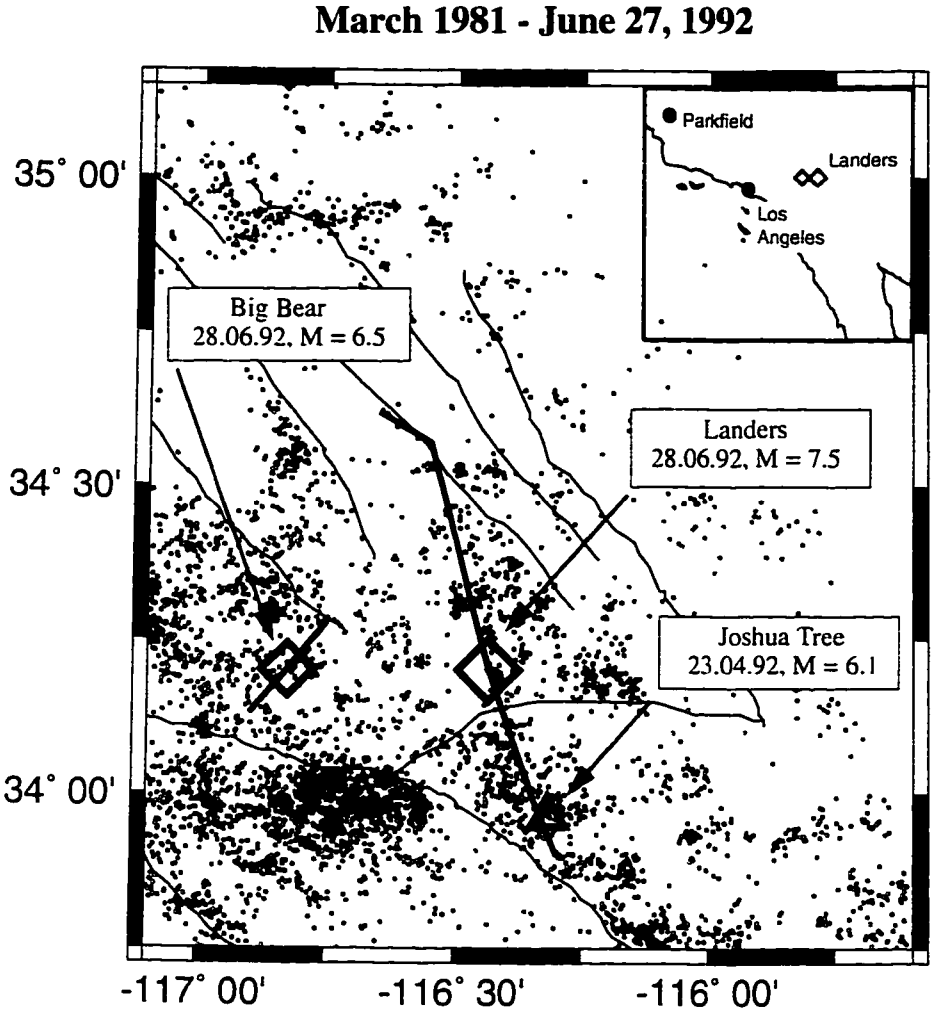

Figure 2.1. Epicenter map of the Landers area showing the epicenters of Landers 28.06.92 M = 7.5 mainshock (large diamond) and of the 28.06.92 M = 6.5 Big Bear aftershock (small diamond). For both earthquakes the rupture (based on the aftershock distribution) is plotted as a thick line. The epicenter of the Joshua Tree (23.04.92 M = 6.1) earthquake is marked by a triangle. The thinner lines correspond to the mapped faults. The small circles show the epicenters ($M \geq 1.6$) contained in the declustered and magnitude corrected catalog we used in our study (5655 events). The catalog spans the time from March 1981 to 27 June 1992.

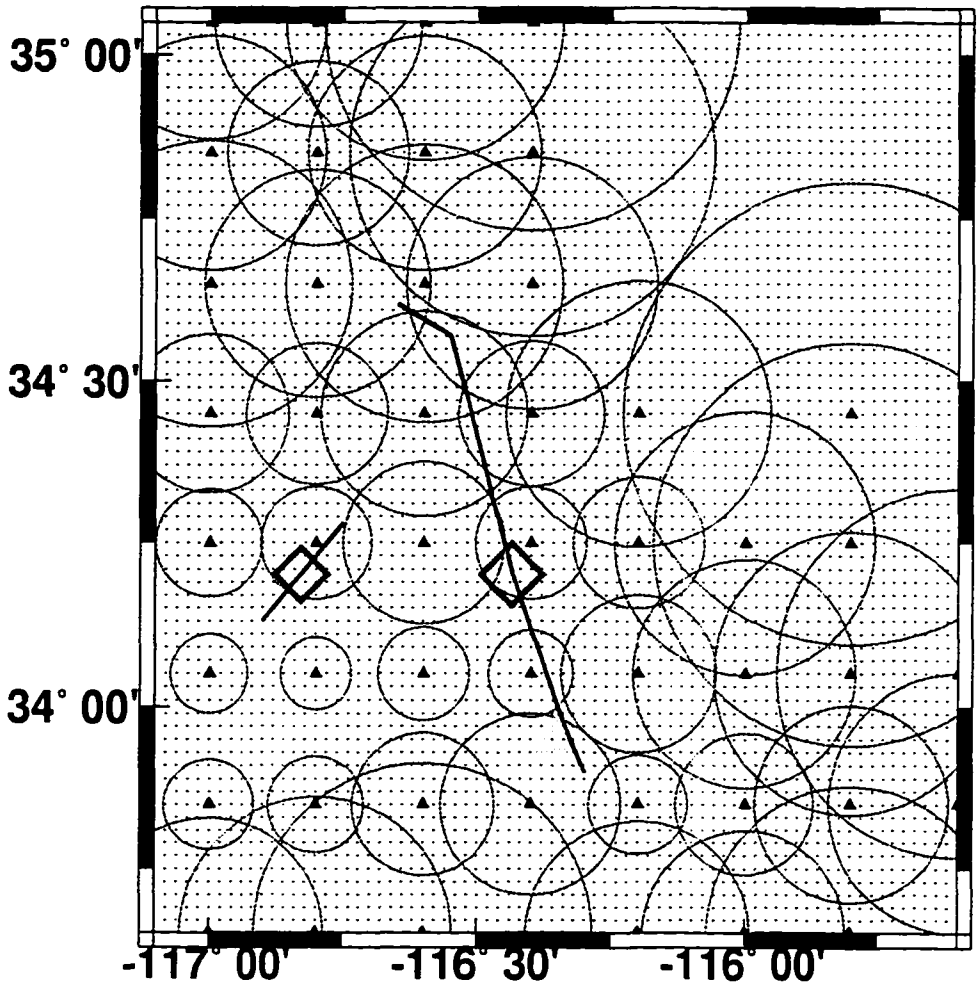

Figure 2.2. Map of the grid used to study the Landers area. For selected points (triangles) the circles representing areas containing 130 epicenters from March 1 1981 to June 27 1992 are shown. The radius r of the circles is inversely proportional to the local density of earthquakes (see Figure 2.1 for comparison). The radii range from 4 km to 32 km and can be used as a measure of the resolution.

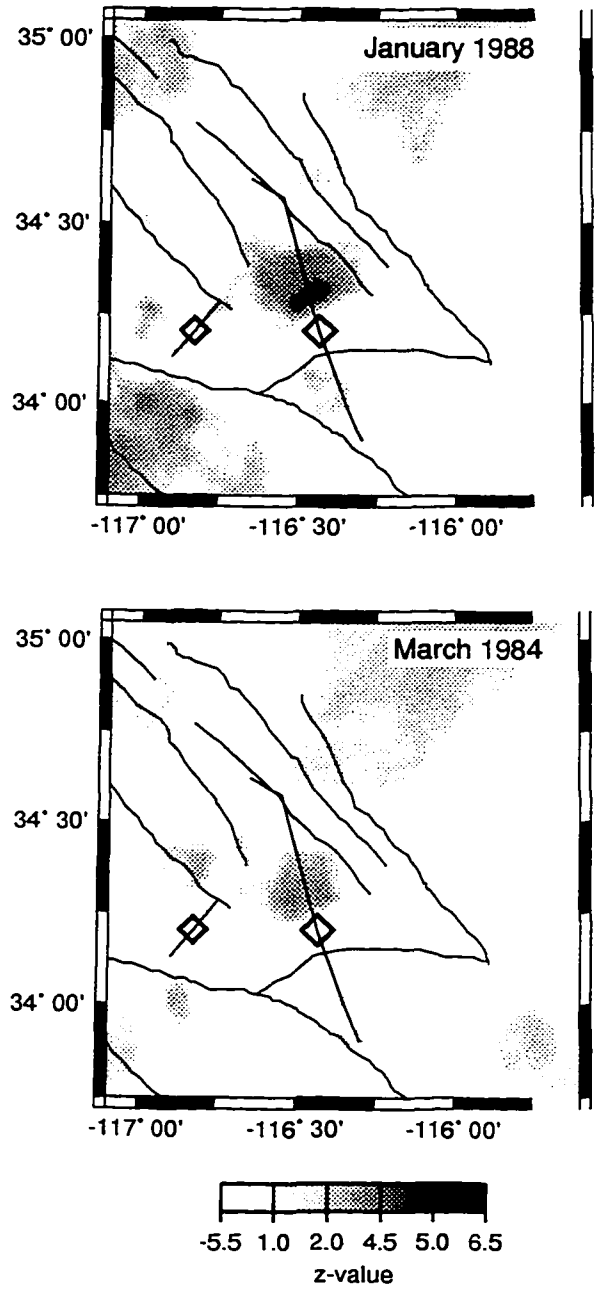

Figure 2.3. Maps of the Landers area showing the degree of seismicity rate decrease (Jan. 1988 and Mar. 1984). Rate changes are measured by the standard deviate z and presented in a gray-code for a comparison of the mean rates before and after January 1988 (top frame), as well as before and after March 1984 (bottom frame). The earthquake catalog used is defined in Figure 2.1. The number of events in each volume is 130. High z-values (shown in dark) represent a decrease in the seimicity rate. The highest z-values occur on the Landers M = 7.5 fault-zone, approximately 10 km north of the rupture initiation point. The anomaly of high z-values is surrounded by low or negative z-values, representing no seismicity change or increased seimicity. The mainshock epicenters and ruptures are marked as in Figure 2.1. The bottom frame shows that no significant changes occur during the early part of the record.

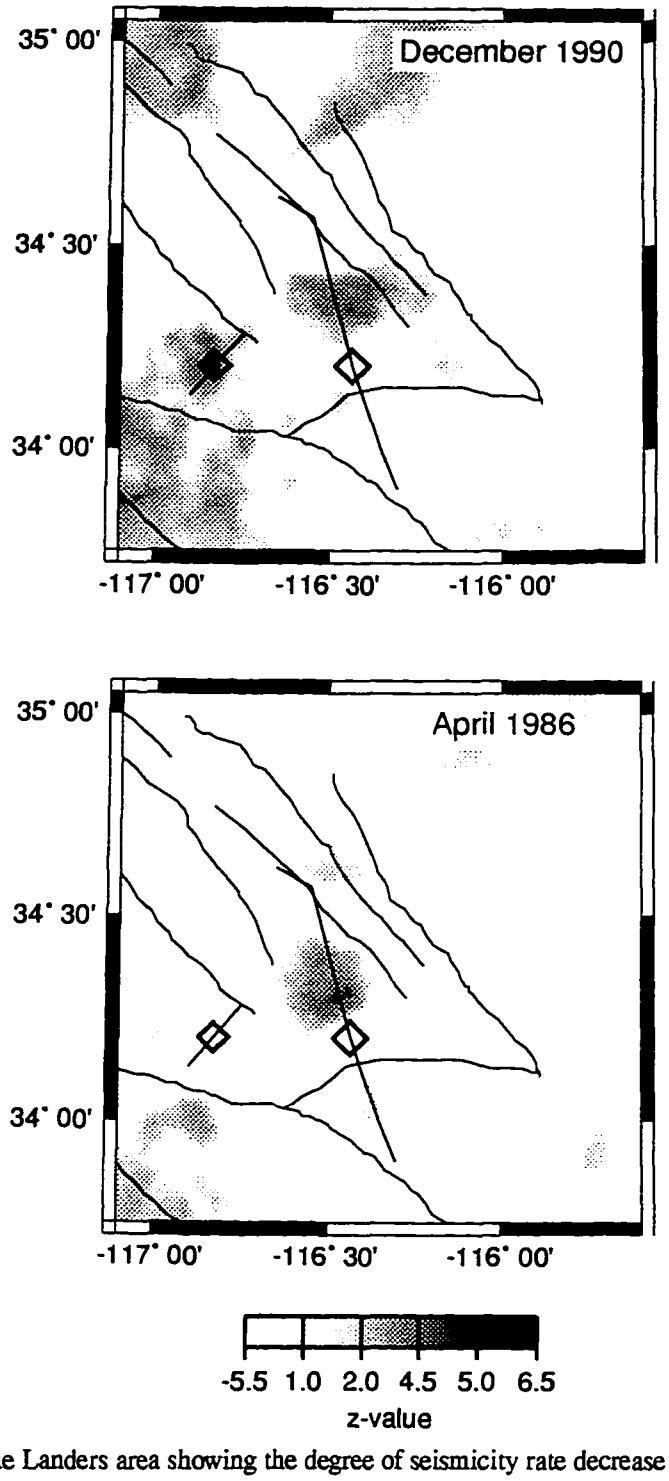

Figure 2.4. Maps of the Landers area showing the degree of seismicity rate decrease (Dec. 1990 and Apr. 1984). Compared is the mean before and after December 1990 (top frame), as well as before and after April 1986 (bottom frame). High z-values occur in the top frame at the epicenter of the 1992 Big Bear M = 6.5 earthquake and indicate a strong decrease in the seismicity, starting 1.6 years before this earthquake. The bottom frame shows that no anomalies exist during the background time, except that a trace of the Landers anomaly emerges.

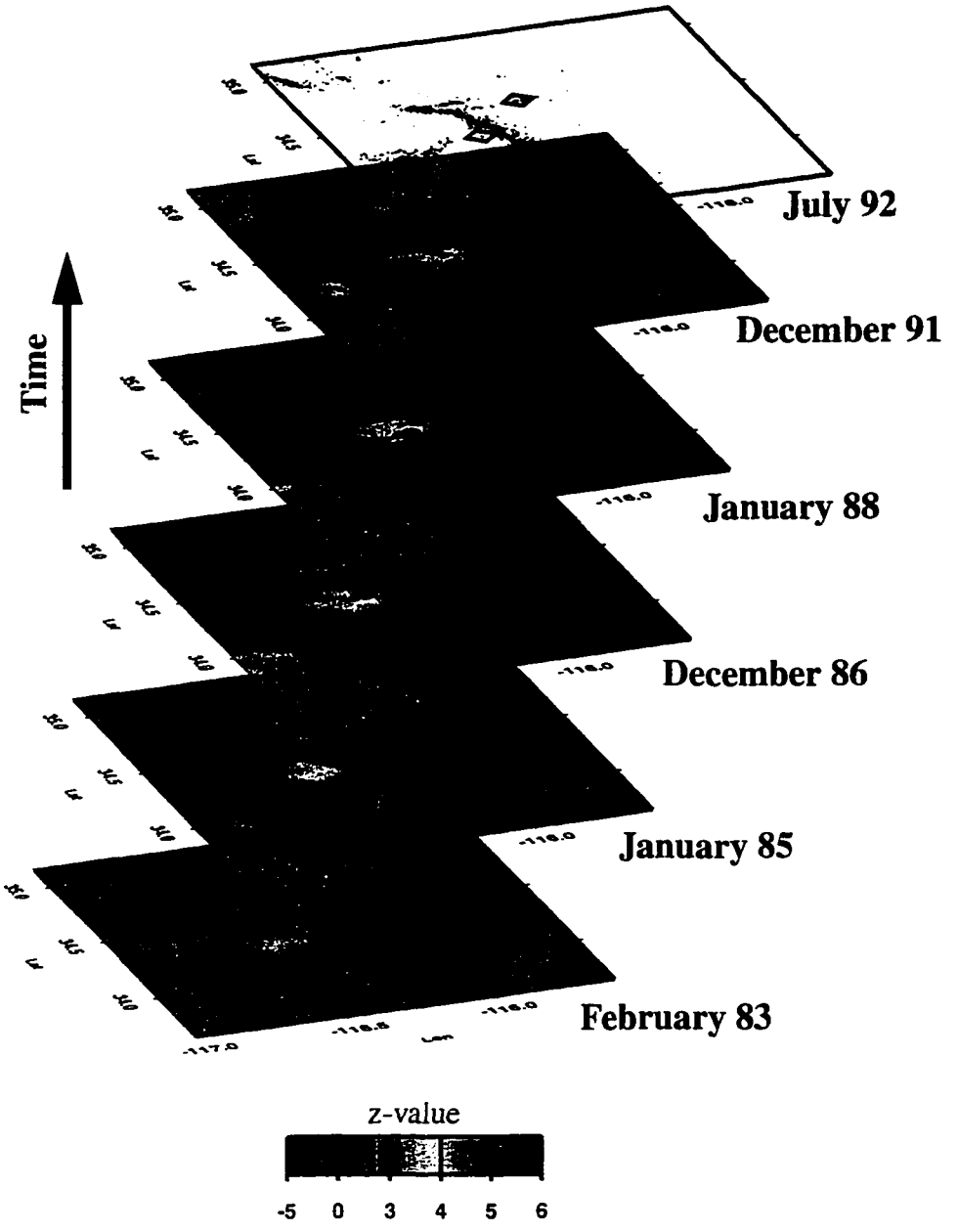

Figure 2.5. Time slices showing the degree of seismicity rate change in the Lander area (same as Figure 2.3). The z-values measure the significance of rate changes comparing the mean before and after the times selected (which are from bottom to top: February 1983, January 1985, December 1986, January 1988 and December 1991). The topmost frame shows the main and aftershock epicenters. The location of the two strongest rate decreases in the entire catalog (hot colors) correlate with the centers of the Landers and Big Bear ruptures. These anomalies begin about 4.5 and 1.6 years before these mainshocks, respectively, and last up to the mainshock. These durations are comparable to quiescence precursor times in other cases. We interpret these two quiescence anomalies as precursors. No significant rate changes occur near the epicenter of the April 1992 Joshua Tree earthquake.

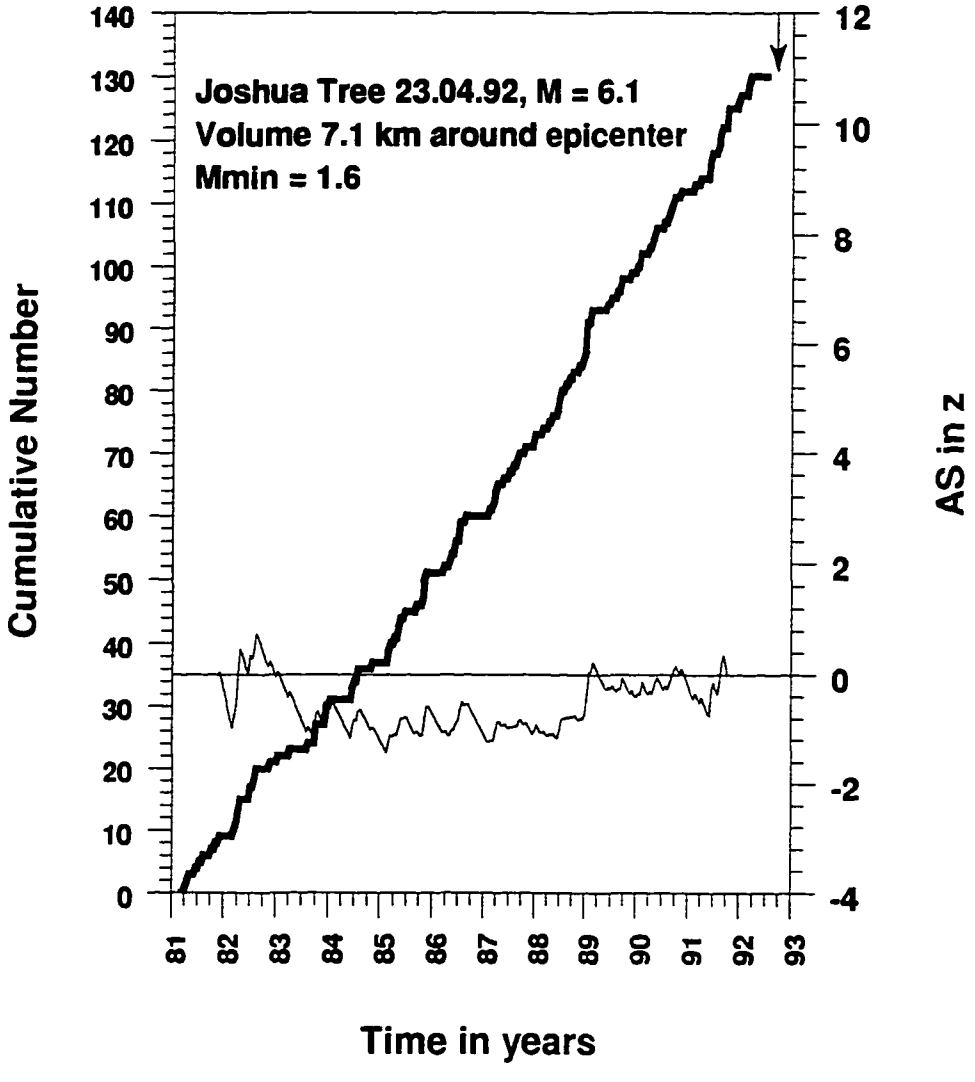

Figure 2.6. Cumulative number of earthquakes as a function of time, in a volume containing 130 events around the epicenter of the Joshua Tree April 1992 M = 6.1 earthquake. The time of the Joshua Tree earthquake is marked by an arrow. No significant rate change occurred in this volume.

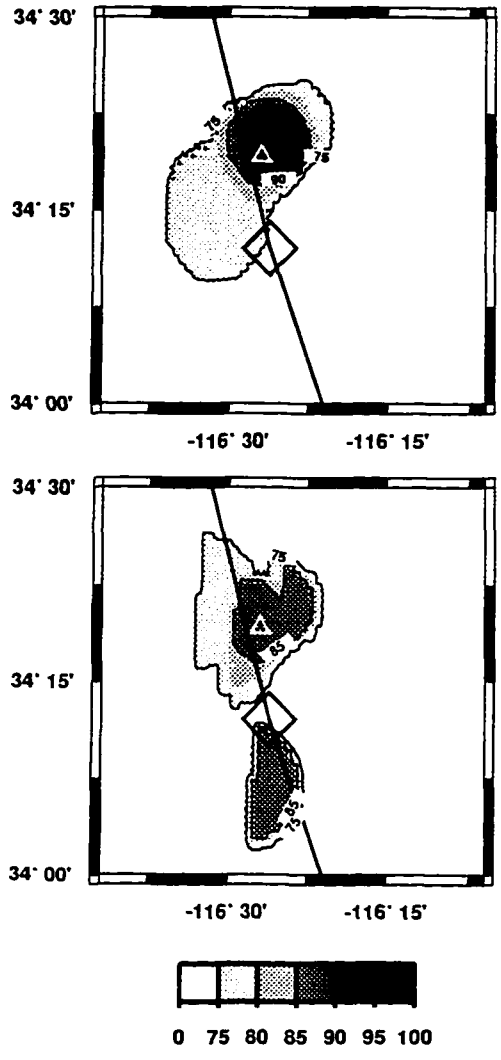

Figure 2.7. Map of the seismicity rate decrease in 1988 near the Landers M = 7.5 mainshock (diamond) on its rupture zone (heavy line) (top frame) . The white triangle marks the position of the M = 5.3 Homestead Valley earthquake of March 15, 1979. The gray-colors refer to the seismicity rate decrease, in percent, comparing the two periods: March 1981 to January 1988 and February 1988 to June 27 1992. We normalized for the different length of these periods and calculated the reduction in percent of the later period compared to the first. N_i, the number of events in each volume is 50. The highest decrease in seimicity (93%) occurs 10 km north of the epicenter of the 1992 Landers earthquake. The decrease to the east of the ruptured fault is higher than on the west side. The area within the 75% decrease contour line has dimensions of approximately 23 km x 11 km and contains 161 earthquakes with M $\geq$1.6. The distribution of these earthquakes are shown in the cumulative number versus time plot in Figure 2.8. The bottom frame compares the two periods: March 1981 to December 1989 and January 1990 to June 27 1992. Two lobes of decreased seismicity to the north and the south of the Landers epicenter appear in this presentation of the anomaly.

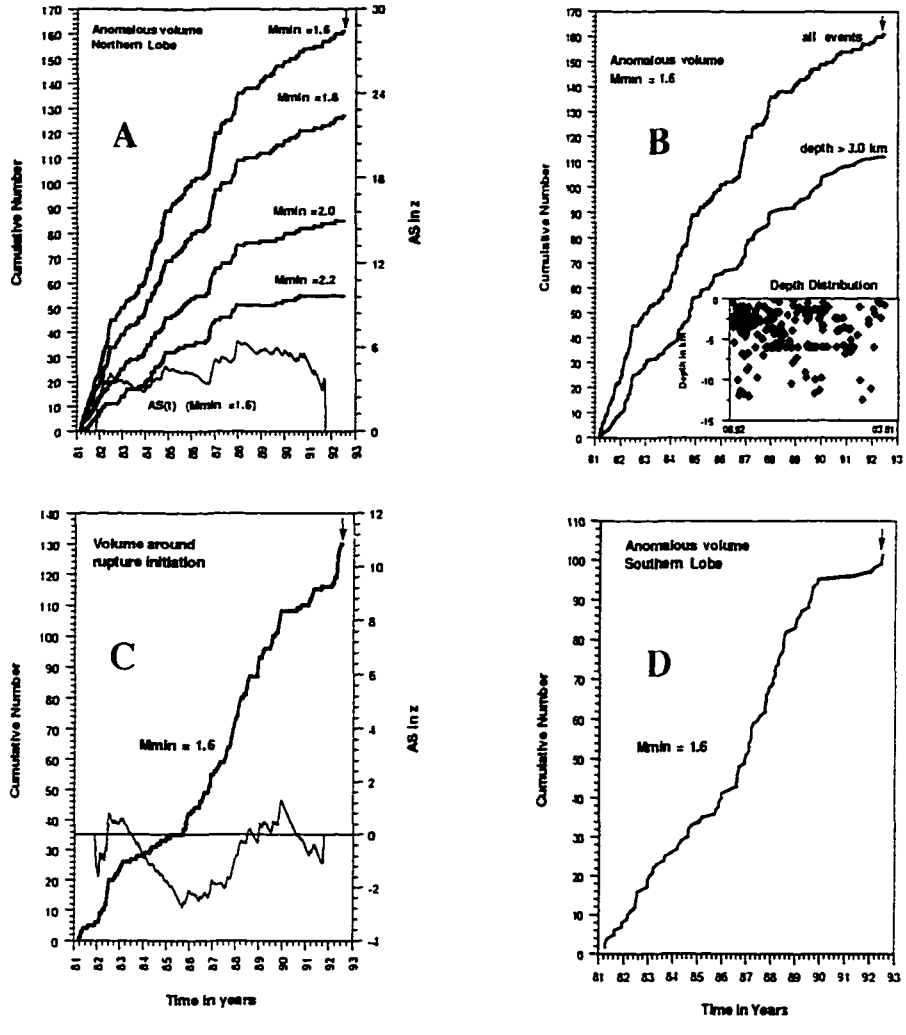

Figure 2.8. Cumulative number of earthquakes as a function of time in the anomalous volume (Frame A) of the Landers 1992 rupture, defined by the 75% contour line in Figure 2.7 (top) for different magnitude thresholds (M_{min} = 1.6, 1.8, 2.0, 2.2). The thin line at the bottom is the AS(t) function for M_{min} = 1.6. For all magnitude thresholds the onset of the quiescence occurs simultaneously in January 1988 (dotted vertical line). The time of the Landers earthquake is marked by an arrow. Frame B: Cumulative number of earthquakes versus time in the anomalous volume of the Landers 1992 rupture defined in Figure 2.7 (top) for different depth thresholds (all events and only events with a depth > 3 km). The onset of the quiescence occurs simultaneously in January 1988 (doted vertical line). The graph in the lower right corner shows the depth distribution of earthquakes with time. The time of the Landers earthquake is marked by an arrow. Frame C: Cumulative number of earthquakes as a function of time in the volume containing 130 events centered at the epicenter of the Landers 1992 M = 7.5 earthquake. The time of the earthquake is marked by an arrow. The increase in seismicity at the end of the period is due to foreshock activity. A quiescence anomaly cannot be defined at a statistically highly significant level. Frame D: Cumulative number of earthquakes in the southern lobe of the anomalous volume defined by the 75% contour line in Figure 2.7 (bottom). A strong seismicity decrease starting in November 1989 can be observed before the Landers earthquake.

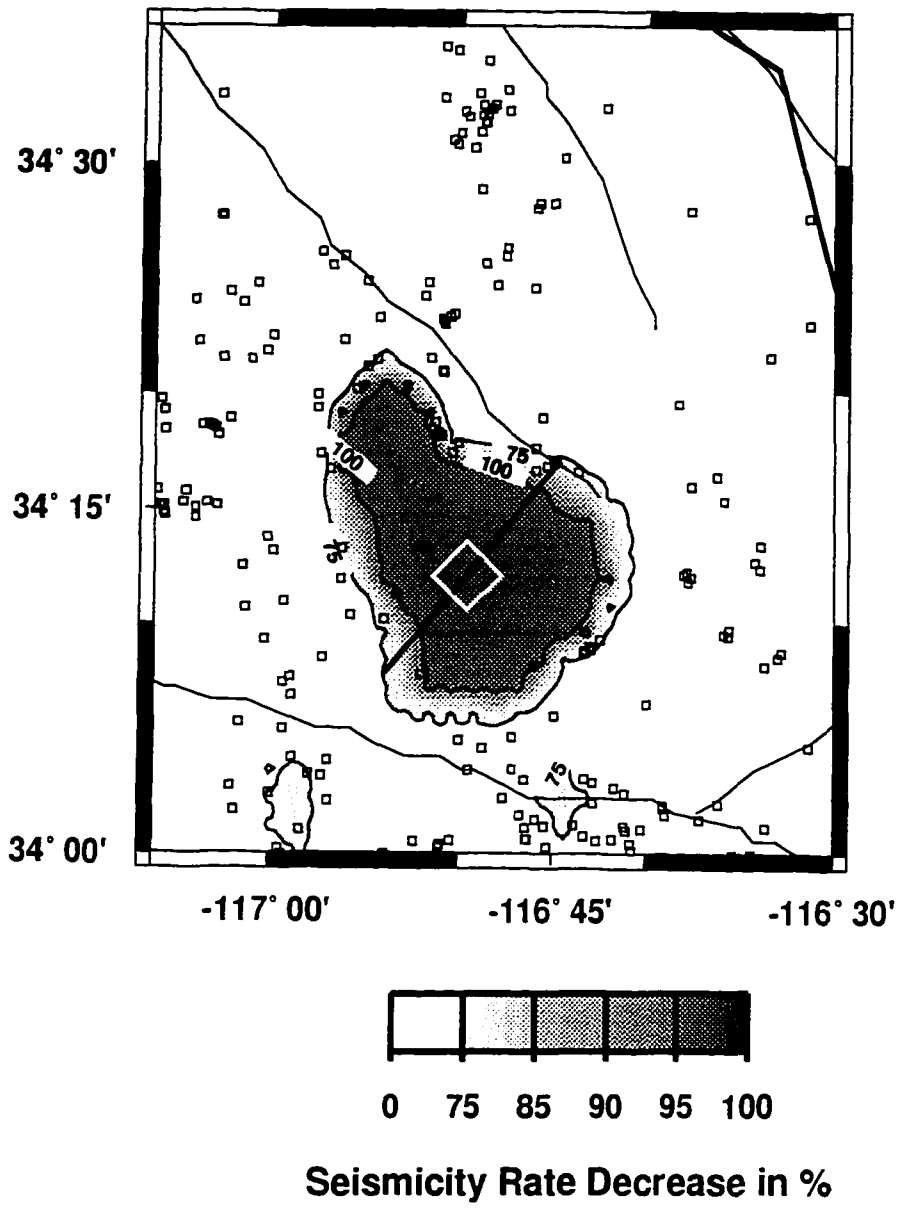

Figure 2.9. Map of the rate decrease in 1990 near the 1992 Big Bear M = 6.5 aftershock (diamond), and its rupture zone (heavy line). The gray-colors refer to the seismicity rate decrease, comparing two periods: March 1 1981 to November 1990 and December 1990 to June 27 1992. We normalized for the different length of these periods and calculated the reduction in percent of the later period compared to the first. The number of events in each volume is 50, with M_{min}=1.6. The highest decrease in seimicity occurs directly at the epicenter of the Big Bear earthquake. The cumulative seismicity within the 75% and 100% contour lines is shown in Figure 2.10. The squares mark epicenters of earthquakes that occurred after December 1990.

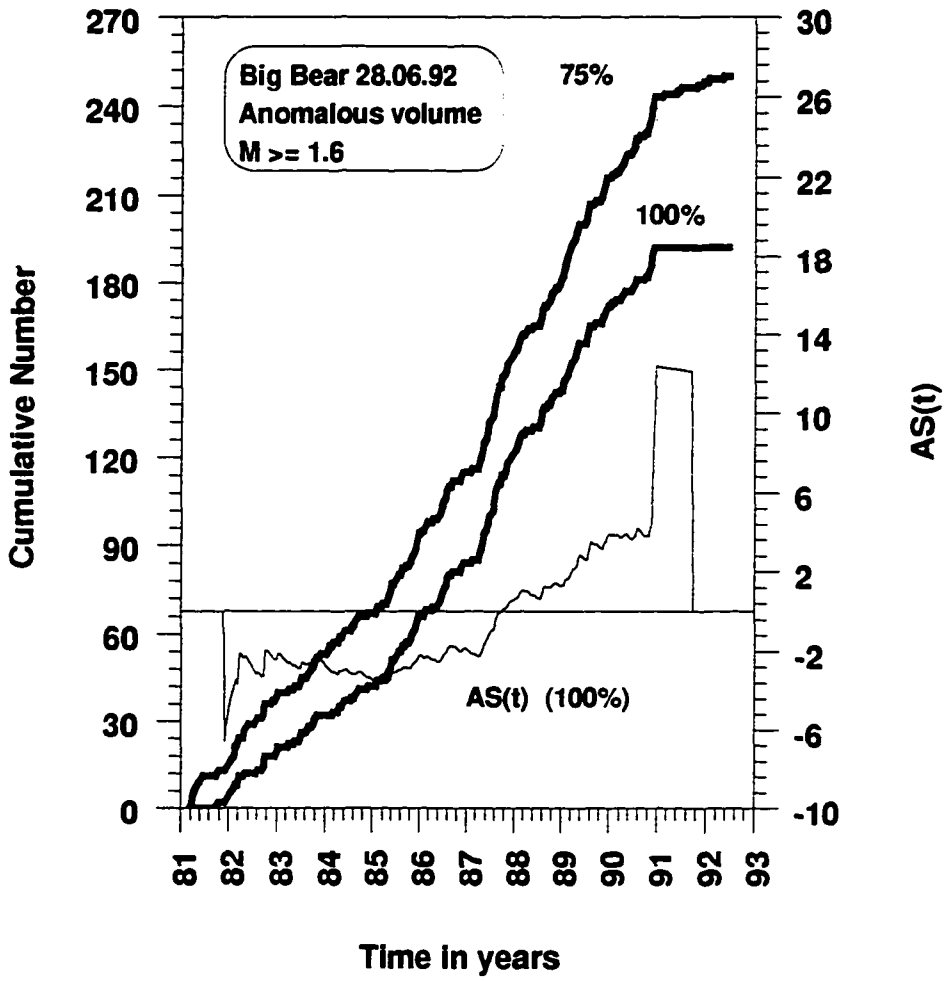

Figure 2.10. Cumulative number of earthquakes as a function of time in the anomalous volume around the Big Bear 1992 hypocenter defined by the 75% and 100% contour lines in Figure 2.9. The magnitude threshold is M_{min}1.6. The thin line represents the AS(t) function. The time of the Big Bear earthquake is marked by an arrow. After November 1990 (dotted vertical line) no earthquake occurred in the smaller of the two volumes considered, resulting in a highly significant AS(t) value of 12.3.

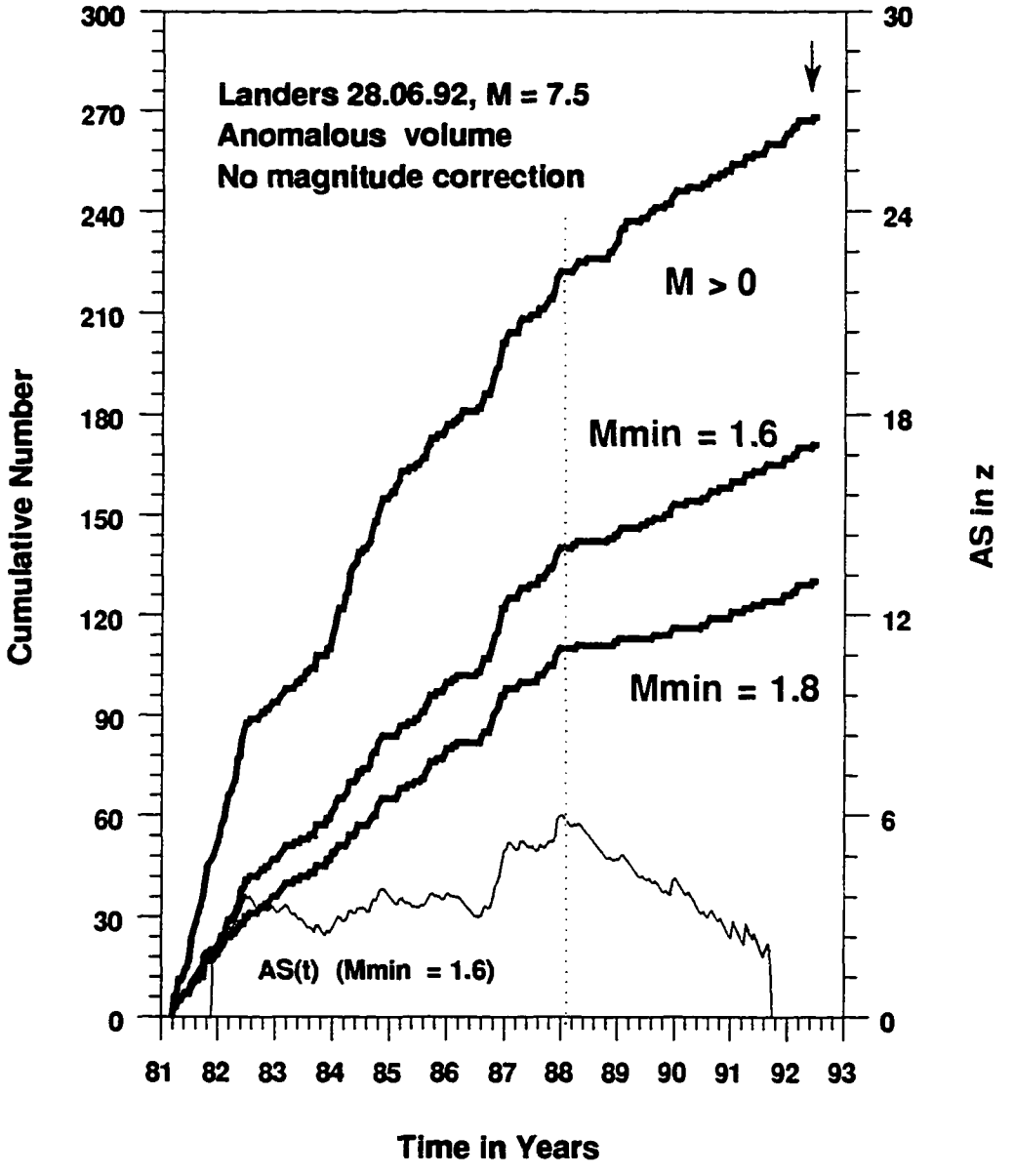

Figure 2.11. Cumulative number of earthquakes as a function of time in the anomalous volume of the Landers 1992 rupture, defined in Figure 2.7. All events reported with a magnitude > 0 are considered, and no magnitude correction is applied to the declustered catalog. The thin line is the AS(t) function, the time of the Landers earthquake is marked by an arrow. The quiescence beginning in January 1988 is clearly visible, showing that we have not introduced it through our corrections.

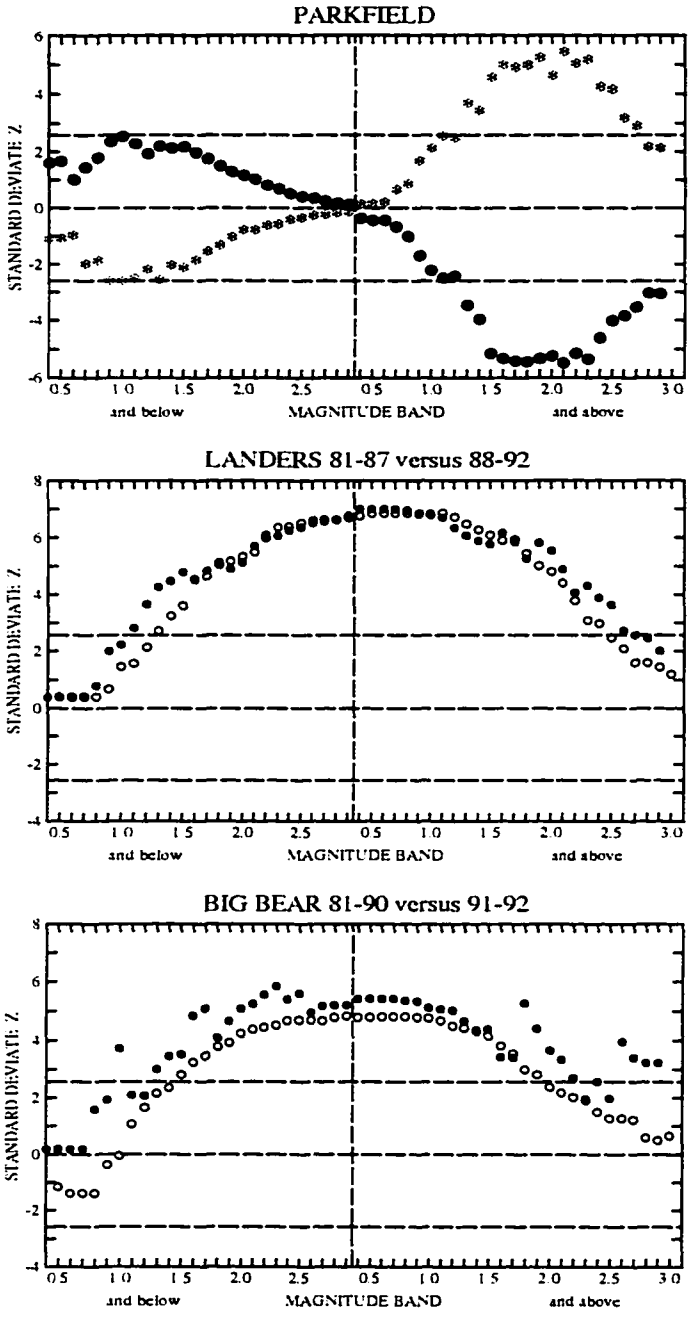

Figure 2.12. Magnitude signatures for the rate changes before the 1992 Landers (center) and Big Bear earthquake (bottom). The standard deviate z is plotted as a function of magnitude band, estimating the significance of the rate changes between the two periods given in the titles. Closed circles show the observed z-values. The open circles denote the synthetic magnitude signatures. For comparison the magnitude signature for the Parkfield false alarm, and for the return to normal, are shown in the top (flakes mark the false alarm in 1986, dots the return to normal in 1989). The patterns in the Parkfield case, with humps in the opposite directions in the two fields, are caused by a magnitude scale compression (flakes) and a subsequent extension (dots). Because the Landers and Big Bear signatures show only positive values, they cannot be interpreted as shifting or compressing of the magnitude scale.

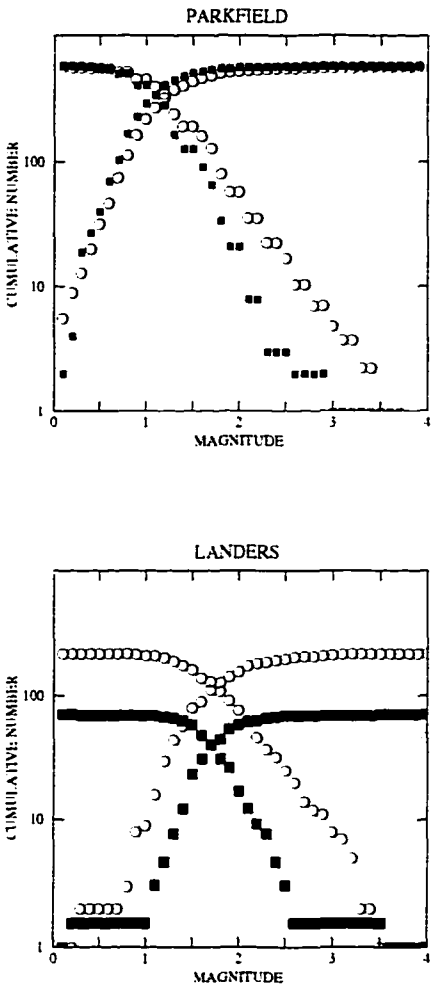

Figure 2.13. Frequency-magnitude plots for background and anomalous periods at Parkfield and Landers. Top: background period (solid symbol), compared to anomalous periods for the false alarm at Parkfield. Bottom: same for the anomalous volume at Landers. The Big Bear earthquake cannot be considered because of the 100% decrease in this case. The numbers during the anomalous periods were normalized to the length of the background period, so that the data from the two periods would plot as identical curves if no rate change took place in any magnitude band. At Parkfield the total rate (all M) did not change, while the rate of large events decreased. This was interpreted incorrectly as a b-value change coupled with quiescence, but we now know that compression of the magnitude scale was responsible for this change. The Landers case is different: the rates in all magnitude bands, including the total rate, decreased uniformly, with the b-value remaining approximately constant. A magnitude transformation cannot achieve the change in the Landers case. Thus, we propose that this change is a real anomaly.

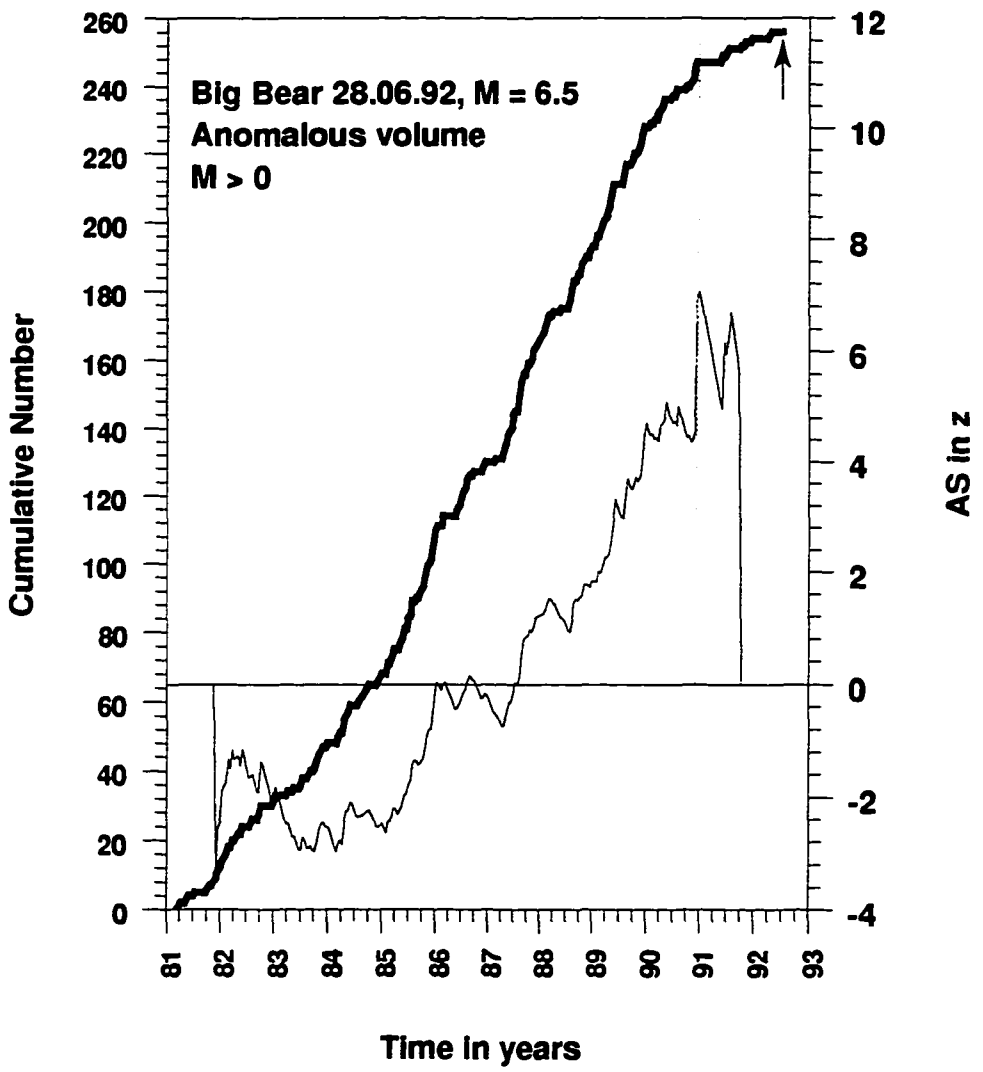

Figure 2.14. Cumulative number of earthquakes as a function of time in the anomalous volume around the Big Bear 1992 earthquake, defined in Figure 2.9. In this figure all events reported with a M > 0 are considered and no magnitude correction is applied to the declustered catalog. The thin line is the AS(t) function, the time of the Big Bear earthquake is marked by an arrow. The quiescence beginning in December 1990 is clearly visible, showing that we have not introduced it through our corrections.

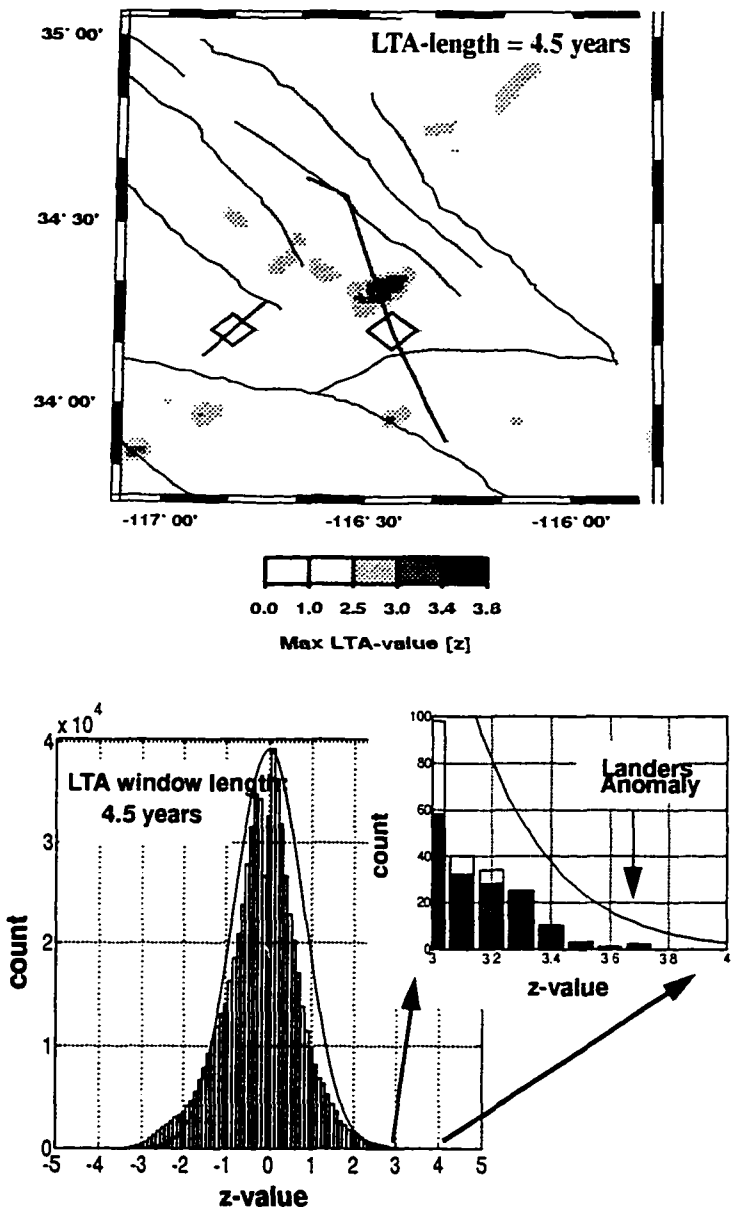

Figure 2.15. Map of the maximum z-values of all LTA functions with a window length of 4.5 years in the Landers area (upper Figure). The most outstanding anomaly is the quiescence before the Landers earthquake starting in January 1988. The bottom figure shows an histogram of z-values for the entire catalog, resulting from all possible comparisons of the mean rate within sliding time windows of 4.5 years length to the long term average over 11.3 years, calculated for each sub-volume. The positive tail of the histogram is magnified separately. The highest z-values in the entire catalog correspond to the Landers anomaly visible in the map in the upper Figure, and to the solid black values in the tail end of the histogram. The thin line in the histogram is a normal distribution with a standard deviation of 0.81 and the mean 0.

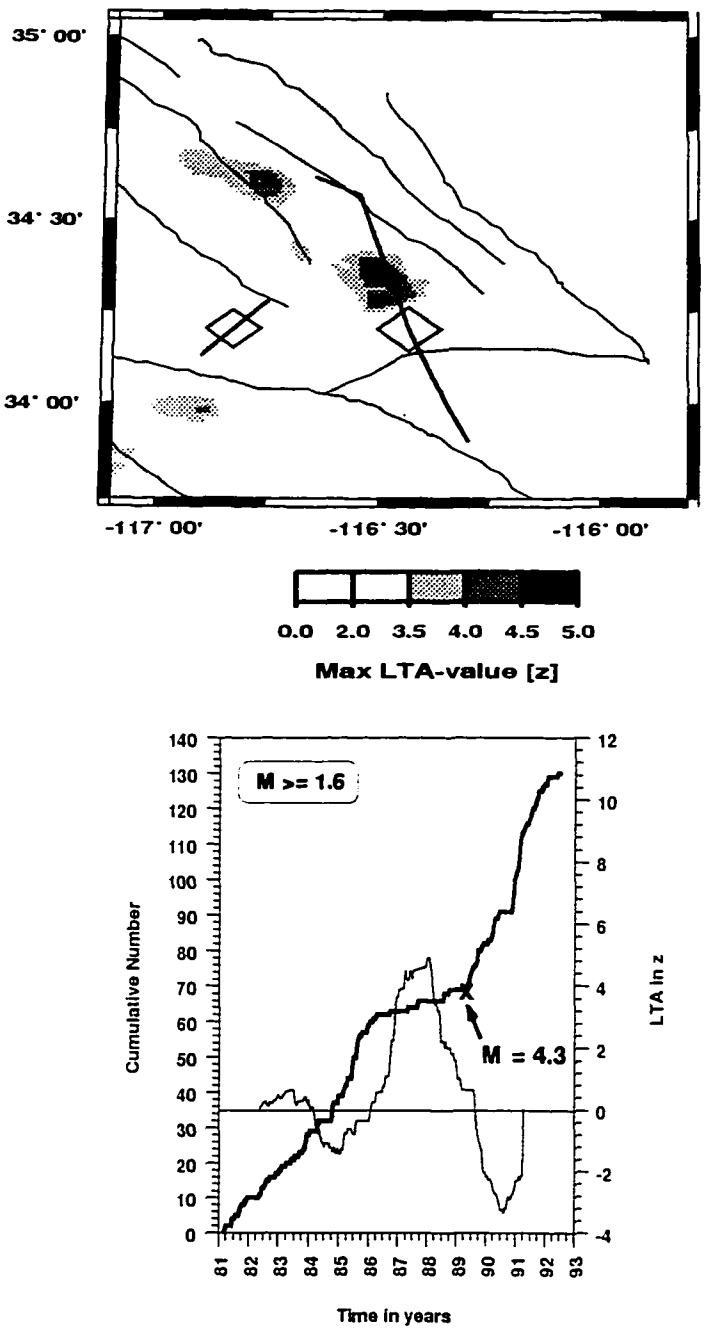

Figure 2.16. Map of the maximum z-values of all LTA functions with Tw= 3.0 years (upper Figure). The most outstanding anomaly is the quiescence before the Landers earthquake starting in January 1988. The cumulative number versus time plot for the second highest anomaly (arrow in the map) is shown in the bottom Figure. A significant decrease in the seismicity rate started in this volume in 1986 and was ended by a moderate earthquake (M = 4.3) on June 4 1989.

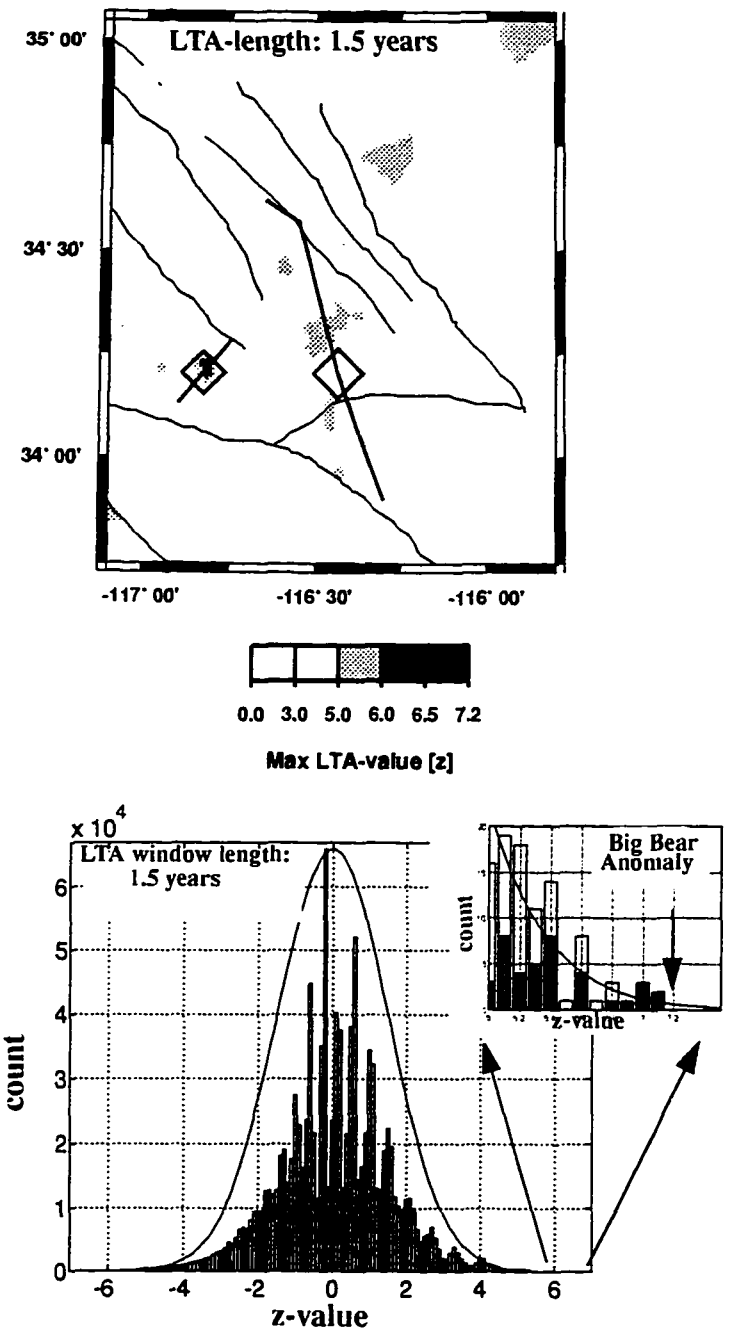

Figure 2.17. Map of the maximum z-values of all LTA functions with Tw=1.5 years (upper Figure). The most outstanding anomaly is the quiescence before the Big Bear earthquake starting in December 1990. The bottom Figure shows an histogram of z-values for the entire catalog, resulting from all possible comparisons of the mean rate within sliding time windows of 1.5 years length to the long term average over 11.3 years, calculated for each subvolume. The positive tail of the histogram is magnified separately. The highest z-values in the entire catalog correspond to the Big Bear anomaly, visible in the map in the upper Figure and to the solid black values in the tail end of the histogram. The thin line is a normal distribution with a standard deviation of 1.7 and the mean 0.

Chapter 3. Details of the Seismic Quiescence prior to the Landers 1992 Earthquake Sequence

3.1 Abstract

The M_w=7.3 Landers and M_w=6.2 Big Bear earthquakes were preceded by a seismic quiescence of 1.5 - 2.5 years. We map the extent of the quiescence using data from 15 km wide cross sections along- and across-strike of the ruptured faults. We identify two areas, each approximately 5 km wide, of significantly diminished seismicity in the vicinity of the Landers hypocenter, separated by a region of foreshock activity. The quiescence prior to the Big Bear earthquake coincides precisely with the hypocenter. The existence of a precursor to the Big Bear earthquake indicates that this earthquake should not be considered an aftershock to the Landers event, but a prematurely triggered independent event. The locations of quiescent volumes on the Landers fault correspond to areas of high moment release during the rupture. This observation supports the hypothesis that areas of high stress, or asperities, are more likely to show seismic quiescence. Based on the correlation of quiescence with fault segments of known high stress, and the absence of quiescence in the segment with known low stress we propose that it is more likely that quiescence is due to dilatancy hardening than to slip-softening. We introduce a new technique to identify all false alarms above a given significance. An 'Alarm Cube' shows all alarms in the space time volume of investigation and allows the calculation of the total space time volume that is covered by alarms. For the Landers earthquake sequence, an alarm threshold of the standard deviate z = 6.5 can predict two out of three mainshocks with no false alarms and with less than 1% of the total space time volume covered by alarms. Based on the hypothesis of seismic quiescence, we propose an empirical relationship between the significance of a seismicity rate decrease, as measured by the standard deviate z, and the probability of an earthquake occurring.

3.2 Introduction

The 28 June 1992 M_w = 7.3 Landers earthquake, together with the Big Bear M_w = 6.2 'aftershock' on the same day and the M_w = 6.1 Joshua Tree earthquake on April 23, represent the most extensive and well recorded sequence of major seismicity in southern California (e.g. *Sieh*

et al., 1992; *Hauksson* et al., 1993). In a previous paper (*Wiemer and Wyss*, 1994) we have documented that seismic quiescences preceded the Landers and Big Bear earthquakes but not the Joshua Tree earthquake. We used a gridding technique to sample the seismicity in overlapping volumes containing a constant number of earthquakes. This enabled us to visualize the seismicity rate changes as an almost continuous function of space and time. However, our description was limited to a map view of the anomaly. In this paper we show recent progress in our software tools that allows us to sample the seismicity in cross section, and we apply this technique to the Landers sequence. We found that cross sections oriented along (or perpendicular to) the strike of faults reveal information not available in map views. For example, a seismicity rate decrease at depth can be obscured by a seismicity rate increase for shallow earthquakes, thus resulting in a map view indicating little change. In cross section the difference between two such contrasting volumes can be mapped. Since many large earthquakes initiate in the lower part of the seismogenic crust, seismic quiescence may be limited to deeper volumes in many cases.

We define the precursory quiescence hypothesis in the following way (*Wyss*, 1986; *Wyss and Habermann*, 1988a): a statistically significant decrease of the independent seismicity rate that occurs in a restricted segment of a seismogenic zone. The rate decrease is terminated by a mainshock and the quiescent volume covers all or major parts of the source volume. Previous case studies (*Wyss and Burford*, 1987; *Wyss*, 1986; *Wyss and Habermann*, 1988b; *Wyss and Fu*, 1989) typically show a decrease in the seismicity rate of 50-70%, with anomaly durations of one to several years. The rate decrease should be present in all magnitude bands above the minimum magnitude useful for analysis, otherwise it is suspected that the anomaly may be artificial.

3.3 Data

We use the Southern California earthquake catalog provided by the California Institute of Technology and the USGS for studying the seismicity rate in the Landers region. Figure 3.1 shows a map view of the seismicity for the period March 1 1981, to June 27, 1992, and the location of the three cross sections along and perpendicular to the strikes of the Landers and Big Bear faults used in this study. Only the independent seismicity is shown, as the data were declustered using a modified version of *Reasenberg's* (1985) algorithm (*Wiemer and Zúñiga*, 1994). We did not apply to the catalog any corrections for suspected magnitude shifts. The minimum magnitude cutoff used to avoid fluctuations in reporting of small events was M_{min} =

1.6.

3.4 Method

The main advantage of sampling the seismicity using a gridding technique is that one can create an almost continuous visualization of seismicity rate changes in any volume, without relying on a few arbitrarily chosen polygons (*Wiemer and Wyss*, 1994). It is possible to detect all false alarms above a given significance by software which is part of a larger package, ZMAP, to investigate seismicity rate changes (available via anonymous ftp; *Wiemer and Zúñiga*, 1994). The 15 km wide cross sections were obtained using a Lambert projection, sampling the seismicity in overlapping volumes containing 50 earthquakes each and using a grid with a 1 km spacing. The significance of seismicity rate changes in each volume at time t can be measured using the standard deviate z-test (Habermann, 1983).

$$z(t) = \frac{R_1 - R_2}{\sqrt{\frac{\sigma_1}{n_1} + \frac{\sigma_2}{n_2}}} \qquad (1)$$

R_1 is the mean rate in period 1 (from t_0 to t), R_2 the mean rate in period 2 (from t to $t+t_{wl}$), where t is the 'current' time ($t_0 < t < t_e$) and t_{wl} a fixed window length (e.g. 1.5 years). σ_1 and σ_2 are the variances in these periods, and n_1 and n_2 the number of samples. We assign each z-value a color. Red colors indicate a seismicity rate decrease, blue a seismicity rate increase. Regions were the seismicity rate is too low (as measured by the radius of the cylinder containing 50 earthquakes) were excluded from the analyses.

3.5 Results

Figure 3.2 presents the cross sections along the strike of the Landers and Big Bear earthquakes. Using equation 1 we compare the seismicity rate in two periods: 1981.3 - 1990 and 1990 - 1992. Two regions of reduced seismicity (red) can be identified in the cross section along the strike of the Landers fault. The first anomaly is centered two kilometers south of the mainshock hypocenter at depths between five and ten km. Note that each grid-point samples the seismicity in a volume of up to eight kilometers in radius. Thus, the volume to the south of the

hypocenter, showing the strongest decrease in the seismicity (z = 6.7), includes the hypocenter. This anomaly starts abruptly in 1990 with a drop in the seismicity rate to zero for the following 2.3 years (2nd and 3rd cumulative curves at top of Figure 3.2). The second anomaly is centered 15 km to the north of the hypocenter at five kilometers depth, coinciding with the location of the 1979 M = 5.3 Homestead valley earthquake. This anomaly starts in 1988, with a further decrease in the seismicity rate in 1990 (2.5 years prior to the Landers mainshock, 1st cumulative curve at top of Figure 3.2). We are not able to extend our analysis more than 35 km to the north of the hypocenter, because the seismicity rate in this region from 1981 to 1992.5 is too low to allow detailed analysis (Figure 3.1).

Foreshock activity prior to the Landers earthquakes has been described by Dodge and Beroza (1996). Our analysis (Figure 3.2) reveals a region of increased seismicity above the hypocenter, just south of the quiescent volume. However, it is possible that this increase was caused by aftershocks of the Joshua Tree earthquake that have not been removed by the declustering algorithm. The cumulative number curve for the hypocenter region of the April 23 M_w = 6.1 Joshua Tree earthquake (pink cross) reveals no significant decrease in the seismicity rate. The seismicity stays remarkably stable over a period of 11 years in this volume (4th cumulative number curve at top of Figure 3.2).

The lower part of Figure 3.2 displays a z-value cross section along the strike of the Big Bear earthquake. A single outstanding anomaly (z = 6.7) coincides in space and time with the hypocenter of this mainshock (black asterix). The seismicity rate in this volume dropped to zero in 1990.5 and remained at zero until the mainshock. No foreshock activity can be detected in this case. A cross section perpendicular to the strike of the Landers fault (labeled C in Figure 3.1) is displayed in Figure 3.3. The width of the cross section was 30 km, and the number of events in each volume surrounding a grid point is 100. In this representation, the quiescence and the hypocenter (black star) coincide precisely. The quiescent volume has a width of approximately 20 km and is surrounded to the east and west by areas of stable or increased seismicity.

3.6 The 'Alarm Cube'

Important questions one has to answer when investigating precursors to earthquakes are: (1) how significant is the observed anomaly, (2) how many false alarms occur, and (3) what

percentage of space time is covered with alarms? We introduce a new technique to address these questions for the analysis of seismic quiescence: the 'Alarm Cube'. The seismicity is again gridded using 1km grid-spacing and seismicity rate changes are mapped at a time t using equation 1. The time t is stepped through the catalog in two week time steps. Therefore, we cover all of space-time with a three-dimensional grid (1km by 1km by 2 weeks). An alarm of length T_{alarm} is declared when the standard deviate z-value at one grid point exceeds a given threshold z_{alarm}. Figure 3.4 shows the result of such an analysis for the Landers region, using a LTA window length of 1.5 years, an alarm threshold of $z_{alarm} = 6.5$, and alarm length T_{alarm} of 1.5 years. A three dimensional view of the cube is shown at the left of Figure 3.4. The map of Southern California with faults and the 1992 rupture are plotted at the bottom. The rupture is plotted again at the top of the cube for reference. Time progresses from the bottom to the top of the cube. The beginning of each alarm is shown as a circle, with a line following it, marking the duration of the alarm. One can see that the alarms only occur towards the end of the time period and near the epicenters of the two large earthquakes. However, it is not easy to evaluate the exact location in time and space from the 3-D view. For this reason the alarm cube can be rotated in our software, and we present two additional views in Figure 3.4. The map view (center) shows that all alarms are located near the two 1992 rupture traces and the epicenters. The view with time and longitude as coordinates shows that all alarms occur before, and last up to, the two large earthquakes. From this analysis we conclude that at the chosen threshold for alarms only three alarm-groups occur, and that these are correlated in space and time with the two large earthquakes. Therefore, we propose that these periods of quiescence were precursors to these shocks.

We also use the alarm cube analysis to investigate the percentage of the total space time volume covered by alarms and thus judge the probability of an anomaly correlating with a mainshock by chance. We calculate the total space-time volume V_{total} as a sum over all grid points

$$V_{total} = \sum_{x,y,t} \pi R_{xy}^{2} T_{total} \qquad (2)$$

where $R_{x,y}$ is the radius of the circle containing 100 earthquakes at each grid-point and T_{total} is the time length of the catalog in years. The space-time volume V_{alarm} covered by alarms can be expressed as:

$$V_{alarm} = \sum_{x,\,y,\,t} \pi R^2_{x_{alarm}, y_{alarm}} T_{alarm} \qquad (3)$$

with T_{alarm} being the time length of the declared alarm. V_{alarm} is a function of the alarm threshold z_{alarm}. Both V_{alarm} and V_{total} contain individual volumes that are not independent but overlap in space and time. The percentage F of space time covered by alarms is consequently $F = \frac{V_{alarm} 100}{V_{total}}$, and is shown as a function of the alarm threshold z_{alarm} (Figure 3.5a). As an example, for an alarm threshold $z_{alarm} = 6.5$ only 0.2% of the total space time volume is covered with alarms.

To measure the performance of the algorithm, it is also necessary to estimate the number of successful predictions and the number of false alarms as a function of alarm threshold. We adopted the following rules to measure the false alarm and success rate:

(1) An alarm is declared if the z-value at a point $H_{(x,y,t)}$ exceeds the threshold z_{alarm}.

(2) If an alarm volume of radius R_{xy} contains a part of the rupture (two vertical planes along the surface ruptures defined in Figure 3.1) and lasts up to the main shock, it is considered a successful correlation, otherwise it is counted as a false alarm.

(3) The length of each alarm window is 1.5 years.

Using these definitions we calculated the ratio of successful predictions versus false alarms as a function of alarm threshold (Figure 3.5b). A 100% ratio means that all alarms were successes, no false alarms occur. For an alarm threshold $Z_{alarm} = 6.5$ we find that the success ratio is 91%, if we raise the alarm threshold to 7.4 no false alarms occur.

Although we detect 59 individual alarms at an alarm threshold of $z_{alarm} = 6.5$, these alarms

fall into groups (Figure 3.4). We define a number of alarms to be a group if they overlap in space and time. The alarm cube analysis will automatically identify all groups, which then can be investigated individually. We identify three alarm groups: the first surrounding the Big Bear epicenter, the other two to the north and south of the Landers epicenter. If we consider group alarms as the only significant alarms there are no false alarms. All groups are centered on parts of the 1992 rupture.

To estimate the chance correlation of the alarm volumes with the mainshocks we will define a precursor volume, V_{pre}. This is the volume (space-time) within which alarms are considered precursors, outside of it they are called false alarms. We accept an alarm as a success if the volume $R_{x,y}$ with $z \geq z_{alarm}$ overlaps with part of the faults and the mainshock occurs within the T_{alarm}. Using this definition V_{pre}=3.7% of V_{total}. Therefore, we would expect 3.7% of all alarms to correlate (according to our definition) with the mainshocks, if the alarms were distributed randomly in space-time. The actual success rate is 91% (for z_{alarm}=6.5, Figure 3.5b). Thus, we observe a 25 fold concentration of alarms in the precursor volume, as compared to a random distribution of alarms. Also, the probability of an M≅7 earthquake in the part of southern California studied is approximately 3 10^{-3} per 1.5 year window. Thus, the unique correlation of quiescence with the Landers earthquake has an exceedingly low probability to occur by chance. We therefore conclude that our observation of precursory seismic quiescence before the Landers and Big Bear earthquakes strongly supports the quiescence hypothesis, but it does not establish it as certain.

3.7 Probability Maps

In a first attempt to quantify the enhanced probability of an earthquake occurring based on the seismic quiescence hypothesis, we propose an empirical relationship between the significance of a seismicity rate decrease and the probability, p, of an earthquake occurring. We assume:

(1) if z < 2.57, the probability of an earthquake in the magnitude range of interest is the Poisson probability estimated from the long term rate λ_{lt}. For the case of the Landers earthquake λ_{lt} = 0.0024 per year (D. Jackson, personal communication, 1995).

(2) The probability for a large earthquake in locations with $z \geq 2.57$ is proportional to z.

(3) The maximum probability should reach values of about 0.5, based on the observation that the number of false alarms approximately equals the number of precursory anomalies.

Under these assumptions, we introduced the empirical relation:

$$p = 1 - \frac{1}{\exp(\lambda_{lt} + 0.03(z - 2.57)^2)} \qquad z > 2.57$$
$$p = 1 - \frac{1}{\exp(\lambda_{lt})} \qquad z \leq 2.57 \tag{4}$$

Using equation (4) we transform the z-value maps into probability maps. Figure 3.6 presents the probability cross sections based on the z-values in Figure 3.1. The maximum probability reaches a value of 0.45 in a volume coinciding with the Big Bear hypocenter, and 0.35 for the volume just south of the Landers hypocenter. We apply the same transformation to the z-values in map view (Figure 3.7). The time-cut shown compares the seismicity from 1981.3 - 1990.5 and 1990.5 - 1992.0 using equation 1 and a 1 km grid spacing. Four regions of increased probability can be observed (A-D in Figure 3.7), which correspond in space and time with the location of the Landers and Big Bear ruptures.

3.8 Discussion and Conclusions

To establish a phenomenon as a precursor one has to show convincingly that it correlates with large earthquakes and that the correlation is not likely due to chance. We submit that both of these conditions are fulfilled by seismic quiescence in the part of the southern California crust surrounding the Landers earthquake sequence of 1992. Previously we have shown that quiescence presented in a map view, without consideration of hypocentral depth, correlated with the epicenter of the Big Bear and the central portion of the Landers rupture (*Wiemer and Wyss*, 1994). This correlation, and the duration of quiescence for several years before and up to these two large earthquakes, were interpreted as evidence linking the two phenomena. The detailed

analysis of the seismicity rate in cross sections (Figures 3.2 and 3.3) makes the spatial correlation even more clear. The hypocentral volumes and the fault segments with the greatest moment release correlate with seismic quiescence.

In the case of the Big Bear earthquake the hypocentral volume coincides exactly with the crustal volume that became quiet about 2 years before the shock (Figure 3.2). The rupture was relatively simple and short (20 km), not multiple as in the case of Landers, and so was the quiescence which was centered on the rupture and included all of it, as seen in the cross section as well as in map view (Figure 3.9 of *Wiemer and Wyss*, 1994). We thus confirm our proposal that a quiescence precursor preceded the Big Bear earthquake. If one accepts that the seismic quiescence was a precursor to the Big Bear earthquake then one accepts the idea that some form of failure process was under way during 1990.5 to 1992.5. As a corollary this means that the Big Bear earthquake was due to occur within a relatively short time (one or two years) after 1992.5 even if it had not been triggered by the Landers main shock. In other words, the Big Bear earthquake was not an aftershock of the Landers main shock, but an independently ready event, possibly triggered prematurely by the Landers shock.

The Landers rupture was long (about 80 km) and complex, with varying slip and moment release along the fault (e.g. *Abercrombie and Mori*, 1994; *Cohee and Beroza*, 1994; *Wald and Heaton*, 1994; *Hudnut et al.*, 1994; *Freymueller et al.*, 1994). The seismicity pattern was also complex. The northernmost 25 km of the rupture could not be investigated because the seismicity rate was too low. The southernmost approximately 30 km did not show a rate change at any time, although it produced the M_w 6.1 Joshua Tree earthquake. The central 30 km of the rupture, surrounding the hypocenter, showed various degrees of quiescence. The sharpest and most significant quiescence was centered in a volume 5 km south of, and at depths equal to the hypocenter (Figure 3.2). The fault segment adjacent to the hypocenter and north of it showed somewhat longer lasting quiescence at depths shallower than the hypocenter. This fault segment was characterized by high moment release (e.g. *Cohee and Beroza*, 1994; *Wald and Heaton*, 1994; *Hudnut* et al., 1994; *Freymueller at al.*, 1994). We postulate that the correlation of seismic quiescence with the location of the initial rupture and a region of high moment release indicates that it was a precursor to the Landers main shock and we interpret its distribution along the rupture as follows. Quiescence occurred in the highly stressed segments of the fault, surrounding

the hypocenter and north of it. Based on the absence of quiescence in the southern 30 km of the rupture we suggest that the stress level there was comparatively low. The low stress level in the southern part is confirmed by the estimates of slip distribution along the fault. Further, our interpretation also agrees with the observation that the Joshua Tree earthquake was unable to trigger the Landers rupture, although the elastic energy was stored and ready to be released at the time, which means that the ambient stress in the southern part of the Landers rupture was relatively low.

From the correlation of areas of high moment release with the quiescence we conclude that the latter correlates with high stress volumes. Based on this observation we suggest that it is more likely that precursory quiescence is due to dilatancy than to a slip- or strain-softening process. In our interpretation the sharp reduction in the normally constant rate of earthquake production signals a change in process. The two most obvious processes that occur in rock failure in the laboratory that could cause this are slip-softening and dilatancy (e.g. *Wyss and Habermann*, 1988b). If precursory creep occurs along a fault segment, then the ambient stress in it will be lowered slightly and quiescence may result (e.g. *Stuart*, 1979, 1994) because small earthquakes that were ready to occur will be delayed in rupturing until additional stress is accumulated. Alternatively if dilatancy occurs the pore pressure will drop and the volume will strengthen (e.g. *Scholz et al.*, 1973; *Scholz*, 1988) not allowing earthquakes to occur at the same rate as previously. Based on the correlation of quiescence with fault segments of known high stress, and the absence of quiescence in the segment with known low stress we propose that it is more likely that quiescence is due to dilatancy hardening than to slip-softening.

The 'Alarm Cube' analysis (Figures 3.4 and 3.5) and the probability maps (Figures 3.6 and 3.7), are steps towards a rigorous test of the quiescence hypothesis. The alarm cube allows the identification of all anomalies in space-time above a given significance threshold. For the Landers sequence we were able to find an alarm threshold above which no false alarm occurs and for which two out of three mainshocks occur in a space-time volume containing an alarm. The percentage of the space time volume covered with an alarm is less than 1% for this alarm threshold.

The quiescence anomalies described by us earlier (*Wiemer and Wyss*, 1994) can be confirmed by viewing seismicity rate changes in cross section. We propose that in many cases a

cross section may provide a better way to visualize the seismicity rate changes in a fault system by revealing information masked in map views. In areas where the seismicity rate is sufficiently high, we will also attempt a true three dimensional (x,y,z) analysis of seismicity rate changes as a function of time. Although the focus of this paper is the analysis of seismic quiescence, the presented techniques (cross section analysis and the alarm cube) also provide advanced tools to investigate the homogeneity of earthquake catalogs and artificially introduced seismicity rate changes.

Acknowledgments: This work was supported by the U.S. Geological Survey Grant no. 1434-94-G-2388 and in part by the Wadati endowment at the Geophysical Institute of the University of Alaska Fairbanks. The authors would like to thank Hilary Fletcher, John Benoit, Doug Christensen, and John Lahr for helpful comments and corrections.

3.9 References

Abercrombie, R., and J. Mori, Local observations of the onset of a large earthquake: 28 June 1992 Landers, California, Bull. Seism. Soc. Am., 84, 724-734, 1994.

Cohee, B. P., and G. C. Beroza, Slip distribution of the 1992 Landers earthquake and its implications for earthquake source mechanics, Bull. Seism. Soc. Am., 84, 692- 712, 1994.

Dodge, and G. C. Beroza, Foreshocks to the 1992 M7.2 Landers earthquake, Bull. Seism. Soc. Am. in press, 1996.

Freymueller, J., N. E. King, and P. Segall, The co-seismic slip distribution of the Landers earthquake, Bull. Seism. Soc. Am., 84, 646-659, 1994.

Habermann, R. E., Teleseismic detection in the Aleutian Island arc, J. Geophys. Res., 88, 5056-5064, 1983.

Hauksson, E., L. M. Jones, and D. Eberhart-Phillips, The 1992 Landers earthquake sequence: seismological observations, J. Geophys. Res., 98, 19835-19858, 1993.

Hudnut, K. W., Y. Bock, M. Cline, P. Fang, y Feng, J. Freymueller, X. Ge, W. K. Gross, D. Jackson, M. Kim, N. E. King, J. Langbein, S. C. Larsen, M. Lisowski, Z. K.Shen, D. Svarc, and J. Zhang, Co-seismic displacements of the 1992 Landers earthquake sequence, Bull. Seism. Soc. Am., 84, 625-645, 1994.

Reasenberg, P. A., Second-order moment of Central California Seismicity, 1969-1982, J. Geophys. Res., 90, 5479-5495, 1985.

Rudniki, J. W., Physical models of earthquake instability and precursory processes,

PAGEOPH, 126, 531-554, 1988.

Scholz, C. M., L. R. Sykes, and Y. P. Aggarwal, Earthquake prediction: a physical basis, Science, 181, 803-810, 1973.

Scholz, C. H., Mechanism of seismic quiescences, PAGEOPH, 126, 701-718, 1988.

Sieh, K., L. Jones, E. Hauksson, K. Hudnut, D. Eberhart-Phillips, T. Heaton, S. Hough, K. Hutton, H. Kanamori, A. Lilje, S. Lindvall, S. F. McGill, J. Mori, C. Rubin, J. A. Spotila, J. Stock, H. K. Thio, J. Treiman, B. Wernicke, and J. Zachariasen, Near-field investigations of the Landers earthquake sequence, April to July 1992, Science, 260, 171-176, 1992.

Stuart, W. D., Strain softening prior to two-dimensional strike slip earthquakes, J. Geophys. Res., 84, 1063-1070, 1979.

Stuart, W. D., Diffusionless dilatancy model for earthquake precursors, Geophys. Res. Letts, 1, 261-263, 1994.

Wald, D. J., and T. H. Heaton, Spatial and temporal distribution of slip for the 1992 Landers, California, earthquake, Bull. Seism. Soc. Am., 84, 668-691, 1994.

Wiemer, S., and M. Wyss, Seismic quiescence before the Landers (M=7.5) and Big Bear (M=6.5) 1992 earthquakes, Bull. Seism. Soc. Am., 84, 900-916, 1994.

Wiemer, S., and R. F. Zúñiga, ZMAP - a software package to analyze seismicity, Supplement to EOS, Transactions, AGU, 75, 456, 1994.

Wyss, M., Seismic quiescence precursor to the 1983 Kaoiki (Ms = 6.6), Hawaii, earthquake, Bull. Seism. Soc. Am., 76, 785-800, 1986.

Wyss, M., and R. O. Burford, A predicted earthquake on the San Andreas fault, California, Nature, 329, 323-325, 1987.

Wyss, M., and Z. X. Fu, Precursory seismic quiescence before the January 1982 Hilea Hawaii earthquake, Bull. Seism. Soc. Am., 79, 756-773, 1989.

Wyss, M., and R. E. Habermann, Precursory quiescence before the August 1982 Stone Canyon, San Andreas fault, earthquakes, PAGEOPH, 126, 333-356, 1988a.

Wyss, M., and R. E. Habermann, Precursory seismic quiescence, PAGEOPH, 126, 319-332, 1988b.

3.10 Figures

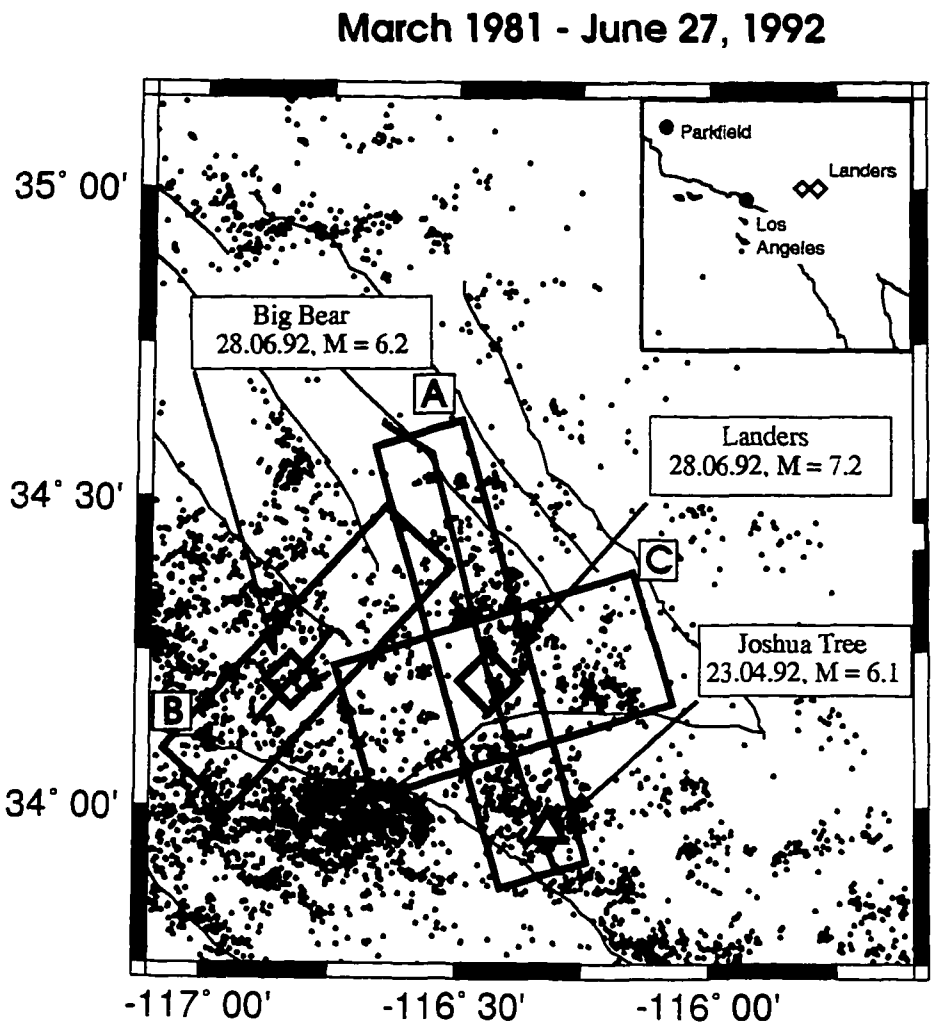

Figure 3.1. Epicenter map of the Landers area showing the epicenters of Landers 28.06.92 M_w = 7.3 mainshock (large diamond) and of the 28.06.92 M_w = 6.2 Big Bear aftershock (small diamond). For both earthquakes the rupture (based on the aftershock distribution) is plotted as a thick line. The epicenter of the Joshua Tree (23.04.92 M_w = 6.1) earthquake is marked by a triangle. The thinner lines correspond to other mapped faults. The small circles show the epicenters (M> 1.6) contained in the declustered catalog we used in our study (5655 events). The catalog spans the time from March 1981 to 27 June 1992. Marked as A,B, and C are the three cross sections presented in Figures 3.2 and 3.6.

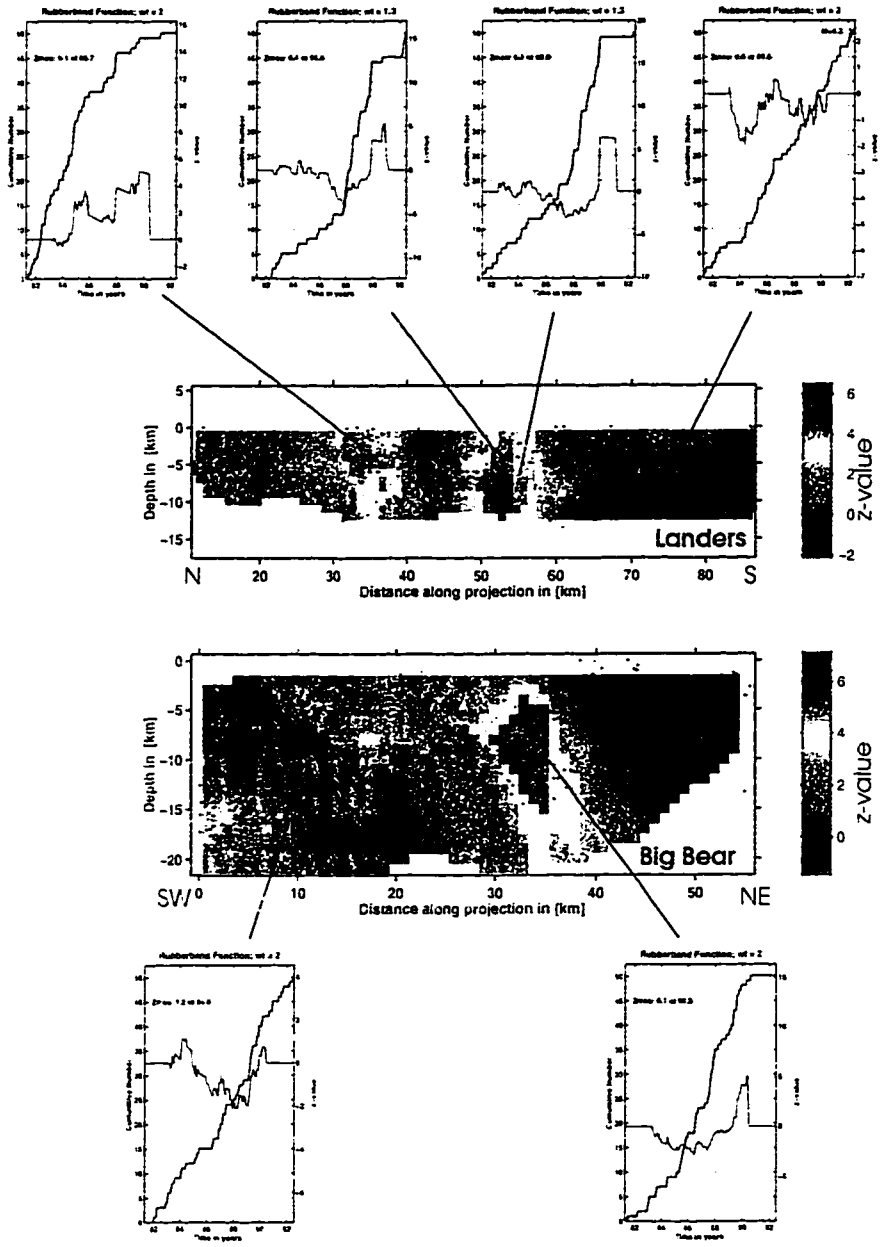

Figure 3.2. z-value cross sections along the strike of the Landers fault (top, profile A in Figure 3.1) and the Big Bear fault (bottom, profile B in Figure 3.1). Using the standard deviate z, we compare the seismicity rates from 1980.3 to 1990 to those from 1990 to 1992. Positive z-values (red) indicate a decrease in the seismicity rate, negative values (dark blue) an increase. The hypocenter location of the two mainshocks is marked by a black asterix, the hypocenter of the Joshua Tree earthquake is marked with a pink cross. Cumulative number plots containing 50 earthquakes are shown for six regions.

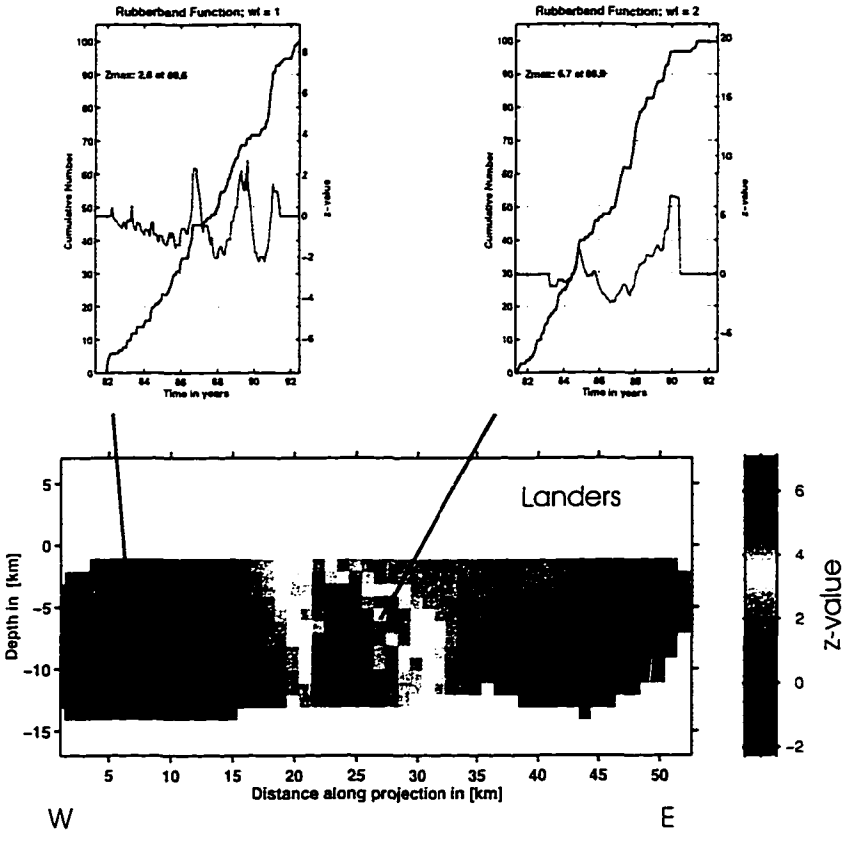

Figure 3.3. z-value cross section, perpendicular to the Landers fault(profile C in Figure 3.1). Cumulative number plots containing 50 earthquakes are shown for two regions.

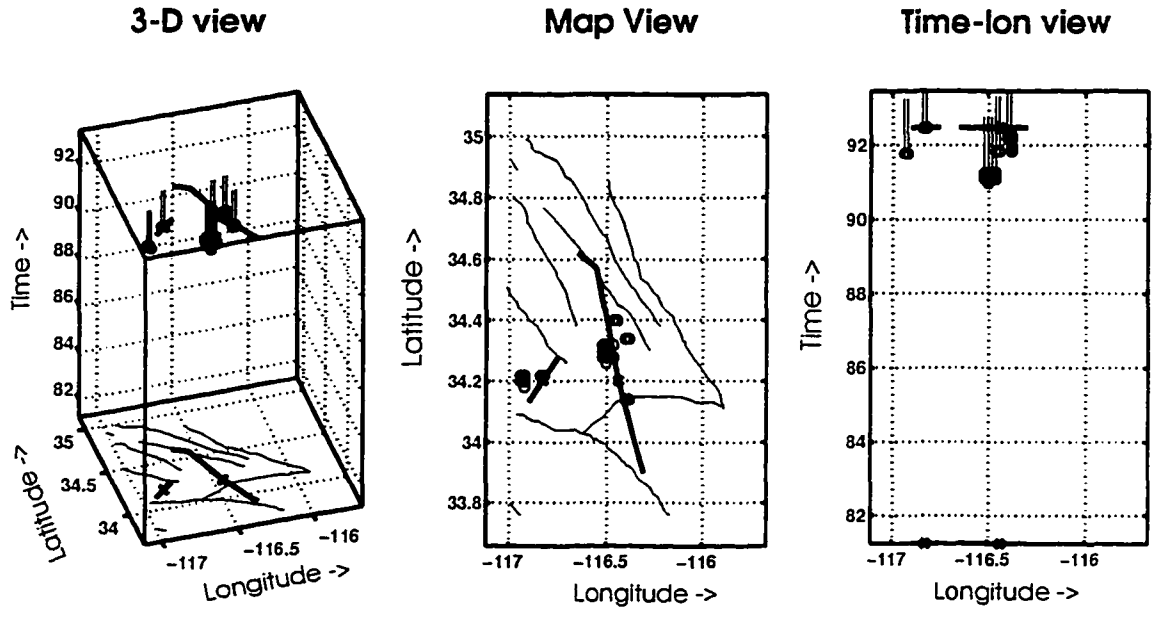

Figure 3.4. Alarm cube for the Landers region in three different orientations. The cube represents a space time volume (longitude, latitude and time). An alarm is declared when the standard deviate z exceeds the threshold of $z_{alarm} = 6.5$. The beginning of the alarm is indicated by a circle, the duration of the alarm (1.5 years) corresponds to the length of the 'tail'. Thick lines represent the Landers and Big Bear ruptures.

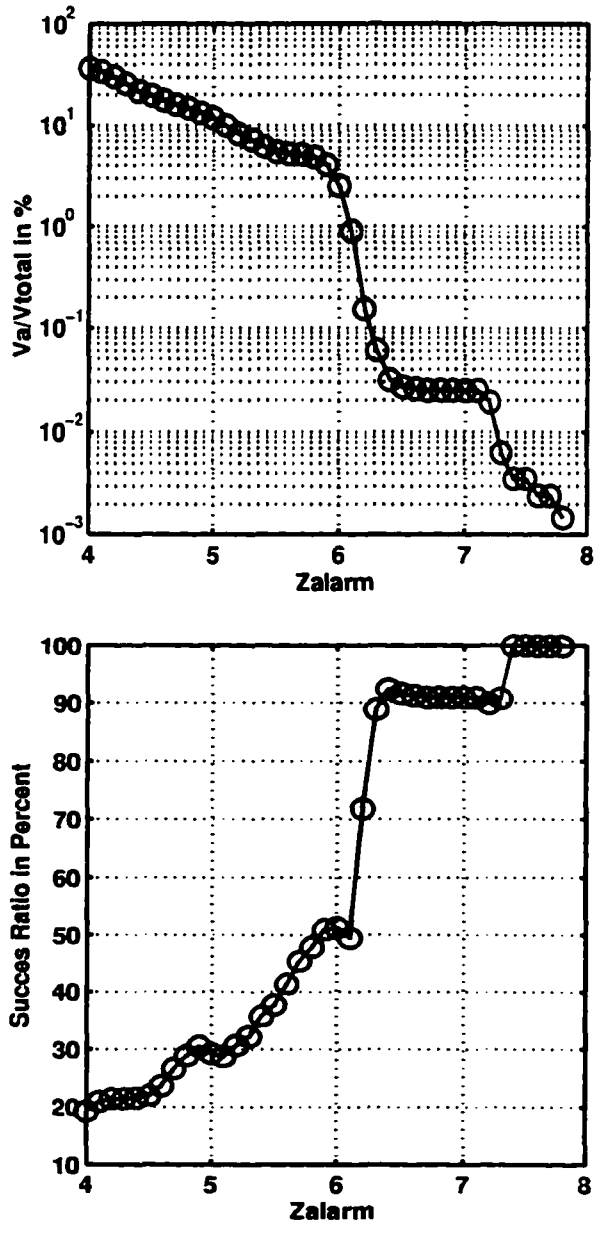

Figure 3.5. Space time volume covered by alarms as a function of alarm threshold (top). Bottom: ratio of successful alarms to false alarms in percent as a function of alarm threshold.

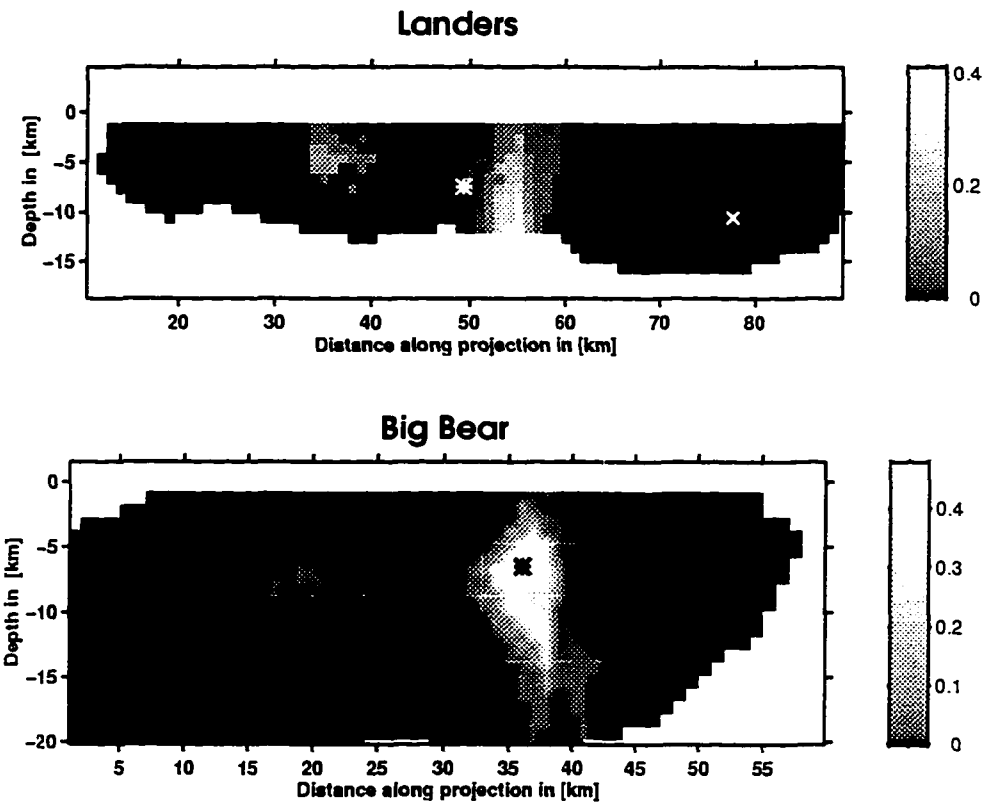

Figure 3.6. Probability distribution derived from the two z-value cross sections shown in Figure 3.2. Using an empirical relation (equation 4) we transformed the z-value at each grid point into the probability of an earthquake occurring based on the seismic quiescence hypothesis.

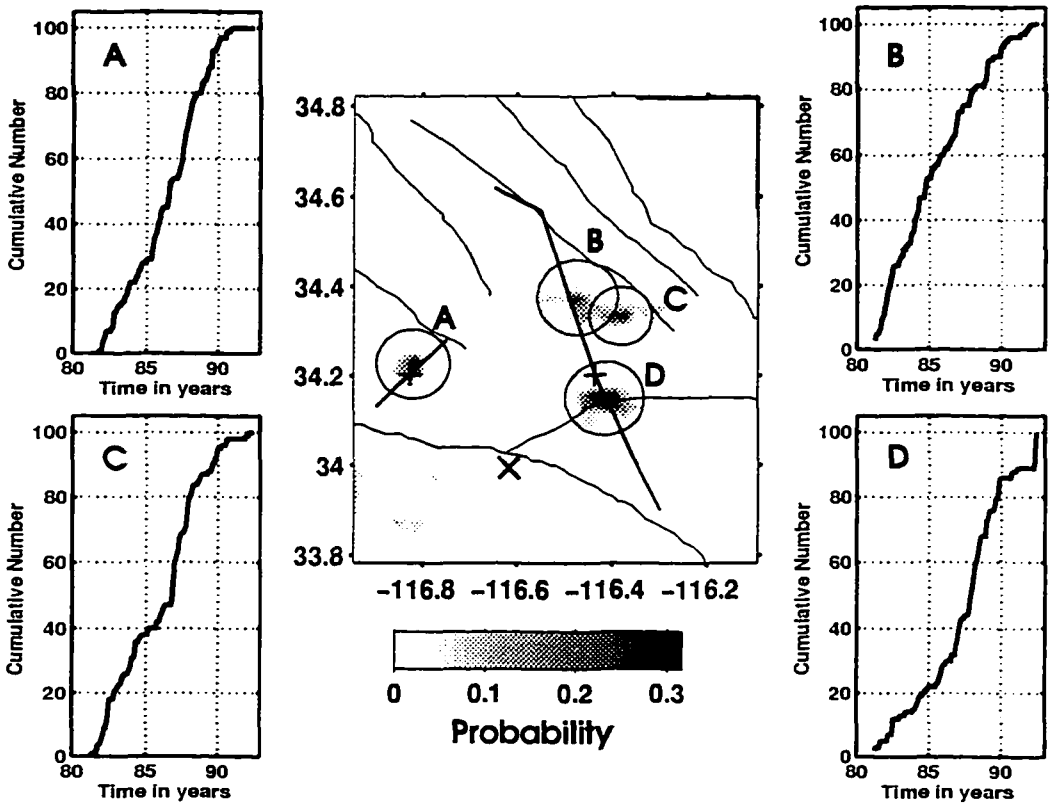

Figure 3.7. Map view of the probability function. The z-values have been calculated using a window length of 1.5 years and the two time periods compared are 1981.3 -1990.5 and 1990.5 - 1992. Using an empirical relation (equation 4) we transformed the z-value at each grid point into the probability of an earthquake occurring based on the seismic quiescence hypothesis. Cumulative number plots (A-D) are shown for four anomalous regions, where the circles in the map contain 100 earthquakes each.

Chapter 4. Mapping the *b*-value Anomaly at 100 km Depth in the Alaska and New Zealand Subduction Zones[1]

4.1 Abstract.

A positive anomaly in the frequency-magnitude distribution (b-value) is detected at approximately 90-100 km depth in two subduction zones. The *b*-value in this anomalous zone is 40% higher than in adjacent volumes. We use regional catalogs with a magnitude of completeness of 2.6 (Central Alaska and Cook Inlet), 2.0 (Shumagin Islands), and 3.5 (New Zealand). To resolve the *b*-value as a function of space in more detail, we project all earthquakes onto planes perpendicular to the strike of the slab. These cross-section views of the *b*-value distribution locate the high *b*-value anomalies at a depth of 90-100 km, on the upper surface of the Wadati-Benioff Zone. At these depths, slab dehydration may increase pore pressure, thus lowering the effective stress and increasing the *b*-value. Increased pore pressure would also lower the solidus in the overlying asthenosphere, giving rise to the volcanism that occurs directly above this zone.

4.2 Introduction

Arc volcanism in the Alaska and New Zealand subduction zones is strongly correlated with the 100 km depth contour of the Wadati-Benioff Zone (*Gill*, 1981). This observation, combined with petrological evidence for the source-depth of arc volcanism, has led to the widely accepted concept that dehydration of the subducting oceanic crust at about 100 km depth provides fluids necessary to lower the solidus of the overlying mantle. In this study we document that an anomaly in the frequency-magnitude (f-m) distribution of earthquakes exists at this depth.

Many studies of the f-m distribution as a function of time, space, and depth have been conducted since *Ishimoto and Iida* (1939) and *Gutenberg and Richter* (1954) introduced the relation between the frequency of occurrence and magnitude of earthquakes: $log_{10}N=a-bM$, where N is the cumulative number of earthquakes having magnitudes larger than M, and a and b are constants. Various methods have been suggested to measure both b and its confidence limit (*Bender*, 1983;

---

1. Stefan Wiemer and John P. Benoit, Geophys. Res. Lett., 23, 1557-1560, 1996.

Shi and Bolt, 1983). *Anderson et al.* (1980) investigated the *b*-value as a function of depth beneath northern Japan and showed an increase in *b* at 70-90 km depths, which, according to them may indicate the depth of the amphibolite to eclocite phase transformation within the subducted oceanic crust. However, the data available to *Anderson et al.* (1980) were limited and they used relatively few earthquakes to estimate the *b*-value. *Frohlich and Davis* (1993), using four different teleseismic catalogs, criticized Anderson's work and reported that they observed no systematic global variation of *b* with depth. They point out that *b*-value changes are often over-interpreted and are subject to numerous numerical and systematic errors. In this paper we re-visit the question of variation of *b* with depth. Our emphasis is to conduct a high resolution study of the *b*-value distribution using data from three regional seismograph networks. We focus our study of the Alaska and New Zealand subduction zones in the depth range 70-130 km, the depth believed to be the source region of arc volcanism (*Gill*, 1981).

4.3 Data and Method

Data from three regional seismograph networks are used: Central Alaska and the Cook Inlet region, Shumagin and Unalaska region, and New Zealand. All catalogs used M_L. We determined for each catalog the magnitude of completeness (M_c) as a function of space and time. Assuming a constant *b*-value, M_c was determined by visually inspecting f-m distributions for a variety of subsets in space and time. We also mapped M_c using the maximum of the derivative of the f-m distribution as a first order approximation of the magnitude of completeness. In addition, we tested the catalogs for major artificial changes in the magnitude reporting. Using these criteria the following data-sets were selected: *(1) Central Alaska and Cook Inlet* (Figure 4.1a): This catalog is compiled by the Alaska Earthquake Information Center (AEIC) (*Fogleman et al.*, 1996) and covers the period from June 1989 to June 1995. The station distribution of the network provides good coverage for Central Alaska and Cook Inlet, with M_c increasing south-west of Iliamna volcano. Therefore, we excluded earthquakes west of 153.5°W. Although the catalog is for the most part complete down to magnitude 2.2, we chose a magnitude threshold of $M_L \geq 2.6$ to accommodate the increase of M_c with depth and towards the West. Because the relative and absolute location uncertainty, especially in depth, decreases for larger events, a conservative estimate of M_c appears sensible. Our final catalog contained 1622 earthquakes, the largest catalog we investigated. *(2) Shumagin and Unalaska Islands* (Figure 4.1a): We used the catalog compiled by the Lamont-

Doherty Earth Observatory. *Abers* (1994) gives a detailed description of the seismographic network and the catalog quality. The most reliable section of the catalog spans the period June 1980 to January 1989. We estimated M_c = 2.0 for the depth range 70-130 km, leaving 323 events for this study. *(3) New Zealand* (Figure 4.1b): We used the catalog from January. 1988 to August 1994, compiled by the Seismological Observatory, Institute of Geological & Nuclear Sciences in New Zealand (*Anderson and Webb*, 1994). We found M_c=3.5, leaving 956 events for our study.

We calculated the *b*-value by both the maximum likelihood and the weighted least squares methods (*Bender*, 1983; *Shi and Bolt*, 1983). For samples larger than 100 events and magnitudes that span more than two magnitude units, both methods give almost identical results and differences between the two methods usually indicate that the M_c value is too small. A sliding spatial window is used to analyze the *b*-value as a function of depth. Windows contain 150 or 75 events and are moved forward by increments of 10% of the window length (15 or 7 events).

To visualize the spatial distribution of *b*-values in more detail, we project all earthquakes onto a vertical plane perpendicular to the strike of the trench. We sample the seismicity in cylindrical volumes containing 100 earthquakes each centered on one grid-element of a 1 by 1 km rectangular grid. A *b*-value is calculated for each volume and then assigned a color. Red colors indicate a high *b*-value, blue a low *b*-value. During our analysis we interactively confirmed anomalous regions by inspecting the f-m distributions and the fits to the curve. We use a constant number of earthquakes in each volume rather than constant volumes in order to be able to meaningfully compare the *b*-value between different volumes. We can map the radius of each cylindrical volume sampled as a measurement of the resolution of our investigation. For a detailed description of the gridding technique used we refer to *Wiemer and Wyss* (1994). The software used, ZMAP, is part of a software package to investigate seismicity rate changes. ZMAP is available via anonymous ftp (*Wiemer and Zúñiga*, 1994).

4.4 Results

For the AEIC catalog, we calculate an overall *b*-value of 0.95 ±0.04. The *b*-value as a function of depth for this region is shown in Figures 4.2a and b. The highest *b*-value, b=1.27 is calculated from an 8.5 km wide window centered at 97 km depth containing 150 events. Note that the maximum likelihood and least squares estimates for the same data set (Figures 4.2a and b) are almost

identical. We varied the number of events in each slice as well as M_c, to verify that this peak is stable and does not depend on the choice of parameter. To confirm our result, we tested two additional catalogs covering the same region: The first catalog, covering a different time period (USGS catalog from 1972-1987, *Fogleman et al.*, 1993), showed a high *b*-value at the same depth. The second catalog, composed of relocated hypocenters from the AEIC (*Ratchkovsky*, 1995) showed an anomaly at 105 km depth.

For the Shumagin region, we calculate an overall *b*-value of 0.84 +0.08. Again, we observe a peak in the *b*-value distribution (Figure 4.2c). The highest *b*-value, $b=1.12$ is calculated from a 17 km window centered at 98 km depth containing 75 events. Due to the small number of events in the catalog, the depth resolution is poor and we detect a broad peak spanning a depth range from 95-110 km. The New Zealand catalog shows the highest overall *b*-value of 1.14±0.13. The shape of the *b*-value with depth curve matches the two other regions closely. A peak value ($b=1.45$) is observed at a depth of 96 km. The 150 earthquakes of this anomalous population cover the depth range 91-103 km (Figure 4.2d).

Two cross-section views were analyzed for the AEIC catalog (Figure 4.3). The location of the cross-sections is shown in Figure 4.1a. The first cross-section transects the Cook Inlet region and contains the active volcanoes Mt. Iliamina and Mt. Augustine. The second profile transects the northern edge of the WBZ (Mt. McKinley region), where no major volcanism has occurred during the Holocene. Both profiles show a region of higher *b*-values at a depth of 90-100 km, located in the upper part of the WBZ. A second region of high *b*-value is identified at a depth of 70-80 km. We show the f-m distribution for two volumes (marked 1 and 2 in Figure 4.3) to demonstrate that the change is not a subtle effect that can be explained by numerical variation in estimation of b. The two distributions (Figures 4.3a and 4.3b) are clearly different for all magnitude bands considered and follow closely the linear Gutenberg-Richter relation. The distributions are significantly different at the 95% confidence level based on an F-test.

The cross-section view analyses for the Shumagin Islands region (Figure 4.3c) and New Zealand (Figure 4.3d) show high *b*-value anomalies in the upper part of the WBZ at depths of about 90-100 km. For the New Zealand catalog a second anomaly at 70-80 km is visible (Figure 4.3c). In addition to the described high *b*-value anomalies it appears that the *b*-value for all four

cross-sections is higher for the upper plane of the WBZ.

4.5 Discussion and Conclusions

Does the f-m distribution vary significantly with depth? We have shown (Figures 4.2 and 4.3) that the answer to this question must be 'yes' for the three regions under investigation. We observe a 30-40% increase of b at depths of 90-100 km. Two different analysis techniques show this anomaly: analyzing the earthquakes as a function of depth (Figure 4.2) and in cross-section (Figure 4.3). We believe that the cross-section view analysis is the superior approach if a sufficient number of earthquakes permits a detailed analysis. Cross-sections allow resolution of the distribution of b in two dimensions, whereas the depth slice analysis is only one dimensional. A depth slice at 90-100 km results in sampling the earthquakes in a high and a low b-value region, thus mixing two different populations. We calculated b-values in cross-sections parallel to the strike of the slab in an attempt to map out the lateral extent of the anomalies, but the results were inconclusive.

The same qualitative behavior of the f-m distribution as a function of depth is observed in three regions in two subduction zones, using data from three independent seismograph networks. This provides strong evidence that these anomalies are related to a general phenomenon associated with the subduction process. Although it may be difficult to compare absolute b-values between different seismic networks and tectonic regimes, the relative behavior of the magnitude-frequency distribution as a function of depth for each network is less likely to be influenced by systematic differences in magnitude reporting. For the AEIC catalog we investigated in detail the possibility that the changes could be correlated with artificial changes in the magnitude reporting or earthquake locations. For the selected data-set we found an average RMS residual of 0.22 s, an average 32 stations reporting, and an average location uncertainty measured by the axis of the hypoellipse error ellipsoid of 1.6 km horizontally, and 3.5 km vertically. We did not find an anomalous or irregular behavior that correlated with the described changes in the f-m distribution for any of these quality parameters. The average radius of the cylindrical volumes used in the cross-section analysis for the AEIC catalog was 5.4 km. Although we cannot estimate the accuracy of the magnitudes reported, we did investigate the homogeneity of magnitude reporting as a function of time and space, and found no major changes for the depth range in question.

Changes in the f-m distribution have been related to material heterogeneity (*Mogi*, 1962),

effective shear stress (*Scholz*, 1968; *Wyss*, 1973), and temperature (*Warren and Latham*, 1970). One or more of these factors may be responsible for the observed *b*-value anomaly: (1) Material heterogeneity: The strength of the plate may be affected by dehydration embrittlement (*Kirby et al.*, 1990) thus changing the frequency magnitude distribution. However, a mechanism to change the fabric of the subducting plate at the anomalous depth and a reversal of this change at greater depth is difficult to envision. (2) Temperature: The thermal structure of the subducting slab is a subject of some contention. There have been many differently calculated thermal-structures published for subduction zones that we may conclude either that the thermal structures are not yet known in detail or that there is considerable variation (*Wyllie*, 1988). The subducted oceanic crust may be relatively warm due to shear heating and heat flux (*Ponko and Peacock*, 1995), or significantly cooled by endothermic dehydration reactions (*Anderson et al.*, 1980). However, one might expect a more gradual, monotonous change in *b* as a response to the change in the thermal regime.

(3) Stress: An increase in pore pressure leads to a decrease in the effective stress and an increase in *b*. The increase in pore pressure may be due to the dehydration of hydrous minerals within the slab. This dehydration would be expected to take place within a limited depth range, in agreement with our observations. Several candidate reactions releasing large amounts of water have been proposed, including the greenschist-amphibolite-eclogite (*Wyllie*, 1988), and the blueschist-eclogite (*Peacock*, 1993) facies changes. This water may then trigger partial melting in the overlying mantle. The location of the high *b* anomaly on the upper surface of the WBZ and directly below the volcanic front is strong indirect evidence that high *b* is associated with high pore pressures or low effective stress (*Anderson et al.*, 1980). However, the positive *b*-value anomalies can be observed even without surface volcanism. Examples include the anomalies at 70-80 km depth as seen in cross-section (Figure 4.3) and underlying Mt. McKinley (Figure 4.3b). This may indicate that while dehydration of the slab is a general feature of the subduction process leading to high *b*-values, only in some regions the combined effects of temperature, pressure, and the presence of water are sufficient to initiate partial melting of the overlying mantle. Further analysis might resolve the differences in the behavior of *b* in active volcanic regions and non-active regions in more detail.

Anomalous non down-dip-extension (non DE) earthquakes have been observed underneath the volcanic arc by several authors (*Iguchi and Ishihara*, 1995; *Comte and Suárez*, 1994). The loca-

tions of these non DE earthquakes correspond roughly with the described *b*-value anomalies and one might speculate that they are caused by the same mechanism. The anomalous non DE earthquakes may indicate a perturbation in the local stress field, which in turn may explain the change in the f-m distribution. To address this question in more detail it would be useful to perform stress tensor inversions for the earthquakes in the anomalous region. *Lu and Wyss* (1996) studied the stress directions in the Alaska subduction zone in great detail. They detected no change in the orientation of the stress field within the anomalous volume at 100 km depth. However, only few well-constrained focal mechanisms were available for their study.

In summary, our results indicate that a region of anomalously high *b*-value exists at a depth of 90-100 km in two subduction zones. This anomaly appears to be the result of a fundamental process connected with the subduction of the slab and the creation of the volcanic arc.

Acknowledgments: The authors would like to thank M. Wyss, H. Fletcher, S. McNutt, J. Lahr, and two anonymous reviewers for reviewing the manuscript. Additional thanks to the Alaska Earthquake Information Center, the Lamont-Doherty Earth Observatory, the Institute of Geological & Nuclear Sciences in New Zealand, and N. Ratchkovsky for supplying the catalogs used in this study. Support for this work has partly been provided by the Wadati endowment of the Univ. of Alaska Fairbanks Geophysical Institute and the Alaska Volcano Observatory.

4.6 References

Abers, G.A., Three-dimensional inversion of regional P and S arrival times in the East Aleutians and sources of subduction zone gravity highs, *J. Geophys. Res.*, *99*, B3, 4395-4412, 1994.

Anderson, H., and T. Webb, New Zealand seismicity pattern revealed by the upgraded National Network, *N.Z. J. Geol. Geophys.*, *37*, 477-493, 1994.

Anderson, R.N., A. Hasegawa, N. Umino, and A. Takagi, Phase changes and the frequency-magnitude distribution in the upper plate of the deep seismic zone beneath Tohoku, Japan, *J. Geophys. Res.*, *85*, 1389-1398, 1980.

Bender, B., Maximum likelihood estimation of *b*-values for magnitude grouped data, *Bull. Seism. Soc. Am.*, *73*, 831-851, 1983.

Comte, D., and G. Suárez, An inverted double seismic zone in Chile: evidence of phase transformation in the subducted slab, *Science*, *263*, 212-115, 1994.

Fogleman, K.A., J.C. Lahr, C.D. Stephens, and R.A. Page, Earthquake locations determined by the Southern Alaska seismograph network for October 1971 through May 1986, *Open File Rep. 93-309*, 54 pp., USGS, 1993.

Fogleman, K.A., C.A. Rowe, and W.R. Hammond, Alaska earthquakes-1994, in *Geologic studies in Alaska by the USGS during 1994*, USGS Bull. 2152, edited by T.E. Moore and J.A Dumoulin., pp. 59-80, 1996.

Frohlich, C., and S. Davis, Teleseismic *b*-values: or, much ado about 1.0, *J. Geophys. Res., 98*, 631-644, 1993.

Gill, J., *Orogenic andesites and plate tectonics*, Springer-Verlag, New York, 390 pp., 1981.

Gutenberg, B., and C.F. Richter, Magnitude and energy of earthquakes, *Ann. Geof. 9*, (1), 1-15, 1954.

Iguchi, M., and K. Ishihara, Characteristic non-down-dip extension intermediate-depth earthquakes immediately beneath the volcanic front in South Kyushu, Japan, *Geophys. Res. Let., 22*, 1905-1908, 1995.

Ishimoto, M., and K. Iida, Observations sur les seisms enregistre par le microseismograph construit dernierment, *Bull. Earthquake Res. Inst. Tokyo Univ., 17*, 443-478, 1939.

Kirby. S., B.S. Hemingway, and R. Lee, Anomalous fracture and thermal behavior of hydrous minerals, in: *The brittle-ductile transition in rocks*, edited by Duba A.G., W.B. Durham, J.W. Handin, H.F. Wang, 119-126, 1990.

Lu, Z., and M. Wyss, Segmentation of the Aleutian plate boundary derived from stress direction estimates on fault plane solutions, *J. Geophys. Res., 101*, 803-816, 1996.

Mogi, K., Magnitude-frequency relation for elastic shocks accompanying fractures of various materials and some related problems in earthquakes, *Bull. Earthq. Res. Inst., 40*, 831-853, 1962.

Peacock, S., The importance of blueschist-eclogite dehydration reactions in subducting oceanic crust, *Geol. Soc. Am. Bull., 105*, 684-694, 1993.

Ponko, S.C., and S.M. Peacock, Thermal modeling of the southern Alaska subduction zone: Insight into the petrology of the subducting slab and overlying mantle, *J. Geophys. Res., 100*, 22117-22128, 1995.

Ratchkovsky, N.A., Relocation of earthquakes in the Cook Inlet area, south-central Alaska, using the joint hypocenter determination method, M. S. thesis, Univ. of Alaska, Fairbanks, 85 pp., 1995.

Scholz, C.H., The frequency-magnitude relation of microfracturing in rock and its relation to earthquakes, *Bull. Seism. Soc. Am., 58*, 399-415, 1968.

Shi, Y., and B. Bolt, The standard error of the magnitude frequency b value, *Bull. Seism. Soc. Am.*, *72*, 1677-1687, 1982.

Warren, N.W., and G.V. Latham, An experimental study of thermally induced microfracturing and its relation to volcanic seismicity, *J. Geophys Res.*, *75*, 4455-4464, 1970.

Wiemer, S. and M. Wyss, Seismic quiescence before the 1993 M=7.5 Landers and M=6.5 Big Bear (California) earthquakes, *Bull. Seism. Soc. Am.*, *84*, 900-916, 1994.

Wiemer, S., and R. Zúñiga, ZMAP-a software package to analysis seismicity (abstract), *EOS, Trans., AGU*, *75*, 456, 1994.

Wyllie, P., Magma genesis, plate tectonics, and chemical differentiation of the earth, *Rev. Geophys.*, *26*, 370-404, 1988.

Wyss, M., Towards a physical understanding of the earthquake frequency distribution. *Geophys. J. Roy. Astr. Soc.*, *31*, 341-359, 1973.

4.7 Figures

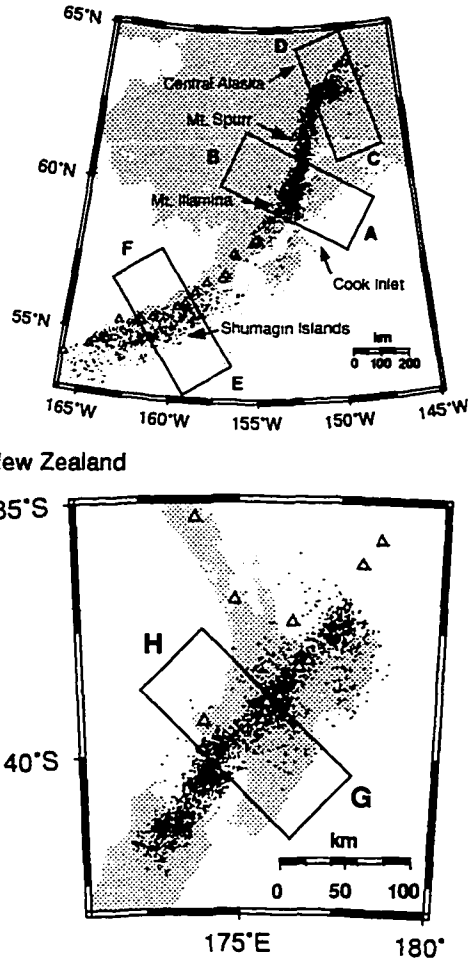

Figure 4.1. Epicenter maps of Alaska (a) and New Zealand (b) with active volcanoes (triangles) and epicenters of earthquakes (dots) used in this study. The rectangles indicate the locations of cross-sections used in Figure 4.3.

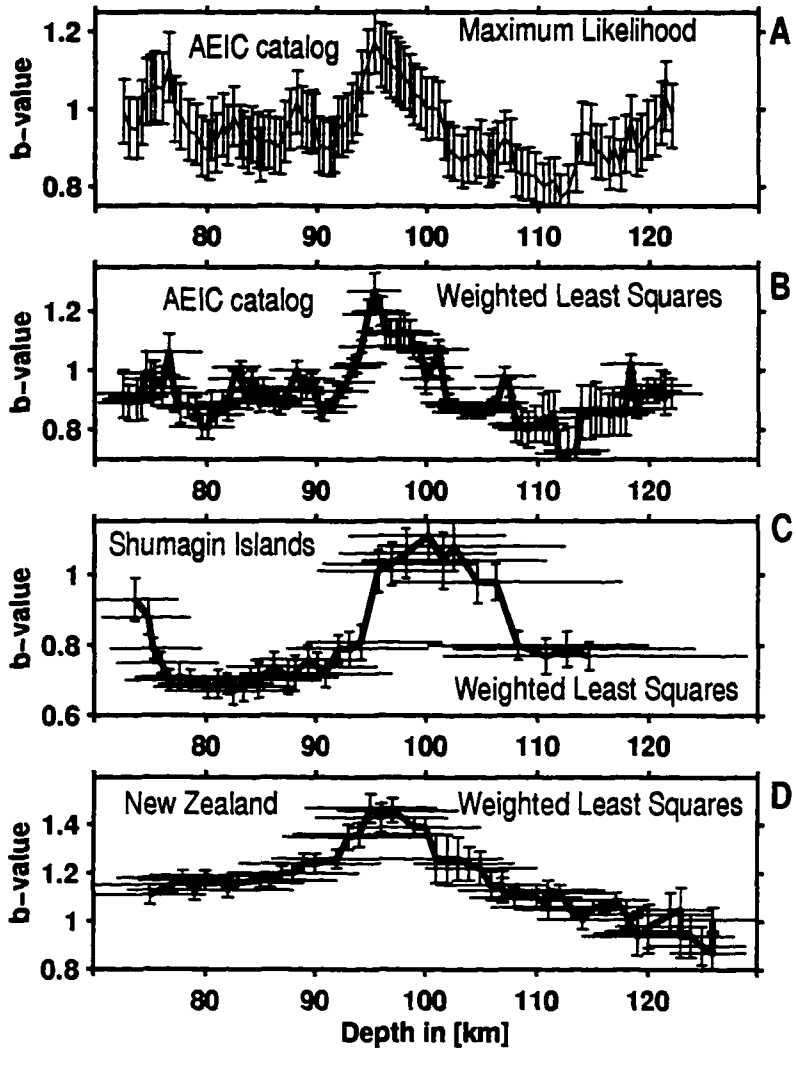

Figure 4.2. *b*-values as a function of depth in three subduction zones(a) AEIC catalog: the graph shows the *b*-values calculated using the maximum likelihood method, vertical bars represent the error-bars in the *b*-value, depth range sampled is the same as in (b). (b-d) same as (a) but *b*-values calculated using a weighted least squares method, horizontal bars indicate the depth range sampled. (b) AEIC catalog. (c) Shumagin catalog. (d) New Zealand catalog.

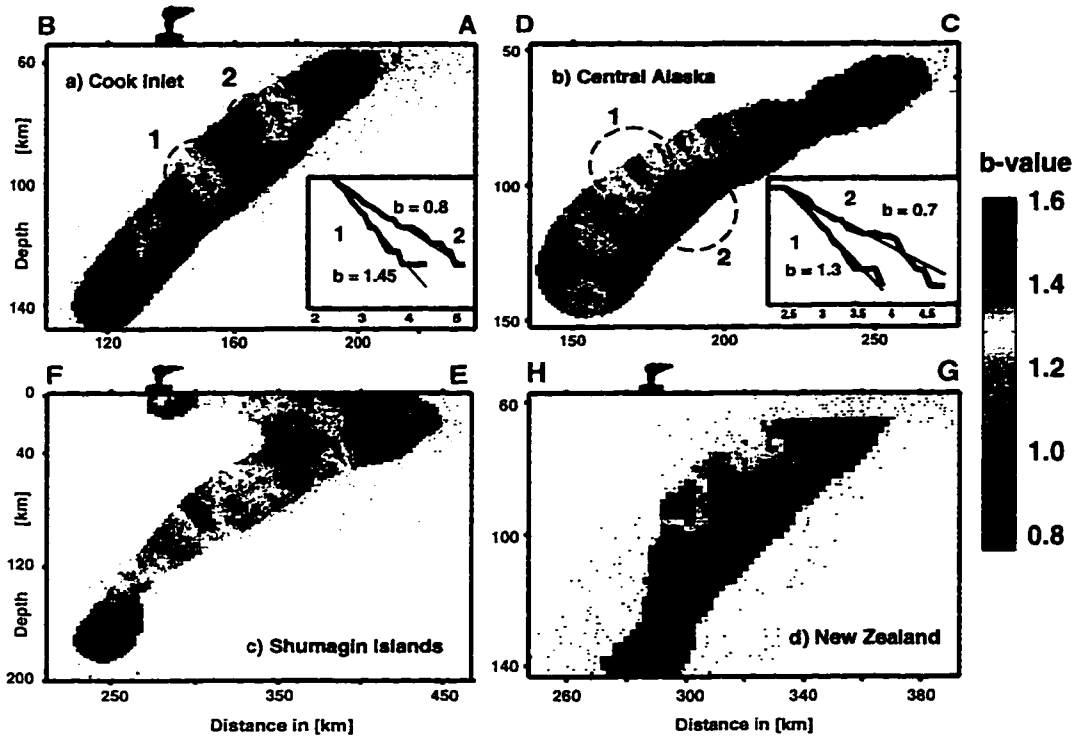

Figure 4.3. Cross-sections of the distribution of *b*-values through four subduction zone segments. Red indicates a high *b*-value. The location of the volcanic arc is indicated. (a) Cook Inlet Alaska along profile A-B (Figure 4.1a). For two volumes (1 & 2) the f-m distribution is shown. (b) Central Alaska along profile C-D (Figure 4.1a). (c) Shumagin Islands along profile E-F (Figure 4.1a). (d) New Zealand along profile G-H (Figure 4.1b).

Chapter 5. Variations in the Frequency-Magnitude Distribution with Depth in two Volcanic Areas: Mount St. Helens, Washington, and Mt. Spurr, Alaska[1]

5.1 Abstract

The frequency-magnitude distribution of earthquakes, characterized using the *b*-value, is examined as a function of space beneath Mt. St. Helens (1988-1996), and Mt. Spurr (1991-1995). At Mt. St. Helens, two volumes of anomalously high *b* (b >1.3) can be observed at depths of 2.6-3.6 km below the crater floor and below 6.4 km. These anomalies coincide with (1) the depth of vesiculation of ascending magma, and (2) the suggested location of a magma chamber at Mt. St. Helens. Study of Mt. Spurr reveals an area of high *b*-value ($b \geq 1.3$) at a depth of about 2.30-4.5 km below the crater floor of the active vent Crater Peak. We propose that the higher material heterogeneity in the vicinity of a magma chamber or conduit due to vesiculation of the ascending magma is the main cause of the increased *b*-value at shallow depths. Alternatively, interaction of magma with groundwater may have increased pore pressure and lowered the effective stress. The deeper anomaly at Mount St. Helens is likely caused by high thermal stress gradients in the vicinity of the magma chamber. Our results indicate that detailed mapping of the frequency-magnitude distribution can be used as a tool to trace vesiculation and locate active magma chambers.

5.2 Introduction

Many studies of the frequency-magnitude distribution (FMD) as a function of time, space, and depth have been conducted since *Ishimoto and Ida* (1939) and *Gutenberg and Richter* (1944) introduced the relation between the frequency of occurrence and magnitude of earthquakes:

$$log_{10}N = a\text{-}bM \qquad (1)$$

where N is the cumulative number of earthquakes having magnitudes larger than M, and a and b are constants. The slope, or *b*-value, of the FMD has been shown in laboratory studies, mines, and numerical simulations to depend on a variety of environmental conditions. Several authors explained variations in the FMD as being caused primarily by material properties such as hetero-

1. Stefan Wiemer and Stephen R. McNutt, submitted to Geophys. Res. Letters, June 1996.

geneity (*Mogi*, 1962), magnitude of applied shear stress (*Scholz*, 1968; *Urbancic* et al., 1992) or effective stress (*Wyss*, 1973), and temperature gradient (*Warren and Latham*, 1970).

Volcanic areas are commonly reported to have high *b*-values (e.g. *Warren and Latham*, 1970), and several authors have investigated *b*-value changes in volcanic areas as a function of time (e.g. *Zobin*, 1979). In the vicinity of magma chambers all three of the aforementioned mechanisms favor a high *b*-value. In general, volcanoes have high heterogeneity because of layering of lava flows and ash, the presence of cooling cracks, dikes and sills, and high thermal gradients in the vicinity of magma. Of course, in magma itself no earthquakes should be produced due to the limited shear strength of molten material. Magma chambers at stratovolcanoes are generally equant in shape, and on the order of 1-20 km^3 in size (*Iyer*, 1984). Their depths are mapped at about 5-20 km based on tomography, S-wave screening, and post-eruption seismicity (*Iyer*, 1984).

We chose Mt. St. Helens as our first target for detailed mapping of the FMD because its eruptions are some of the best documented, it has a high quality earthquake catalog, and the internal structure of the magmatic system has been studied by a number of researchers. We then applied our method to a similar volcano, Mt. Spurr in Alaska, where the volcanic plumbing system is largely unknown.

Although the interpretation of the *b*-value remains non-unique, we propose that a high resolution imaging of the spatial distribution of *b*-values helps to understand the volcanic plumbing system. A detailed view of the distribution of *b*-values will be presented in this paper. We will show that the two regions with anomalously high *b*-value coincide at both volcanoes with (1) the suggested locations of magma chambers and (2) the depth of vesiculation of the ascending magma. Finally, we will interpret the observed anomalies in a framework of material heterogeneity, stress, and temperature related effects.

5.3 Data

5.3.1. Mt. St. Helens

Volcano-tectonic (VT; also known as high frequency or A-type) events were selected from the earthquake catalog of the University of Washington. Following the results of *Moran* (1994) we decided to use data spanning the period 1988 through January 1996. During this time no major

eruptions occurred at Mt. St. Helens. The magnitude range is 0.4 to 2.8 and the events range in depth from 0 to 10 km. *Moran (*1994) explained the exponential decay in the number of events recorded as being caused by a re-pressurization of the magmatic system.

The overall *b*-value of the catalog from 1988 onward is 0.96±0.06, a value close to the average world-wide *b*-value observed in the seismogenic crust. Using FMD plots we estimate the magnitude of completeness threshold as M_{comp}=0.4; below this the number of events declines. We perform our analyses on the 1674 events with a magnitude ≥ 0.4, which occurred during the period January 1988 to January 1996. We chose zero depth for Mount St. Helens data as the crater floor of the volcano (1.9 km above sea level). (In the notation of the Cascade Volcano Observatory (CVO), zero depth is at 1.1 km, the mean station elevation, and no earthquakes are located above this depth.)

5.3.2. Mt. Spurr

Mt. Spurr, an andesitic stratovolcano located in Cook Inlet, Alaska, erupted three times in the summer of 1992 through the active vent Crater Peak (*Alaska Volcano Observatory*, 1993; *Eichelberger et al.*, 1995). Seismicity beneath the active vent Crater Peak dips to the SSW, suggesting that the magmatic conduit dips to the SSW (*Power et al.*, 1995). Long-period earthquakes occurred at depths of 20-40 km, suggesting fluid pressurization; volcanic tremor occurred in the upper 1 km, presumably in the shallow conduit (*McNutt et al.*, 1995), and a post-eruption earthquake swarm at 5-10 km depths may indicate the top part of the magma chamber (*Power et al.*, 1995).

We use the data set of VT earthquakes recorded by the Alaska Volcano Observatory (AVO) with M_{comp}=0.1. The period 1991-1995 includes all three 1992 eruptions of Mt. Spurr. Overall, these data contain 643 events within about 2 km of Crater Peak and spanning a magnitude range from 0.1 to 2.2. Events analyzed ranged from 0 to 12 km in depth. For the Spurr data set, zero km depth refers to the floor of Crater Peak at 1.98 km above sea level. Note that the reference datum is nearly the same for the two volcanoes, which facilitates comparison.

5.4 Method

We estimate the *b*-value by both the maximum likelihood and the weighted least squares methods, because different methods have different advantages and by comparing two methods we can

ensure that our results are independent of the method used (*Bender*, 1983). The *b*-value is estimated in sliding depth windows containing 100 or 200 earthquakes which are then displayed in vertical cross-sections. To visualize the *b*-value distribution as a function of space in more detail, we project all earthquakes using several vertical cross-sections. We sample the seismicity in overlapping horizontal cylindrical volumes containing 100 earthquakes each, using a grid with a 0.1 km grid spacing. The *b*-value is then estimated for each volume and we assign each *b*-value a color. Red colors indicate high *b*-values, blue low *b*-values. For further details on the techniques to estimate *b* see *Wiemer and Benoit* (1996), who applied the same techniques to study the variation of the FMD with depth in subduction zones.

We estimate the probability that two FMD's are different using a test proposed by *Utsu* (1992). If b_1 and b_2 are the slopes of two FMD's, and n_1 and n_2 are the total number of events larger than M_{comp}, then the probability P that the two distributions are different can be written as:

$$P = \exp\left(\frac{-dA}{2} - 2\right)$$

where (2)

$$dA = -2n\ln(n) + 2n_1\ln\left(\frac{n_2 b_1}{b_2} + n_1\right) + 2n_2\ln\left(\frac{n_1 b_2}{b_1} + n_2\right)$$

and $n=n_1 + n_2$. In order to establish a significant difference we will require that two *b*-values are different at the 99% confidence limit (P=0.01). During our analysis we interactively confirmed anomalies by viewing the individual FMD's. We contour the confidence limits in the following way: At each grid-point we compare the *b*-value at this grid-point with the *b*-value for the remaining data-set, using equations 2.

5.5 Results

5.5.3. Mt. St. Helens

The *b*-values as a function of depth, using the sliding window analysis for the Mt. St. Helens catalog, are presented in Figure 5.1. The center panel shows a north-south cross-section view of the seismicity. The cross-section is 3 km long, 1 km wide and cuts through the center of the resur-

gent dome. Each of the FMD's used to calculate b contained 200 earthquakes. The b-value as a function of depth (left panel, Figure 5.1) is low ($b \leq 0.8$)from 0.7-2.6 km and from 3.6-6.4 km, and high ($b \geq 1.2$) from 2.6 -3.6 km and from 6.4-8.0 km. Below this depth the density of earthquakes is too low to permit analysis. The right panel of Figure 5.1 shows a histogram of the depth distribution of the events, each bin extending 0.5 km in depth. The anomalous region of b=1.2 at 2.6-3.6 km depth correlates with an increased number of earthquakes at this depth. At greater depth no noticeable increase in the number of events is visible, despite the increased b-value. We verified our results by comparing FMD's at different depths. The b-value for earthquakes at a depths of 1-2.3 km is 0.68 ± 0.05, and at the depth range 2.8-3.6 km it is $b=1.36 \pm 0.04$. Both curves contain about 200 earthquakes and follow closely the linear Gutenberg-Richter distribution. The two distributions are significantly different at the 99% confidence limit using Utsu's test (equation 2). We are therefore confident that the distribution of b-values with depth as shown in Figure 5.1 is real and is not caused by computational artifacts.

Using a 0.1 km grid, we map out the spatial distributions in a two dimensional view (Figure 5.2). The most outstanding anomalies are a volume of high b-values (red colors) at a depth of 2.7-3.8 km and a volume of high b-values at a depth of about 6.7-9.0 km. The 99% contour lines (Figure 5.2) indicate that in both regions of increased b the anomalies are significantly different from the rest of the data at the 99% confidence limit. The result of the cross-section analysis (Figure 5.2) confirms the b-value as a function of depth curve (Figure 5.1). We also calculated an east-west trending cross-section view, and mapped views at different depth ranges. All of these views show approximately the same distribution of b. The FMD is shown for four cylindrical volumes in the right panel of Figure 5.2. The volumes (labeled A-D in Figure 5.2) were chosen to represent regions of extremely low and high b-value. From these plots it is clear that the distributions are distinctly different. Regions with a high b-value do not contain any events with magnitudes $M>1.5$, whereas the low b-value regions contain events up to magnitude 2.8.

5.5.4. Mt. Spurr

At Mt. Spurr the analysis of the FMD as a function of depth using the moving window technique for the Crater Peak seismicity (Figure 5.3, left panel) shows a low b-value at the surface, which remains at a minimum of b=0.75 to about 2 km depth. A sharp peak between depths of 2.9-3.9 km (b=1.2) can be observed, after which b drops again. The number of events in each depth bin

(Figure 5.3, right panel) resembles closely the distribution of *b* with depth.

The spatial distribution of the FMD at Crater Peak was investigated using a SW-NE trending cross-section with a length of 3 km and a width of 2 km (Figure 5.3, center panel). One outstanding region of anomalously high *b*-values can be observed at a depth of about 2.3-4.5 km depth underneath Crater Peak (Figure 5.4). The *b*-value in this region (b=1.8) is almost twice the normal *b*. The contour lines of the significance of *b* establish that the increase in *b* at this depth is significant at the 99% confidence limit. We show four FMD's that represent the extreme values (A-D in Figure 5.3). The anomalous region at 3.2 km depth (B) cannot sustain earthquakes larger than M=0.6, whereas at other depths events with a magnitude of up to 2.2 occur. A final increase of *b* at 10.8 km depth can be observed in both the cross-section (Figure 5.4) and the *b*-value versus depth curve (Figure 5.3). Unlike Mount St. Helens, Mt. Spurr has deeper seismicity extending to depths of >40 km. We obtained a *b*-value of 1.67 for the 80 events between 20 and 40 km depth. Petrologic evidence (*Nye et al.*, 1995) suggests the existence of a deep (>20 km) magma chamber at Spurr, in agreement with the high *b*-value.

5.6 Discussion and Conclusions

Our results show that the *b*-value varies significantly as a function of depth (Figures 5.1 and 5.3) and location (Figures 5.2 and 5.4) under the two volcanoes investigated. The detailed analysis of the FMD is capable of resolving two distinctly different areas: (1) volumes containing average to low *b*-values (b=0.8±0.2), and (2) volumes containing high *b*-value anomalies (b=1.5±0.3). Regions of high *b*-value in our analysis are characterized by an increased number of events (Figures 5.1 and 5.3), and typically have a largest event one magnitude unit smaller than the surrounding regions. Based on these observations we believe it is incorrect to assume that volcanic areas can simply be characterized by an overall higher *b*-value. Instead we propose that anomalously high *b*-value pockets exist in a crust otherwise described by an average or normal *b*-value. Our results emphasize the heterogeneous properties of the crust that can be studied, given high quality earthquake catalogs.

For Mt. St. Helens, we find that the two volumes with anomalously high *b*-value coincide in location with a suggested shallow magma reservoir or zone of vesiculation and a deeper magma reservoir. The shallow anomaly at depths of 2.6-3.6 km below the dome of Mt. St. Helens coin-

cides with a zone believed altered by vesiculation and disruption of the ascending magma (*Pallister et al.*, 1992; *Chadwick et al.* 1988). The high *b*-value anomaly at >7 km below the dome of Mt. St. Helens coincides with the proposed main magma reservoir as derived from the earthquake-free zone that is surrounded by hypocenters, the orientation of the stress field at this depth (*Moran*, 1994; *Scandone and Malone*, 1985; *Barker and Malone*, 1991), and tomographic results (*Lees*, 1992). *Lees* (1992) observed a 7 percent change in velocity at depths of 7-10 km. Using data from the period 1988-1993, *Moran* (1994) showed changes in the orientation of the stress field of up to 80 degrees that may indicate the re-pressurization of a magma chamber at these depths.

The plumbing system of Mt. Spurr/Crater Peak is poorly understood. The cross-section and depth slice analysis of the FMD (Figures 5.3 and 5.4) show an area of increased *b*-value at a depth of 2.3-4.5 km underneath Crater Peak. Based on the similarity between the Mt. St. Helens and Mt. Spurr analyses (Figures 5.2 and 5.4), we suggest that vesiculation permanently altered the rock surrounding the conduit at a depth of about 3-4 km underneath the active vent Crater Peak. The increased *b*-values at depths below 10.8 km (Figures 5.3 and 5.4) could be caused by a deeper magma reservoir. However, due to the low seismicity rate at this depth, we do not have sufficient data to indicate the existence of such a reservoir. The small number of deep (20-40 km) earthquakes has a high *b*-value, and they correspond to the likely depth of a magma chamber based on petrologic evidence (*Nye et al.*, 1995). Here material heterogeneity and thermal stresses are the most likely causes of the high *b*-values because the pressures are too great for vesiculation by water exsolution to be important (vesiculation of CO_2 is a possibility).

The cause for the anomalously high *b*-value regions under both volcanoes cannot be resolved with certainty at this point. It is possible that all three proposed mechanisms (temperature, stress, and heterogeneity) are jointly responsible for the increase in the *b*-value. The depth of the observed shallow anomalies at both volcanoes coincides approximately with petrological evidence for the vesiculation of ascending magma containing 4 wt.% H_2O at about 4 km (*Eichelberger*, 1995). We speculate that this marks the depth at which the vesiculation of the ascending magma causes the surrounding rock to fracture, thus increasing the crack density or heterogeneity of the material and consequently shifting the fractal distribution of events towards higher *b*-values (*Main*, 1987). Alternatively, interaction of magma with groundwater may increase pore pressure at this depth and lower the effective stress. Open cracks are known to exist at depths of 3 km or so, and

these would facilitate groundwater movement.

To explain the increase in *b* observed in the vicinity of the main magma chamber at greater depth, we suggest that an increase in the material heterogeneity in the rock surrounding the magma chamber is caused by thermal cracking and high stresses. This interpretation is consistent with the observed decrease in P and S-wave velocity at this depth (*Lees*, 1992).

The maximum magnitude of events observed in the high *b*-value zones translates into a maximum rupture length of about 70 m for Mt. St. Helens (M_{max}=1.5) and about 20 m for Crater Peak (M_{max}=0.6). These values are determined using the scaling relation by *Kanamori and Anderson* (1975). Using the fractal dimension $D=2b$ (*Turcotte*, 1992), the high *b*-value regions (b=1.2-1.8) could be described as volumes where the fractal dimension is close to 3. This is consistent with a three dimensional volume with cracks oriented in all directions. Alternative explanations would be a thermal anomaly associated with shallow magma storage, or a local perturbation of the stress field. Either an anomalous temperature or stress regime, however, would represent temporary effects that would diminish as the environmental conditions returned to normal. If our interpretation is indeed correct, the permanent trace left behind by vesiculation and thermal cracking should be detectable by our method at many andesitic volcanoes.

The resolution of our method depends on the seismicity rate and the magnitude of completeness M_{comp}. As a measure of the resolution we use the radius of the horizontal cylindrical volumes containing 100 earthquakes. For Mt. St. Helens, the average radius was 0.8 km. We believe that the two-dimensional cross-section analysis is the superior approach to the one-dimensional depth-slice analysis if the number of earthquakes is sufficient to permit a detailed study. Seismicity at both volcanoes investigated in this paper is restricted to narrow vertically oriented zones, and the analysis of *b* in depth slices (Figures 5.1 and 5.3) and cross-sections (Figures 5.2 and 5.4) reveals similar results. In a regional setting where the seismicity is more spread out, cross-sections can identify anomalous volumes more accurately. Preliminary results by M. Wyss (pers. commun., 1996) indicate that high *b*-value anomalies can be identified underneath several volcanoes in Japan, and that the locations of these anomalies correlate with the inferred locations of magma chambers in the crust.

To address the question of whether the described anomalies could be caused by artifacts in the magnitude reporting or the hypocenter accuracy, we investigated the dependency of a number of quality descriptors (such as RMS, vertical and horizontal error, number of stations reporting) on depth and magnitude. For both catalogs, we found no evidence that could explain the high b-values or the lack of large events in the anomalous regions.

We believe that the high resolution techniques presented in this paper can give important clues about the plumbing system of a volcano. The FMD is one of the few methods available for collecting information about the material properties at depth, short of drilling. The comparison between Mt. St. Helens and Mt. Spurr reveals that both volcanoes show a sharp increase in the b-value at a depth of 2.5-3.5 km below the crater floor, or 1-2 km below sea level. In both regions an increase in b can be observed at greater depths. These similarities suggest a possible generic behavior of andesitic volcanoes. Future work will focus on more case studies and an attempt to analyze the FMD as a function of time and space simultaneously. To overcome the ambiguity in the interpretation of b-value changes, it is necessary to quantitatively compare the b-value changes with other geophysical and petrological observations such as attenuation, P and S-wave velocities, stress tensor orientations, resistivity, and earthquake swarm locations at a variety of volcanoes.

5.7 Acknowledgments

The authors would like to thank M. Wyss, C. Nye, H. Fletcher, and J. Benoit for helpful comments and suggestions. Additional thanks to the University of Washington for making available the earthquake catalog. This work has been partially supported through a dissertation fellowship of the University of Alaska Fairbanks (SW). A portion of this work was supported by the U.S. Geological Survey as part of the volcano Hazards and Geothermal Studies Program, and by additional funds from the State of Alaska through the Alaska Volcano Observatory.

5.8 References

Alaska Volcano Observatory, Mt. Spurr 1992 Eruption, *EOS, Transactions AGU, 74*, No. 19. 217-222, 1993.

Barker, S., and S. Malone, Magmatic system geometry at Mount St. Helens modeled from the stress field associated with posteruptive earthquakes, *J. Geophys. Res., 96*, 11883-11894, 1991.

Bender, B., Maximum likelihood estimation of b-values for magnitude grouped data. *Bull. Seism. Soc. Am.*, 73, 831-851, 1983.

Chadwick, W.W. Jr. , R.J. Archuleta, and D.A. Swanson, The mechanics of ground deformation precursory to dome-building extrusions at Mount St. Helens, 1981-1982, *J. Geophys. Res., 93*, B5, 4351-4366, 1988.

Eichelberger, J.C., Silicic volcanism: Ascent of viscous magmas from crustal reservoirs, *Annu. Rev. Earth Planet. Sci., 23*, 41-63, 1995.

Eichelberger, J.C., T.E.C. Keith, T.P. Miller, and C.J. Nye, Mount Spurr/Crater Peak eruptions of 1992: Chronology and summary, in: T.E.C. Keith ed., The 1992 eruptions of Crater Peak vent, Mount Spurr volcano, Alaska, *U.S. Geological Survey Bulletin 2139*, 1995.

Gutenberg, B., and C.F. Richter, Frequency of earthquakes in California, *Bull. Seism. Soc. Am.*, 34, 185-188, 1944.

Ishimoto, M., and K. Iida, Observations sur les seisms enregistre par le microseismograph construit dernierment, *Bull. Earthquake Res. Inst. Tokyo Univ., 17*, 443-478, 1939.

Iyer, H.M., Geophysical evidence for the locations, shapes and sizes, and internal structures of magma chambers beneath regions of Quaternary volcanism, *Phil. Trans. R. Soc. Lond., A 310*, 473-510, 1984.

Kanamori, H., and D.L. Anderson, Theoretical basis of some empirical relations in seismology, *Bull. Seism. Soc. Am, 65*, 1073-1095, 1975.

Lees, J.M., The magma system at Mount St., Helens: non-linear high-resolution P-wave tomography, *J. Volcanol. Geotherm. Res., 53*, 103-116, 1992.

Main, I.G., A characteristic earthquake model of the seismicity preceding the eruption of Mount St. Helens on 18 May 1980, *Phys. Earth Planet. Int., 49*, p.283-293. 1987.

McNutt, S.R., G. Tygat, and J.A. Power, Preliminary analysis of volcanic tremor associated with the 1992 eruptions of Crater Peak, Mount Spurr, Alaska, in: T.E.C. Keith ed., The 1992 eruptions of Crater Peak vent, Mount Spurr volcano, Alaska, *U.S. Geol. Survey Bulletin 2139*, 161-177,

1995.

Mogi, K., Magnitude-Frequency relation for elastic shocks accompanying fractures of various materials and some related problems in earthquakes, *Bull. Earthq. Res. Inst., 40*, p. 831-853. 1962.

Moran, S., Seismicity at Mount St. Helens, 1987-1992: Evidence for repressurizing of an active magmatic system, *J. Geophys. Res., 99*, 4341-4354, 1994

Nye, C.J., M.L. Harbin, T.P. Miller, S.E. Swanson, and C.A. Neal, Whole-rock major- and trace-element chemistry of 1992 ejecta from Crater Peak, Mount Spurr Volcano, Alaska, in: T.E.C. Keith ed., The 1992 eruptions of Crater Peak vent, Mount Spurr volcano, Alaska, *U.S. Geol. Survey Bulletin 2139*, 119-128, 1995

Pallister, J., R. Hoblitt, D. Crandell, and D. Mullinneaux, Mount St. Helens a decade after the 1980 eruptions: magmatic models, chemical cycles and a revised hazard assessment, *Bull. Volcanol., 54*, 126-146, 1992.

Power, J.A, A.D. Jolly, R.A. Page, and S.R. McNutt, Seismicity and forecasting of the 1992 eruptions of Crater Peak vent, Mount Spurr volcano, Alaska: An overview, in: T.E.C. Keith ed., The 1992 eruptions of Crater Peak vent, Mount Spurr volcano, Alaska, *U.S. Geological Survey Bulletin 2139*, 149-159, 1995.

Scandone, R., and S.D. Malone, Magma supply, magma discharge and readjustment of the feeding system at Mount St. Helens during 1980, *J. Volcanol. Geotherm., Res., 23*, 239-362, 1985.

Scholz, C.H., The frequency-magnitude relation of microfracturing in rock and its relation to earthquakes, *Bull. Seism. Soc. Am., 58*, 399-415, 1968.

Turcotte, D.L., *Fractals and chaos in geology and geophysics*, Cambridge Univ. Press, 221 pages, 1992.

Urbancic, T.I., C.I. Trifu, J.M. Long, and R.P. Young, Space-time correlations of b-values with stress release, *PAGEOPH, 139*, 449-462, 1992.

Utsu, T., On seismicity, in: Report of Cooperative Research of the Institute of Statistical Mathematics 34, Mathematical Seismology VII, *Annals of the Institute of Statistical Mathematics, Tokyo*, 139-157, 1992.

Warren, N.W., and G.V. Latham. An Experimental Study of Thermally Induced Microfracturing and its Relation to Volcanic Seismicity. *J. Geophys Res., 75*, 4455-4464. 1970.

Wiemer, S., and J. Benoit, Mapping the b-value Anomaly at 100 km Depth in the Alaska and New Zealand Subduction Zones, *Geophys. Res. Lett*, 23, 1557-1560, 1996.

Wiemer, S., and M. Wyss, Mapping the frequency-magnitude distribution in asperities: an improved technique to calculate recurrence times?, submitted to J. Geophys. Res., 1996.

Wyss, M., Towards a physical understanding of the earthquake frequency distribution. *Geophys. J. Royal Astr. Soc.*, *31*, 341-359, 1973.

Zobin, V.M., Variations of volcanic earthquake source parameters before volcanic eruptions, *J. Volcanol. Geotherm. Res.*, *6*, 279-293, 1979.

5.9 Figures

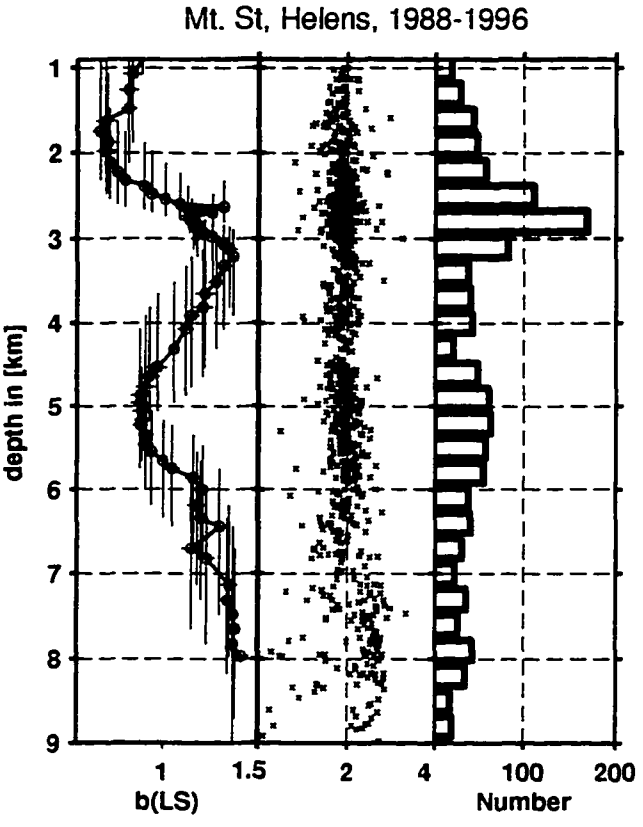

Figure 5.1. *b*-value as a function of depth for Mt. St. Helens (left panel) Center panel: Cross-section view, north-south trending, of the seismicity at Mt. St. Helens from 1988-1996. The cross-section is 0.5 km wide and cuts through the center of Mt. St. Helens. Right panel: Histogram of the depth of the seismicity at Mt. St. Helens. Each bin is 0.5 km in depth.

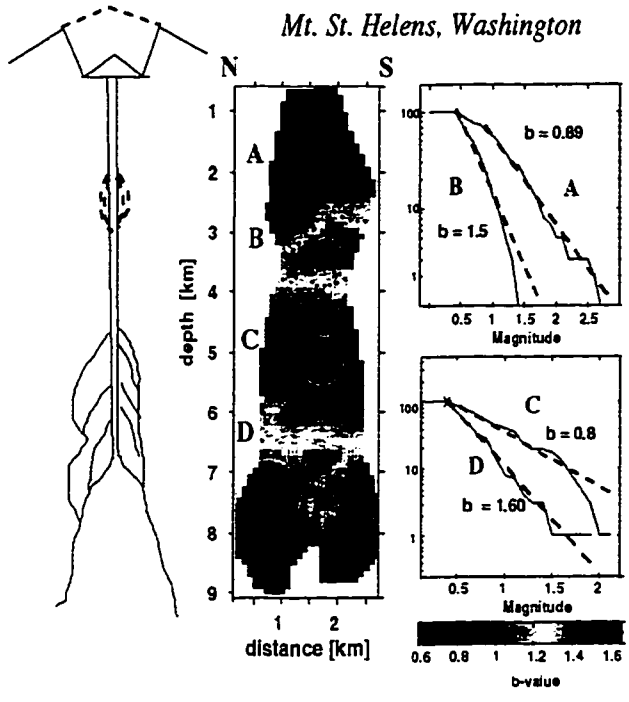

Figure 5.2. Distribution of *b*-values in a vertical N-S cross-section through Mt. St. Helens. The contour lines are the 95% and 99% significance level based on equation 2, and the black line drawing represents a schematic view of the Mt. St. Helens systems by *Pallister et al.* (1992). For four volumes (labeled A-D), the FMD is plotted on the right.

Figure 3

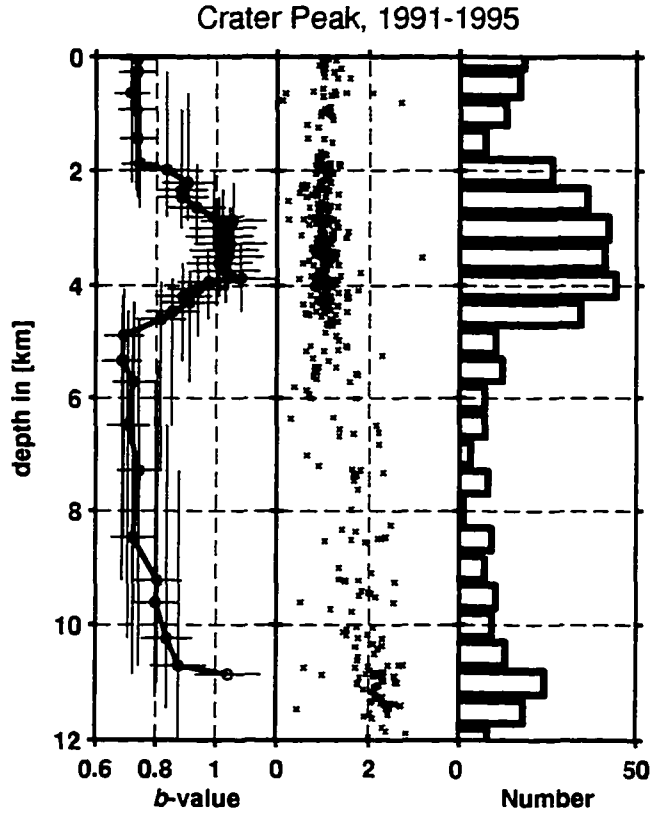

Figure 5.3. *b*-value as a function of depth for Crater Peak, Alaska (left panel). Center panel: Cross-section view, NW-SE trending, of the seismicity at Mt. Spurr from 1991-1995. The cross-section is 2 km wide and cuts through the center of Crater Peak. Right panel: Histogram of the depth of the seismicity at Crater Peak. Each bin is 0.5 km in depth.

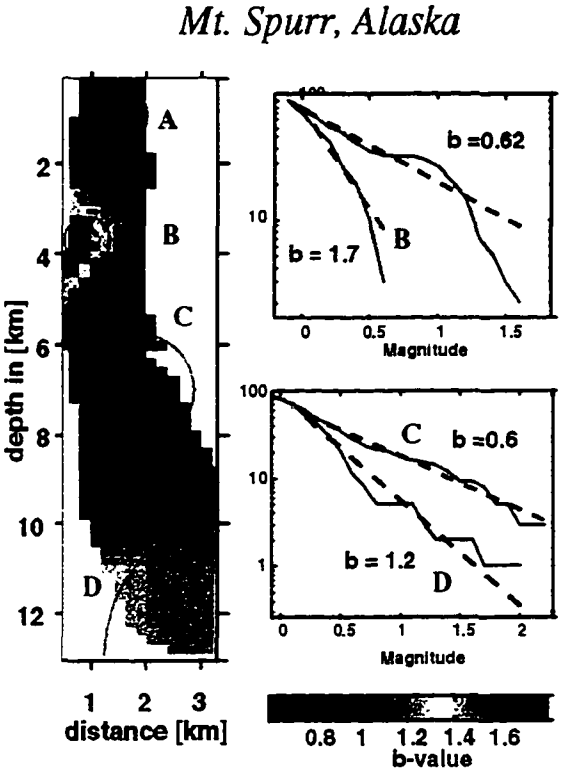

Figure 5.4. Distribution of *b*-values in a vertical NW-SE cross-section through Crater Peak. The contour lines are the 95% and 99% significance level based on equation 2. For four volumes (labeled A-D), the FMD is plotted on the right.

Chapter 6. Mapping the Frequency-Magnitude Distribution in Asperities: an Improved Technique to Calculate Recurrence Times?[1]

6.1 Abstract

We add further evidence to the observations that the *b*-value of the frequency-magnitude relationship of earthquakes is inversely proportional to stress by showing that it decreases with depth in the Parkfield segment of the San Andreas and along the Calaveras fault. *b*-values above and below 5 km depth are approximately 1.2 and 0.8, respectively, based on samples of at least 800 earthquakes each, in both of these areas. The significance of this difference exceeds the 99% confidence limit. At Parkfield the lack of co-seismic displacement in the top crustal layers during the 1966 main shock, and the accumulation of 30 cm surface dislocation during the following two years, clearly showed that the top several km of the fault are a poorly coupled, low stress environment. This evidence, combined with observations in the laboratory, in underground mines, of the dependence of *b* on pore pressure, and comparisons of *b* in different tectonic environments strongly suggests that the fractal distribution of earthquakes is perturbed by increased stress in favor of more large events.

We find support for the hypothesis that asperities, the locations of high stress concentration, may be defined by mapping anomalously low *b*-values. Along the San Andreas fault near Parkfield the asperity under Middle Mountain, with its b=0.46, can clearly be distinguished from all other parts of the fault surface. Likewise, along the Calaveras fault the northern asperity of the Morgan Hill 1984 (M6.2) rupture can be identified by its low *b* of 0.5 as a high stress patch along the fault. The southern asperity of the Morgan Hill rupture is located in an aseismic region for which *b*-value estimates are not possible.

We propose that probabilistic recurrence times, *Tr*, based on the seismicity parameters *a* and *b* of the frequency-magnitude distribution, should be calculated from their values within asperities only, instead of from the values of the entire rupture area of the maximum expected earthquake. It

1. Stefan Wiemer and Max Wyss, submitted to Journal of Geophysical Reserach, May 1996.

is widely acknowledged that major asperities control the time of rupture. These strong patches on faults are capable of accumulating larger stresses than the rest of the fault zone, which slips along passively when an asperity breaks. Therefore, no information on *Tr* is contained in the passive fault segments, only in the asperities. At Parkfield, the probabilistic estimates of *Tr* derived from the data in the whole rupture and in the asperity only are 70 and 23 years, respectively, compared to the historically observed repeat time of 22 years. At Morgan Hill, *Tr* derived from the seismicity parameters in the whole rupture and in the asperity only are 130 and 78 years, respectively, compared to the observed repeat time of 72 years. We conclude that for moderate main shocks with one major asperities the asperity method to estimate *Tr* may furnishe more accurate results than the conventional method that uses data from the entire rupture. We propose that this method should also be tested for large to great earthquakes, because the same could be true for these events based on a reasonable model of the nature of asperities.

6.2 Introduction

The Earth's crust is heterogeneous at large and small scales. Asperities govern most important aspects of earthquake ruptures and have dimensions ranging from less than a kilometer to tens of kilometers. Significant advances in our understanding of the mechanics of ruptures, of the local hazard distribution, and of recurrence times could be gained if we could map asperities and define their seismicity characteristics. Based on detailed mapping of the frequency-magnitude distribution in the Parkfield and Morgan Hill rupture zones, we demonstrate in this paper that *b*-values are significantly lower in asperities than in the rest of the fault zone. This perturbation of the fractal distribution in favor of larger events can be interpreted as indicative of higher than average stress, a property thought to be typical for asperities.

Two widely accepted concepts in seismological research are the asperity model and the frequency-magnitude distribution. In this paper, both of these models are used to develop a new model to more accurately estimate recurrence times for moderate to large earthquakes. Asperities are defined as strong patches on a fault that are locked during the decades of stress-buildup in a fault system, and they release most of the energy during the eventual earthquake (e.g. *Miyamura et al.* 1965; *Wyss and Brune*, 1967; *Lay and Kanamori*, 1981). The surrounding areas are weakly coupled and passively drag along during the earthquake. The effective stress normal to the fault surface in asperities is believed to be relatively higher than in the surrounding rock. Many studies have been performed to map the location of these asperities and to study their characteristics (e.g. *Ruff and Kanamori*, 1982; *Aki*, 1984; *Christensen and Beck*, 1995). For some

fault systems seismologists believe they have a fairly detailed knowledge of the behavior and extent of the asperities. The Parkfield region is one example where several lines of evidence shed light on the location, as well as the behavior of the asperity (e.g. *Lindh and Boore*, 1981; *Nadeau et al.*, 1994; *Malin et al.*, 1994). An extensive review of the Parkfield prediction experiment was presented by *Roeloffs and Langbein* (1994).

The frequency-magnitude distribution (*Ishimoto and Iida*, 1939; *Gutenberg and Richter*, 1944) describes the power-law relation between the frequency of occurrence and magnitude of earthquakes:

$$log_{10}N = a - bM, \qquad \text{(EQ 6.1)}$$

where N is the cumulative number of earthquakes having magnitudes larger than M, and a and b are constants. Various methods have been suggested to measure b and its confidence limits (e.g., *Utsu*, 1965, 1992; *Aki*, 1965; *Bender*, 1983; *Shi and Bolt*, 1983).

It is common practice to calculate the recurrence time, Tr, based on a and b . The assumptions made are:

(1) The fault segment (crustal volume) that will produce the maximum size earthquake, M_{max}, can be identified.

(2) Over the period Tr the Gutenberg-Richter relationship will be fulfilled with $N_{(Mmax)}=1$.

(3) The seismicity rate (a per unit time) and the distribution with magnitude (b) remain constant with time.

(4) a and b are constant throughout the source volume in question.

This last assumption is made implicitly, but most investigators are not aware of it. In this paper we focus on this problem and investigate the consequences if the assumption of constant a and b as a function of space is strongly violated.

The Gutenberg-Richter relationship to estimate Tr from a and b clearly does not work for some regions and faults. For example, the recurrence time of the San Andreas fault's segment that ruptured in the 1857 great earthquake is estimated as 132 years (*Sieh*, 1984; *Sieh et al.*, 1989) based on paleoseismic evidence. Therefore it should produce approximately 700 M3.5 earthquakes per year according to assumptions (1),

(2) and (3). Instead, only a handful such earthquakes have been observed over the last 50 years on that fault segment. Even along more active segments of strike-slip faults, *Tr* based on the Gutenberg-Richter model is overestimated in about 80% of the cases when compared with paleoseismic evidence (*Wesnousky*, 1994; *Stirling et al.*, 1996). For this reason these authors concluded that the characteristic earthquake model (*Schwarz and Coppersmith*, 1984; Kagan, 1993) results in a better fit to the data for most faults. In this paper we went a step further and questioned the implicit assumption (4). We hypothesize that the estimate of *Tr* for the largest earthquake in a fault segment may be improved by using the *a* -and *b*-values of its major asperity, rather than the values for the whole rupture area.

Figure 6.1 shows a schematic illustration of the frequency-magnitude distributions in cumulative form for the three models. The gray line shows the distribution assumed for the standard calculation of *Tr:* a slope of $b=1$ and an intercept at $N_{Mmax}=1$ (*Gutenberg and Richter*, 1944). The dashed line shows the distribution observed for most strike-slip faults, using the whole rupture area (*Wesnousky*, 1994; *Stirling et al.*, 1996), with a slope of about $b=1$, and intercepting at $N_M{}^a=1$, where M^a is the Magnitude of the largest aftershock. The solid line shows the distribution within asperities, with a low value of about $b=0.5$ and an intercept at $N_{Mmax}=1$. This is the distribution we propose should be used to calculate *Tr* .

There are three reasons for which we think that *b*-value studies are of high interest again: (1) In the catalogs for the last 10 to 20 years we can now define *b* more accurately (many smaller magnitude events are listed) and in greater detail as a function of space (greater accuracy of hypocenters and more events per unit volume). (2) With a new computer tool that allows mapping of the *b*-value in a dense grid as a function of space, we are able to delineate variations in *b* as a function of depth and along fault zones. (3) The realization that the frequency-magnitude distribution represents a self-organized critical system (e.g. *Bak and Tang*, 1989; *Turcotte*, 1992) opened the door for new insights into the physical mechanisms for perturbations of this system.

Two physical parameters that perturb the standard *b*-slope of 1 are stress and heterogeneity. The *b*-value has been shown to be inversely proportional to stress in the laboratory (*Scholz*, 1968) and in mines (*Urbancic et al.*, 1992). The inverse dependence on stress was also demonstrated for earthquakes in Denver, where the pore pressure was known to vary (*Wyss*, 1973). This means that the mean magnitude, <M>, of earthquakes produced in a volume depends on the stress level necessary to rupture the faults present, because <M> is inversely proportional to *b* (*Aki*, 1965; *Utsu*, 1965; *Hamilton*, 1967). Additional evidence

supporting this observation comes from the low b-values observed in thrusting environments, compared to higher b in normal faulting environments (*Frohlich and Davis*, 1993). Since the constant overburden equals the least and greatest principal stresses in the two cases, respectively, it is most likely that the difference in b is due to a difference in ambient stress level.

The b-value was also found to be proportional to the degree of heterogeneity in rock samples in laboratory tests (*Mogi*, 1962). Using a cellular automata, *Steacy et al.* (1996) also found that b increased with increasing range of heterogeneity. In addition these authors showed that the b-value decreased with increasing fractal dimension. We believe their interpretation of this observation was incorrect and offer the following alternative. In their experiment presented in their Figure 6.5a (low fractal dimension D=1.6) the largest events occurred but seldom, and b=1.44 was relatively high. The reason for these two observations is that none (or very few) of the elements in the coherent high strength patches broke throughout their experiment, until all contiguous elements in one of the major asperities broke together in one of the largest events. This means that almost all of the events recorded throughout their experiment occurred in the low-strength elements, which once again confirms that low stress levels lead to high b-values. In their other experiment, using a large fractal dimension (D=2.6, their Figure 6.5b), the elements of diverse strength were well mixed (no major asperities preferentially impeded rupture in high strength elements), and thus the resulting population of events ruptured a mixture of high and low stress elements, leading to a moderate (relatively low) b-value. We believe that our explanation brings the experiment into agreement with other known means of perturbation of the b-value, whereas the interpretation by *Steacy et al.* (1996) was in part at odds with these facts.

The experiments described by *Urbancic et al.* (1992) and *Steacy et al.* (1996) are examples of the reason why we advocate that detailed mapping of the b-value as a function of space along fault zones is informative. We believe that fault zones, and the crust, are heterogeneous in strength, and that one must therefore evaluate the fractal distribution by b-value, mapping it on a fine scale to resolve the differences that exist. Mixing of fault patches with different properties, as is done in the estimates of Tr, may lead to overestimates of Tr, and to misinterpretation of the material properties. Recently, a number of high resolution studies of the frequency-magnitude distribution showed that highly heterogeneous distributions of b-values with significant variations over short distances are abundant in seismogenic regions. Detailed maps of the frequency-magnitude distribution in two subduction zones showed significant variations of b at scales of 10 km (*Wiemer and Benoit*, 1996). These authors identified a region of anomalously high b-value at a

depth of 90-100 km on the upper surface of the Wadati-Benioff Zone, directly underlying the volcanic arc. At this depth, slab dehydration may increase pore pressure, thus lowering the effective stress and increasing the *b*-value. Increased pore pressure would also lower the solidus in the overlying asthenosphere, giving rise to the volcanism that occurs directly above this zone. Similar results have been found by *Wyss et al.* (1996a) using data from Japan. Mapping *b*-values at a scale of less than 1 km grid spacing, *Wiemer and McNutt* (1996) found high *b*-values in the vicinity of active magma chambers at Mount St. Helens (Washington) and Crater Peak (Alaska). *Wyss et al.* (1996b) found the same for the Off-Izu vocanic area in Japan. Our technique of mapping *b*-values thus may offer a tool to locate seismically active magma chambers.

By mapping the distribution of *b*- and *a*-values along a fault system (using cross-sections) the *b*-value can be shown to vary significantly. Areas with the lowest *b*-values coincide with the location of the asperities. We argue that high stress is the most likely cause for the low *b*-value in asperities, and that the frequency-magnitude distribution may be used as a stress-barometer that can identify the location of patches on the fault under high stress. If high resolution imaging of the frequency-magnitude distribution can potentially identify asperities it may contribute to identifying possible nucleation points of future earthquakes. In some cases termination of ruptures may correlate with fault segments of high *b*-values, i.e. low stress segments. Thus, it may be possible that *b*-value "tomography" may contribute to defining rupture areas of future earthquakes.

If rupture volumes show strong contrasts of *b*-values in asperities compared to the rest of the volume, the question arises: Which *b*-value should be used for estimating Tr? We propose that for many cases the *b*-values of the asperities lead to more accurate estimates of *Tr* than the *b*-value of the total rupture area (Figure 6.1).

6.3 Data

In this paper we focus on two fault segments in California: The Parkfield segment of the San Andreas fault and the Morgan Hill segment of the Calaveras fault (Figure 6.2). Both of these areas are favorable targets for a high resolution study of the frequency magnitude distribution for a number of reasons: (1) The seismicity rate is high. (2) The tectonic environment is relatively simple, in that the faults are approximately vertical planes. (3) Seismic monitoring is excellent. The hypocenter accuracy is believed to be better than 1 km, and the catalogs are complete for the most part down to magnitude 1.0. Also, continuity of recording

with time exists over the past 15-20 years. (4) Both segments experienced similar size main shocks. The 1966 M=6.0 Parkfield and the 1984 M=6.2 Morgan Hill event allowed the location of asperities along these fault segments to be identified.

The data were obtained from the Northern California Earthquake Data Center. For the San Andreas fault, earthquakes from the period January 1971- January 1996 with a magnitude ≥ 1.0, and within a 4 km wide zone centered on the fault were selected; a total of 6467 events (Figure 6.2). For the Morgan Hill section of the Calaveras fault, a 4 km wide zone centered on the fault was selected. The data were divided into two sub-sets before and after the 1984 M=6.2 Morgan Hill main shock: (1) the period 1971 - 1984, containing a total of 1711 events with M ≥ 1.3, and (2) the period 1986 -1996, containing a total of 3480 events with M ≥ 1.0.

Before we begin *b*-value studies we investigate the possibility that magnitude stretches (inadvertent changes of the magnitude scale used) may exist in a catalog. We also determine the magnitude of complete reporting, Mc, as a function of time and location before estimating *b*-values, by using the cumulative as well as the non-cumulative frequency-magnitude distribution. Problems of heterogeneous reporting in catalogs are abundant (e.g. *Habermann*, 1982; 1986, 1987; *Wyss*, 1991; *Zúñiga and Wyss*, 1995). In the Parkfield data-set a magnitude stretch was introduced in 1986. We decided to not correct for this change of scale, but to study two subsets in time, before and after 1986.5, in order to estimate the impact of this artificial change in the magnitude reporting.

6.4 Method

We estimate *b*-values in two ways, because different methods have different advantages. We use both the maximum likelihood method and a weighted least squares fit (*Utsu*, 1965; *Aki*, 1965; *Hamilton*, 1967; *Page*, 1968; *Bender*, 1983; *Shi and Bolt*, 1983). By comparing the results obtained using the two methods, we can ensure that our results are independent of the technique used to estimate *b*. Before claiming any significant differences between *b*-values in sub-volumes we inspect the magnitude frequency plots visually to make sure that the data are defining the *b*-value well, and that the computed fit is acceptable based on common sense inspection.

A moving spatial window technique is used to analyze the *b*-value as a function of depth. A window with a constant number of earthquakes (200) is applied, rather than using constant depth intervals in order to avoid fluctuations in the calculated *b*-values due to changes in the number of events. The window is

moved to increasing depth by increments of 10% of the window length (20 earthquakes). The same technique has been used by *Wiemer and Benoit* (1996) to study the variation of the frequency-magnitude distribution with depth in subduction zones.

An estimate of the error, δb, of the *b*-value can be obtained using the equation first derived by *Aki* (1965), or the improved formulation by *Shi and Bolt* (1982)

$$\delta b = 2.3 b^2 \sqrt{\frac{\sum_i (M_i - \langle M \rangle)}{n(n-1)}} \qquad \text{(EQ 6.2)}$$

were <M> is the mean magnitude, and n the sample size. We also estimate the error in *b* and *a* as a function of sample size based on a Monte Carlo type technique that uses the actual data. A random sample of *N* events is drawn from the pool of all magnitudes in the catalog, and the *b*- and *a*-values are estimated for this sample. This process is repeated 300 times. We can thus find the range of *b*-value as a function of sample size *N* (Figure 6.3). Our results agree with a similar study by *Bender* (1983) based on synthetic data-sets. The confidence limits for the Parkfield region for *N=100* are about δb = +/- 0.15 and δa = +/- 0.16, for *N = 250* we find δb = +/- 0.08, and δa = +/- 0.11. The maximum likelihood method results in a more constant mean and a more symmetric distribution of the *b*-values around the mean than the weighted least squares approach. We found that using our technique, lower-quality data-sets such as the early recording period (1971-1980) for the Calaveras fault, show larger confidence limits of *a* and *b*.

The probability that two frequency-magnitude distributions come from the same population is estimated using a test proposed by *Utsu* (1992). If b_1 and b_2 are the slopes of two frequency magnitude distributions, and n_1 and n_2 are the total numbers of events larger M_{comp}, then the probability *P* that the two distributions come from the same population can be written as:

$$P = \exp\left(\frac{-dA}{2} - 2\right) \qquad \text{(EQ 6.3)}$$

where $$dA = -2n\ln(n) + 2n_1 \ln\left(\frac{n_2 b_1}{b_2} + n_1\right) + 2n_2 \ln\left(\frac{n_1 b_2}{b_1} + n_2\right)$$

and $n = n_1 + n_2$. A value of $P = 0.05$ indicates that we can reject the hypothesis that the two *b*-values are equal at the 95% confidence limit. In order to establish a significant difference we will require that two *b*-

values are different at the 99% confidence limit ($P = 0.01$).

To visualize the b-value distribution as a function of space in detail, the earthquakes are projected onto vertical cross-sections perpendicular to and along the strike of the fault. The seismicity is sampled in overlapping cylindrical volumes of constant radius R (for example 3 km), with centers positioned at the nodes of a grid with a 1 km spacing. The b-value is then estimated for each volume and each node is assigned a color proportional to b. Red indicates low b-values, blue high b-values (e.g. Figure 6.7), and the images obtained are smoothed using a spline interpolation. During the analysis, anomalies are interactively confirmed by inspecting the magnitude-frequency distributions and the fit to the distribution. In previous studies of b-values, we have sampled a constant number of events around each grid-node rather than a constant radius, to avoid fluctuations in the estimation of b due to varying sample size (e.g. *Wiemer and Benoit*, 1996).

We judge the activity of a volume by the parameter a in equation 1. Using a constant number of earthquakes results in an a that is a function of b and the information about the activity resides in the radius of each volume sampled. This approach cannot be used here because we need a explicitly to estimate Tr. For volumes of constant radius containing fewer than 50 earthquakes no b-value value is estimated. The software used is part of a larger software package to investigate seismicity rate changes that we developed recently. This software package, ZMAP, is available via anonymous ftp (*Wiemer and Zúñiga*, 1994).

The recurrence time for an earthquake with magnitude equal or greater than M can be calculated from the b and a-value obtained at each grid-node as:

$$T_r = \frac{\Delta T}{10^{(a - bM)}} \qquad \text{(EQ 6.4)}$$

where ΔT is the recording period covered by the seismicity catalog. The error in Tr can be estimated from the confidence limits of a and b (Figure 6.3). An equivalent way of presenting the recurrence times would be as the Poisson probability of an earthquake occurring per year, the inverse of Tr.

The radius of a b-value anomaly that may be an asperity has to be defined for estimating Tr. This is done in the following way. We determine Tr for the events within a cylinder, centered at the previously mapped anomaly, and let the radius increase by increments of 0.2 km, generating Tr estimates as a function of ra-

dius. For small radii *Tr* will be large, regardless of b, because *a* is small (equation (4)). As long as the radius is increased within the asperity, i.e. within a volume of constant *b*, *Tr* decreases because *a* increases. Once the radius extends beyond the limits of the asperity, disproportionate numbers of small earthquakes are added to the sample and *b* decreases. At this point the estimate for *Tr* begins to increase. Consequently, we define the extent of the asperity by the radius for which the estimate for *Tr* becomes a minimum.

6.5 Results - Parkfield

A systematic decrease of the *b*-values as a function of depth is obvious in Figure 6.4a. *b*-values are estimated from the frequency-magnitude distribution using a moving window, starting with the 200 shallowest earthquakes with a magnitude M ≥1.8. The window is successively moved deeper by 25 earthquakes, thus ensuring that the total number of events in each sample remains constant. For the shallow part of the Parkfield segment of the San Andreas fault a *b*-value of around 1.2 is observed (Figure 6.4a). A peak value of *b=1.28* exists at a depth of 4 km, below which *b* systematically decreases with depth. The minimum *b*-value is reached at a depth of 11 km (*b= 0.76*). The results from both methods estimating *b* (maximum likelihood and weighted least squares) are almost identical. Also shown in Figure 6.4a is the histogram of the number of events with depth. The maximum number of events occurs at a depth of about 5.5 km. No correlation between the rate of activity and the *b*-value is detected. To confirm the significance of the variation of *b* with depth, the same moving window technique is applied to a randomized catalog. We used the same data set but randomly assigned a depth, drawn from the pool of depths, to each event. This results, as expected, in a constant distribution of *b* with depth with a mean of *b*= 0.85 +/- 0.08.

The frequency-magnitude distributions for events in the depth range 0-5 km yield a *b*-value of 1.26 (Figure 6.4), whereas the subsets covering the depths below 7 km show a *b*-value of 0.88. The difference in *b* is significant at the 99.9% confidence limit using Utsu's test (equation 3) and clearly does not result from computational inadequacies. The *b*-value calculations are based on earthquakes ranging in magnitude from 1.8 to larger than 4, spanning about 2.5 magnitude units, and they are defined by more than 800 events in each data set. The same results are obtained when using a different Mc.

A vertical cross-section of the distribution of *b*-values along the strike of the fault (Figures 6.5 and 6.6) and across the fault (Figure 6.7) allows a detailed analysis of the distribution of *b*-values. The cross-section along the strike of the fault is 4 km wide and about 100 km long (Figure 6.5a). We use a grid with a spacing of 1 km, and calculate the *a* and *b*-value for the earthquakes within a 3 km radius from each node.

The color representation of the distribution of *b*-values along the strike of the San Andreas fault (Figure 6.5b) shows low *b*-values in red and high *b*-values in blue. The *b*-values vary significantly and systematically with location. Higher *b*-values can generally be found close to the surface and vice versa, confirming the one-dimensional *b*-value analysis as a function of depth (Figure 6.4a). The lowest *b*-value of the entire 100 km long segment is located underneath the Middle Mountain segment of the fault. Two moderate earthquakes (M=4.6, 14/11/93; M=4.7, 20/12/94) believed to have occurred within the Parkfield asperity are marked by stars in Figure 6.5. Their locations coincide with the patch of anomalously low *b*-values at a depth of about 10 km. *b*-values are generally lower to the south-east of the Middle Mountain segment, and higher to the north-west. To confirm the results of the cross-section analysis, the frequency-magnitude distribution at a number of nodes were inspected. Two frequency-magnitude distributions, representing extreme populations are shown in Figure 6.8. Although the two volumes are within 10 km of each other, the two populations yield *b*-values almost a factor of three different (0.46 versus 1.3). In the shallow volume, no earthquake with a magnitude larger than 2.0 is recorded, whereas the deep volume contains events up to M=4.7.

Recurrence times for a magnitude M = 6 earthquake based on the *b*- and *a*-values at each node are calculated using equation 4 and a sampling radius of 3 km. A cross-section of the distribution of recurrence times along the strike of the San Andreas fault is shown in Figure 6.5d. The recurrence times range from 22 years to over 10000 years. The image in Figure 6.5 focuses on the shortest recurrence time values from 20 to 250 years. The most outstanding anomaly, with the shortest recurrence time of 22 years, coincides with the location of the low *b*-value anomaly and thus the location of the Parkfield asperity. The second lowest recurrence time (Tr = 60 years) is recorded approximately 18 km to the south-east at the same depth of around 10 km.

The *a*-values (and therefore the recurrence time Tr) at each node depend on the number of earthquakes sampled. Therefore, we must hold the sampling radius constant for estimating *Tr*. Of all the sampling radii we could choose to produce Figure 6.5d, we are most interested in *R(Tr=min)*, the one that leads to the shortest *Tr* in the asperity, based on the reasoning we outlined in the methods section. The recurrence time reaches a minimum of 22 years for the asperity volume at a sampling radius of 3 km (Figure 6.9). Thus, we find that the Parkfield asperity has a diameter of 6 km, and we computed Figure 6.5d using $R_{(Tr=min)}$=3 km for all nodes. Nodes for which this radius selected fewer then 50 events were not colored.

In Figure 6.7a the *b*-values are presented in a vertical cross-section perpendicular to the strike of the San Andreas fault and through the Middle Mountain segment (defined in Figure 6.2a). The cross-section is 20 km wide. A significant variation of b with depth can be observed, ranging from b = 1.1 at shallow depth to b = 0.5 at a depth of 10 km. A rapid transition from high to low *b*-values occurs at a depth of about 5 km. The locations of the two M > 4.5 earthquakes coincide with the region of the lowest *b*-value. The recurrence time map (Figure 6.7 center) highlights this region even more. The minimum recurrence time of Tr = 50 years at a depth of 10 km coincides with the Parkfield asperity.

The data for Parkfield were studied separately for the pre- and post-1986.5 periods (Figure 6.6) because a magnitude stretch took place at that time. In this way we avoid mixing of scales and we will have an estimate of changes as a function of time and of changes possibly introduced by new reporting standards.

6.6 Results - Morgan Hill

The epicenters of the earthquakes selected for the study of the Calaveras fault are shown in Figure 6.2b. Using the data for the period 1986-1996, we find that the *b*-values decrease systematically as a function of depth (Figure 6.4b). In each sample 200 events with M≥1.0 are used and the selection window is stepped by 20 events. At shallow depths we find b>1. At about 4 km depth a strong decrease can be noticed, and a minimum at *b*=0.6 is reached below 9 km depth. The data above and below 5 km depth define *b*-values of 1.13 and 0.75, respectively (Figure 6.4). The numbers of data points are approximately 1000 and 2000 for the two sets compared, and the difference is judged significant above the 99.9% confidence level using *Utsu's* (1992) test. The pattern of decreasing *b*-values as a function of depth is very similar at Parkfield and Morgan Hill (Figure 6.4).

The *b*-values along the Calaveras fault are mapped in cross sections 3 km wide, using a 1 km grid spacing, for two periods (Figures 6.10 and 6.11); before the Morgan Hill main shock (1971-1984.3) and after its aftershock sequence had decayed (1986-1996). The aftershock sequence is excluded because we wish to establish the patterns of *a* and *b* from data during intervals without a main shock, to estimate *Tr* in the customary fashion. In addition, separate analyses of data from two periods allows a preliminary assessment of the stability of *b*-value patterns as a function of time. We see that the *b*-value patterns are similar in the two periods, showing a close association of a patch of lowest *b*-values with the aftershock area of 1984

(Figures 6.10 and 6.11). The frequency-magnitude distribution within the Morgan Hill asperity (b=0.53) is compared to that in the shallow fault segment above it (b=1.4) in Figure 6.8. The strong difference between the two earthquake samples is evident and judged significant above the 99% confidence level using *Utsu's* (1992) test.

Figures 6.10 and 6.11 show the recurrence time calculated from the a- and b-values at each node for a magnitude 6 earthquake. The minimum recurrence time, using a sampling radius of 3 km, is 78 years and coincides in location with the rupture area of the 1984 Morgan Hill earthquake. The sampling radius that yields the shortest recurrence time, R_{min}=3 km, is estimated by calculating Tr as a function of R for the Morgan Hill asperity.

6.7 Discussion and Conclusions

6.7.1. Decrease of b-values with Depth and Inverse Dependence on Stress

The decrease of b-values as a function of depth is established by high quality data sets for both the Parkfield segment of the San Andreas and the Calaveras fault (Figure 6.4). More than 800 events over two to three orders of magnitude define b for data sets above and below 5 km depth as about 1.2 and 0.8, respectively (Figure 6.4). This observation agrees with the result by *Mori and Abercrombie* (1996), who found this pattern along several faults in California, and with that of *Wyss* (1973), who showed it for the aftershocks of the Borrego Mt. earthquake of 1968. The observation of decreasing b with depth at Parkfield is particularly important because it confirms the interpretation by *Wyss* (1973) that it is due to increasing stress with depth. The evidence that the top two to four kilometers at Parkfield are weakly coupled and support much lower stresses than the fault below 5 km depth is the following. (1) Most of the fault segment studied shows fault creep along the surface (e.g. *Schulz et al.*, 1982). (2) The 1966 main shock was not associated with any appreciable co-seismic surface faulting. Instead the co-seismic dislocation propagated as creep from a depth below 4 km to the surface, generating a clear fault break and accumulating about 30 cm of right lateral slip during the two years following the main shock (*Smith et al.*, 1968; *Scholz et al.*, 1968). Thus, the contrast of high and low b-values above and below 5 km at Parkfield is possibly the strongest piece of evidence establishing the inverse dependence of b on stress for crustal earthquakes.

A second, qualitative indication of poor coupling, hence low stress, at shallow depth comes from the near absence of hypocenters in the top two kilometers in both test cases (Figure 6.4). At Parkfield the low level of activity extends to four kilometers depth, the depth above which no co-seismic displacement occurred

in 1966 (*Scholz et al.*, 1968).

We believe that the stress dependence of *b* can now be accepted as an established fact based on the following observations. (1) *b* decreases with increased ambient stress in the laboratory (*Scholz*, 1966). (2) *b* was proportional to pore pressure in the Denver earthquakes (*Wyss*, 1973). (3) *b* correlates inversely with high stress volumes in mine excavations (*Urbancic et al.*, 1992). (4) *b* is lower in tectonic regimes of thrust faulting than in normal faulting (*Frohlich and Davis*, 1993). (5) *b* correlates inversely with coupling, hence with stress, as a function of depth at Parkfield (Figures 6.4 and 6.7).

6.7.2. Mapping Asperities in Fault Zones by b-values

We propose that asperities along fault zones may be mapped by anomalously low *b*-values, based on the inverse correlation of *b* with stress. We test this hypothesis for two segments of the San Andreas fault where locations of asperities are known. At Parkfield the volume with about 5 km radius around the rupture initiation point of the fore- and main shock of 1966 below Middle Mountain, has been designated as alert box (*Roeloffs and Langbein*, 1994) because it is considered to be the key asperity along this fault segment for a number of reasons (e.g. *Lindh et al.*, 1981; *Nadeau et al.*, 1994; *Malin et al.*, 1994). In this case the asperity does not coincide with the area of greatest slip during the earthquake (*Segall and Harris*, 1987), which was located further south in 1966. The Parkfield asperity seems to act as a locked segment that casts a creep-shadow along the fault south of it. The segment north of it shows high creep rates, south of it the creep rate decreases to zero at approximately the southern rupture end of 1966. Once the Middle Mountain asperity breaks, the rupture segment south of it slips along, catching up with the integral slip released by creep during the interseimic interval north of the asperity. Therefore, we accept the definition of the Parkfield asperity as the alert box under Middle Mountain, and not as the location of largest slip.

In the *b*-value cross-sections of the Parkfield segment of the San Andreas fault (Figures 6.5 and 6.7) the location of the Parkfield asperity is marked by the large crosses, the hypocenters of the largest two earthquakes (M>4.5) that have occurred since 1975. The lowest *b*-value of 0.43 coincides exactly with the Parkfield asperity and contrasts strongly with *b* in the rest of the rupture area (Figure 6.5b). This supports our hypothesis that asperities may be mapped as locations of high stress concentrations by exceptionally low *b*-values. The frequency-magnitude relations for the asperity volume (B) and the volume above it (A) are shown in Figure 6.8. The difference in b of 0.43 and 1.5 is outstandingly clear.

The second major patch of anomalously low *b*-values in the San Andreas cross-section studied is located

near the southern end of the 1966 Parkfield rupture. The entire rupture area is characterized by lower *b*-values than surrounding areas. The very southern segment of the fault that we were able to image shows again increased *b*-values, which may indicate the existence of a barrier in 1966, terminating the rupture of the main shock at that time. The aseismic, locked part of the San Andreas south of approximately 35.3°N latitude cannot be studied by our method because not enough earthquakes occur.

From the cross-section view of the San Andreas fault at Parkfield and north of it, it becomes clear that areas of the fault separated by only a few kilometers can show a distinctly different frequency-magnitude distribution (Figure 6.5b), an indication of the heterogeneity of the crust. Each frequency-magnitude distribution follows the Gutenberg-Richter power law closely. The variability in *b* is a factor 3 greater than expected when assuming a random distribution of magnitudes (Figure 6.3). The spatial correlation of the location of the Parkfield asperity and the area of lowest *b*-value suggests that this variability in the frequency-magnitude distribution is not purely random, but systematic and the result of a physical process. The entire segment investigated covers an area of 100 km x 15 km, or 1500 km^2. The Parkfield asperity covers an area of approximately 3 km in radius, 28 km^2, or 2% of the total area. This value estimates the chance correlation of the asperity and the lowest *b*-value patch.

We investigated the *b*-value distribution separately for the periods 1971-1986.5 and 1986.5-1996 and found that the distribution along the strike of the fault remains basically the same (Figures 6.5 and 6.6). Thus the low *b*-value observed in the Parkfield asperity is not a result of the recent moderate main shocks or due to stretches in the magnitude scale, but a feature that can be identified throughout the recording history of the catalog.

For the Morgan Hill segment of the Calaveras fault there is no special asperity defined, so we accept the two areas of largest slip during the 1984 main shock as the asperities. The northern one of these, extends from the hypocenter to about 5 km to the south, the other was centered about 15 km south of the hypocenter (*Hartzell and Heaton*, 1986; *Bakun et al.*, 1986; *Mikumo and Miyatake*, 1995). The second of these two asperities is located in an aseismic patch of the fault (Figures 6.10 and 6.11), for which we have no information because we cannot measure the *b*-value. The northern asperity, however, correlates exactly with the strongest anomaly of low *b*-values on the segment of the Calaveras fault investigated (Figures 6.10 and 6.11). The contrast between the frequency-magnitude relationship of the northern Morgan Hill asperity (b=0.5) and that of the shallow seismicity above it (b= 1.2, Figure 6.8) is as striking and significant

as the contrast at Parkfield.

To test whether a systematic error in the hypocenter quality or magnitude estimation could be the reason for the observed changes of *b* with depth and along the strike, we investigated a number of quality descriptors that are given in the catalog. We found for the Parkfield data set a mean vertical error in the hypocenters of 0.86 km, a mean horizontal error of 0.43 km, a mean RMS travel time residual of 0.076, and an average of 19 P- and S-phases reported for each event. We investigated the dependency of these quality descriptors on depth and magnitude and found no correlation that possibly could explain the observed decrease of *b* with depth. We also selected a sub-set of 2657 events that contained only high quality hypocenters (vertical error <= 1.5 km, horizontal error < 1 km, RMS < 0.15, and number of P- and S-phases > 10). Using this high quality data-set we found the same dependency of *b* with depth, and identified the same anomalies in cross-section view. The minimum recurrence times calculated were the same as those estimated from the entire data set.

We conclude that out of two asperities investigated (Parkfield and northern Morgan Hill) both support the hypothesis that asperities in fault zones may be mapped by anomalously low *b*-values if they are seismically active enough to allow *b*-value estimates.

6.7.3. Stability of b-value Anomalies as a Function of Time

In a preliminary investigation of the stability of *b*-value anomalies as a function of time we examined the *b*-value cross sections of the Parkfield and the Calaveras fault segments in two periods. The overall impression is that in both cases there is little change as a function of time. In Parkfield the two cross sections looked very similar, in spite of the magnitude stretch in 1986.5. One exception may be a volume near the southern end that shows lower *b*-values in the second period. In the Calaveras case one can notice some differences. The period after the 1984 main shock shows somewhat lower *b*-values, especially north of the main shock, where three historic M5 class earthquakes have been located (1943, 1955, 1988; *Oppenheimer et al.*, 1990). It may be that the effective stress along this segment of the fault was increased by the 1984 Morgan Hill main shock, either through decrease of pore pressure or redistribution of shear stress. We conclude that temporal changes of *b*-value patterns may exist, but are weaker than spatial differences. We postpone detailed investigations of *b* as a function of time for a future study.

6.7.4. Recurrence Times of Moderate Earthquakes Calculated From Asperities

The concept that asperities control the time of rupture in earthquakes is generally accepted. As a corollary

of this concept we propose that any information on recurrence time must reside in the asperity. The fault area outside the asperity, that slips along relatively passively when the asperity breaks, cannot contain any information on the recurrence time of the main shock that results when the asperity breaks. During the inter-event period the passive part of the rupture area simply waits for the next event to emanate from the asperity. We accept the forestated assumptions (1) through (3) necessary for calculating recurrence time from equation (4) as valid, and we compare the result with the historically observed *Tr* with and without assumption (4). Computing *Tr* from equation (4) using *a* and *b* from the entire rupture segment of the Parkfield and Morgan Hill rupture areas we obtain 72 and 122 years, respectively (Table 1). Using *a* and *b* from the asperities only, we estimate the respective recurrence times as 23 and 78 years. The historically observed *Tr* for Parkfield is 22 years (*Bakun and McEvilly*, 1984), and that for Morgan Hill is 73 years (*Oppenheimer et al.*, 1990).

These comparisons of *Tr* calculated by our method with historically observed recurrence times (Table 1) suggest that our hypothesis is correct: For moderate main shocks of the M6 class the probabilistic recurrence estimate based on equation (4) yields more accurate results if the seismicity parameters from the asperity only are used. If we calculate *Tr* based on the seismicity outside the asperities we obtain large values between several hundred years and 10,000 years (Figures 6.5d, 10 and 6.11).

Table 6.1: Recurrence Time Estimates for Parkfield and Morgan Hill

Method	Parkfiled			Morgan Hill 71-84		
	a (km^2)	b	Tr (years)	a (km^2)	b	Tr (years)
all	3.6	0.71	72	3.9	0.82	122
outside	3.2	0.95	>1000	~4	>1	>1000
asperity	2.5	0.43	23	2.4	0.55	78
historic	---	---	22	---	---	73

The results given in Table 1 for the Morgan Hill case were calculated from the pre-main shock period, assuming that this is a period with seismicity characteristics representative for the inter-event period. The estimate of *Tr* from the post 1985 seismicity parameters in the asperity would be a factor of two shorter

because the seismicity rate (a-value) is still elevated compared to the pre-main shock level. To base the estimate of *Tr* on the post-main shock data would thus not be correct.

6.7.5. Recurrence Times Calculated from Total Rupture Areas

Since our results suggest that the asperities govern the recurrence time of moderate to large earthquakes we believe that *Tr* estimated from entire rupture areas may be overestimated if major asperities are embedded in passive parts of the fault area. *Stirling et al.* (1996) found that along 80% of the strike-slip faults they investigated the standard calculation of *Tr* overestimates the historically observed values substantially. We propose that these errors are due to the mixing of seismicity parameters *a* and *b* from passive and asperity parts of the rupture areas. If our hypothesis is correct the fault segments investigated by these authors contain a mixture of passive and asperity parts, and we propose that by using the seismicity parameters of the asperities instead of the mixed overall averages, more accurate estimates of *Tr* may be obtained.

In general we expect that recurrence times calculated from total fault seismicity parameters cannot be accurate, unless the seismicity parameters are uniform over the fault area. This condition could exist in some cases (e.g. 20% of the faults investigated by *Stirling et al.*, 1996), but it is not likely to be the general case because the crust is heterogeneous and most fault surfaces contain asperities.

6.7.6. Probabilistic Recurrence Estimates for Great Earthquakes

We expect that correct estimates of *Tr* may be possible, based on our method, for the main shocks studied by *Wesnousky* (1994) and *Stirling et al.* (1996) because these events are in the moderate to large magnitude range. However, for most ruptures in the large to great range one may argue that no probabilistic method using equation (4) can furnish reliable estimates of *Tr*, since these ruptures are usually composed of several major asperities. However, it may be that the ratio of asperity surface to entire fault surface in great ruptures is the same as that observed at Parkfield, approximately five. Also, great ruptures are most likely to occur along fault segments with several major asperities in a row that have similar individual recurrence times. If this is so, and if they have once been synchronized by a single large rupture, then they may rupture together repeatedly. Based on this idea, we speculate that *Tr* estimated for several major asperities of one great rupture should all equal approximately the historically observed recurrence time of that rupture. To stipulate that several asperities in a row may have the same *Tr* is not as far fetched as it seems because they all share a common fault surface (plate boundary) and a common strain accumulation

rate. By virtue of all of them being asperities, they may also have similar resistance to faulting, and thus their recurrence times may be similar. Therefore, we propose to test the hypothesis that major asperities in large to great earthquakes may all furnish estimates of *Tr* approximately equal to the historically observed recurrence times. If this should be shown to be correct then we may have a means of estimating how large a segment of a fault (plate boundary) may rupture in a great earthquake by mapping asperities based on their low *b*-values (the method developed in this paper), and calculating their individual *Tr*. Groups of asperities with similar *Tr* could then be considered candidates for simultaneous rupture, if there is evidence that their seismic cycle was synchronized. Asperities with appreciably different *Tr* are less likely to participate in the same overall rupture, so ruptures should terminate between asperities with dissimilar *Tr* , as well as in extended areas of high *b*-values suggesting low ambient stress.

6.7.7. Identifying Potential Locations of Rupture Termination

An earthquake rupture that propagates from asperity to asperity may stop in a low-stress fault patch between asperities. We interpret the *b*-value cross section of the Calaveras fault (Figure 6.10b) as demonstrating this phenomenon. Once the rupture initiated at the hypocenter, it propagated to the south with increasing slip (e.g. *Hartzell and Heaton*, 1986) into the fault patch of lowest *b*-values (red in Figure 6.10b). The rupture did not propagate northward from the hypocenter because the stress on the fault was low in this segment as reflected by normal *b*-values (blue in Figure 6.10b). The rupture continued to the southern asperity of the Morgan Hill main shock (*Hartzell and Heaton*, 1986), located in the fault segment where we cannot map *b* because there are practically no earthquakes. South of this zone the rupture stopped in a fault segment that is colored dark blue (from kilometer mark 40 to 50 approximately in Figure 6.10b), indicating high *b*-values. We suggest that this fault segment has low stresses and therefore the rupture of the 1979 Coyote Lake (M5.9) could not propagate north past this patch to connect to the southern Morgan Hill asperity, and the Morgan Hill rupture, propagating south, terminated in this low stress patch also.

For the Parkfield case we also propose that the low stresses suggested by high *b*-values north of the hypocenter (blue in Figure 6.5b) prevented the rupture from propagating north. The generally popular explanation that the 1966 Parkfield rupture stopped near Highway 46 because the fault south of this point is locked seems reasonable to us, but we cannot test it for want of earthquakes. If we had data in this location we would expect to see anomalously low *b*-values and a recurrence time substantially longer than that of the Parkfield asperity, possibly the 132 years typical for the 1857 break of the Carizo Plains fault segment.

One of the limitations of our method is that completely locked asperities, where no earthquakes occur, cannot be mapped. However, the absence of earthquakes does not necessarily indicate high stresses. Continuous fault creep could occur in these locations reducing the stress so substantially that no earthquakes occur.

If we are able to establish with more certainty that earthquakes rupture mainly in low *b*-value regions and that ruptures preferably stop in regions with a high *b*-value and between asperities with different *Tr*, we may be able to develop a technique to estimate the extent of future rupture areas. For this study we calculated recurrence times for events with M6, the size observed from the historic record because we do not know yet how to independently relate the size of *b*-value anomalies (asperities) to the size of the future main shock. We realize that this paper contains several new ideas, some of which are not tested yet and others for which only few examples lend support so far. Also, the results from mapping in detail the seismicity parameters *a* and *b* along fault zones open new questions. It seems to us that many of these questions may be answered by the type of detailed studies we conducted in this paper, and that the perturbation of the fractal distribution of earthquakes holds a great deal of information important for estimating earthquake hazard and for understanding tectonic processes leading to earthquake ruptures.

6.8 Acknowledgments

The authors would like to thank J. Lahr and H. Fletcher for reviewing the manuscript. Support for this work has partly been provided by the Wadati endowment of the University of Alaska Fairbanks, Geophysical Institute.

6.9 References

Note: preprints for submitted documents of Wyss and Wiemer can be obtained by anonymous ftp from giseis.alaska.edu in the directory /ftp/pub/preprints.

Aki, K., Maximum likelihood estimate of b in the formula log N = a - b M and its confidence limits, Bull. Earthq. Res. Inst., 43, 237-239, 1965.

Aki, K., Asperities, barriers, characteristic earthquakes and strong motion prediction, J. Geophys. Res., 89, 5867-5872, 1984.

Bak, P., and C. Tang, Earthquakes as a self-organized critical phenomenon, J. Geophys. Res., 94, 15635-15637, 1989.

Bakun, W. H., Seismic activity of the southern Calaveras fault in Central California, Bull. Seism. Soc. Am., 70, 1181-1197, 1980.

Bakun, W. H., and T. V. McEvilly, Recurrence models and Parkfield, California, earthquakes, J. Geophys. Res., 89, 3051-3058, 1984.

Bakun, W. H., R. M. Stewart, C. G. Bufe, and S. M. Marks, Implication of seismicity for failure of a section of the San Andreas fault, Bull. Seism. Soc. Am., 70, 185-201, 1980.

Bakun, W. H., M. M. Clark, R. S. Cockerham, W. L. Ellsworth, A. G. Lindh, W. H. Prescott, A. F. Shakal, and P. Spudich, The Morgan Hill, California, earthquake, Science, 225, 288-291, 1984.

Bakun, W. H., G. C. P. King, and R. S. Cockerham, Seismic slip, aseismic slip, and the mechanics of repeating earthquakes on the Calaveras fault, California. In: Earthquake source mechanics., 37, S. Das, C. Scholz, and J. Boatwright eds., AGU Geophys. Mono., Washington. 195-207, 1986.

Bender, B., Maximum likelihood estimation of *b*-values for magnitude grouped data, Bull. Seism. Soc. Am., 73, 831-851, 1983.

Ben-Zion, Y., and J. R. Rice, Earthquake failure sequences along a cellular fault zone in a three-dimensional elastic solid containing asperity and nonasperity regions, J. Geophys. Res., 98, 14109-14131, 1993.

Beroza, G. C., and P. Spudich, Linearized inversion for fault rupture behavior: application to the 1984 Morgan Hill, California, earthquake, J. Geophys. Res., 93, 6275-6296, 1988.

Christensen, D. H., and S. L. Beck, The rupture process and tectonic implications of the great 1964 Prince William Sound earthquake, PAGEOPH, 142, 29-53, 1994.

Eberhardt-Phillips, D., and A. J. Michael, Three-dimensional velocity structure, seismicity, and fault structure in the Parkfield region, Central California, J. Geophys. Res., 98, 15737-15758, 1993.

Frohlich, C., and S. Davis, Teleseismic *b*-Values: Or, Much Ado about 1.0, J. Geophys. Res., 98, 631-644, 1993.

Gutenberg, R., and C. F. Richter, Frequency of earthquakes in California, Bull. Seism. Soc. Am., 34, 185-188, 1944.

Habermann, R. E., Consistency of teleseismic reporting since 1963, Bull. Seism. Soc. Am., 72, 93-112, 1982.

Habermann, R. E., A test of two techniques for recognizing systematic errors in magnitude estimates using data from Parkfield, California, Bull. Seism. Soc. Am., 76, 1660-1667, 1986.

Habermann, R. E., Man-made changes of Seismicity rates, Bull. Seism. Soc. Am., 77, 141-159, 1987.

Habermann, R. E., Seismicity rate variations and systematic changes in magnitudes in teleseismic catalogs, Tectonophysics, 193, 277-289, 1991.

Hamilton, R. M., Mean magnitude of an earthquake sequence, Bull. Seism. Soc. Am., 57, 1115-1116, 1967.

Harris, R., and P. Segall, Detection of a locked zone at depth on the Parkfield, California segment of the San Andreas fault, J. Geophys. Res., 92, 7945-7962, 1987.

Hartzell, S. H., and T. H. Heaton, Rupture history of the 1984 Morgan Hill, California, earthquake from the inversion of strong motion records, Bull. Seism. Soc. Am., 76, 649-674, 1986.

Ishimoto, M., and K. Iida, Observations of earthquakes registered with the microseismograph constructed recently, Bull. Earthq. Res. Inst., 17, 443-478, 1939.

Kagan, Y. Y., Statistics of characteristic earthquakes, Bull. Seism. Soc. Am., 83, 7-24, 1993.

Lay, T., and H. Kanamori, The asperity model of earthquake sources and its implication for triggering and discrimination. In: Earthquake Prediction: An International Review, Maurice Ewing Ser., 4, D. W. Simpson, and P. G. Richards eds., AGU, Washington, DC, 579-592, 1981.

Lay, T., H. Kanamori, and L. Ruff, The asperity model and the nature of large subduction zone earthquakes, Earthquake Prediction Research, 1, 3-72, 1982.

Lindh, A. G., and D. M. Boore, Control of rupture by fault geometry during the 1966 Parkfield earthquake, Bull. Seism. Soc. Am., 71, 95-116, 1981.

Malin, P. E., S. N. Blakeslee, M. G. Alvarez, and A. J. Martin, Microearthquake imaging of the Parkfield asperity, Science, 244, 557-559, 1994.

McEvilly, T. V., W.H. Bakun and K.B. Casaday, The Parkfield, California, earthquakes of 1966, Bull. Seism. Soc. Am., 57, 1221-1244, 1967.

Mikumo.T, and T. Miyatake, Heterogeneous distribution of dynamic stress drop and relative fault strength recovered from the results of waveform inversion: the 1984 Morgan Hill, California, earthquake, Bull. Seism. Soc. Am., 85, 178-193, 1995.

Miyamura, S., S. Omote, R. Teisseyre, and E. Vesanen, Multiple shocks and earthquake series pattern, Bull. Int. Inst. Seism. Earthq. Eng., 2, 71-92, 1964.

Mogi, K., Magnitude-Frequency Relation for Elastic Shocks Accompanying Fractures of Various Materials and some Related Problems in Earthquakes, Bull. Earthq. Res. Inst., 40, 831-853, 1962.

Mori, J., and R. E. Abercrombie, Depth dependence of earthquake frequency-magnitude distributions in California: Implications for the rupture initiation, in preparation, 1996.

Nadeau, R., M. Antolik, P. A. Johnson, W. Foxall, and T. V. McEvilly, Seismological studies at Parkfield III: Microearthquake clusters in the study of fault-zone dynamics, Bull. Seism. Soc. Am., 84, 247-263, 1994.

Oppenheimer, D. H., W. H. Bakun, and A. G. Lindh, Slip partitioning of the Calaveras fault, California, and prospects for future earthquakes, J. Geophys. Res., 95, 8483-8498, 1990.

Page, R., Aftershocks and microaftershocks of the great Alaska earthquake of 1964, Bull. Seism. Soc. Am., 58, 1131-1168, 1968.

Roeloffs, E., and J. Langbein, The earthquake prediction experiment at Parkfield, California, Rev. of Geophys., 32, 315-335, 1994.

Scholz, C. H., The Frequency-Magnitude Relation of Microfracturing in Rock and its Relation to Earthquakes, Bull. Seism. Soc. Am., 58, 399-415, 1968.

Scholz, C. M., M. Wyss, and S. W. Smith, Seismic and aseismic slip on the San Andreas fault, J.

Geophys. Res., 74, 2049-2069, 1969.

Schulz, S. S., G. M. Mavko, R. O. Burford, and W. D. Stuart, Long-term fault creep observations in Central California, J. Geophys. Res., 87, 6977-6982, 1982.

Schwartz, D. P., and K. J. Coppersmith, Fault behaviour and characteristic earthquakes: Examples from the Wasatch and San Andreas fault zones, J. Geophys. Res., 89, 5681-5698, 1984.

Segall, P., and R. Harris, Earthquake deformation cycle on the San Andreas fault near Parkfield, California, J. Geophys. Res., 92, 10511-10525, 1987.

Shi, Y., and B. A. Bolt, The standard error of the Magnitude-frequency b value, Bull. Seism. Soc. Am., 72, 1677-1687, 1982.

Sieh, K. E., Lateral offsets and revised dates of large prehistoric earthquakes at Pallett Creek, Southern California, J. Geophys. Res., 89, 7641-7670, 1984.

Sieh, K. E., M. Stuiver, and D. Brillinger, A more precise chronology of earthquakes produced by the San Andreas fault in Southern California, J. Geophys. Res., 94, 603-623, 1989.

Smith, W. S., and M. Wyss, Displacement on the San Andreas fault subsequent to the 1966 Parkfield earthquake, Bull. Seism. Soc. Am., 58, 1955-1973, 1968.

Steacy, S. J., J. McCloskey, C. J. Bean, and J. Ren, Heterogeneity in a self-organized critical earthquake model, Geophys. Res. Lett, 23, 383-386, 1996.

Stirling, M. W., S. G. Wesnousky, and K. Shimazaki, Fault trace complexity, cumulative slip, and the shape of the magnitude-frequency distribution for strike slip faults: a global survey, Geophys. J. Int, 124, 833-868, 1996.

Turcotte, D. L., Fractals and chaos in geology and geophysics, Cambridge, 1992.

Urbancic, T. I., C. I. Trifu, J. M. Long, and R. P. Toung, Space-time correlations of *b*-values with stress release, PAGEOPH, 139, 449-462, 1992.

Utsu, T., A method for determining the value of b in a formula log n = a - bM showing the magnitude frequency for earthquakes, Geophys. Bull. Hokkaido Univ., 13, 99-103, 1965.

Utsu, T., On seismicity. In: Report of the Joint Research Institute for Statistical Mathematics. 34, Institute for Statistical Mathematics, Tokyo, 139-157, 1992.

Warren, N. W., and G. V. Latham, An Experimental Study of Thermally Induced Microfracturing and its Relation to Volcanic Seismicity, J. Geophys. Res., 75, 4455-4464, 1970.

Wesnousky, S. G., The Gutenberg-Richter or characteristic earthquake distribution, which is it?, Bull. Seism. Soc. Am., 84, 1940-1959, 1994.

Wiemer, S., and J. Benoit, Mapping the *b*-value anomaly at 100 km depth in the Alaska and New Zealand subduction zones, Geophys. Res. Lett., 23, 1557-1560, 1996.

Wiemer, S., and S. McNutt, Mapping the magnitude-frequency distribution in volcanic regions as a tool for detecting magma chambers, Geophys. Res. Letts, 23, submitted, 1996.

Wiemer, S., and R. F. Zúñiga, ZMAP - a software package to analyze seismicity, EOS, Transactions, Fall Meeting, AGU, 75, 456, 1994.

Wyss, M., Towards a physical understanding of the earthquake frequency distribution, Geophys. J.

R. Astr. Soc., 31, 341-359, 1973.

Wyss, M., Reporting history of the central Aleutians Seismograph network and the quiescence preceding the 1986 Andreanof Island earthquake, Bull. Seism. Soc. Am., 81, 1231-1254, 1991.

Wyss, M., and J. N. Brune, The Alaska earthquake of 28 March 1964: A complex multiple rupture, Bull. Seism. Soc. Am., 57, 1017-1023, 1967.

Wyss, M., A. C. Johnston, and F. W. Klein, Multiple asperity model for earthquake prediction, Nature, 289, 231-234, 1981.

Wyss, M., K. Shimazaki, and S. Wiemer, Maping active magma chambers by *b*-values, J. Geophys. Res., 101, in preparation, 1996a.

Wyss, M., S. Wiemer, and S. Tsuboi, Magnitude distribution anomalies in the WBZ beneath Japan, J. Geophys. Res., in preparation, 1996b.

Zúñiga, R., and M. Wyss, Inadvertent changes in magnitude reported in earthquake catalogs: Influence on *b*-value estimates, Bull. Seism. Soc. Am., 85, 1858-1866, 1995.

6.10 Figures

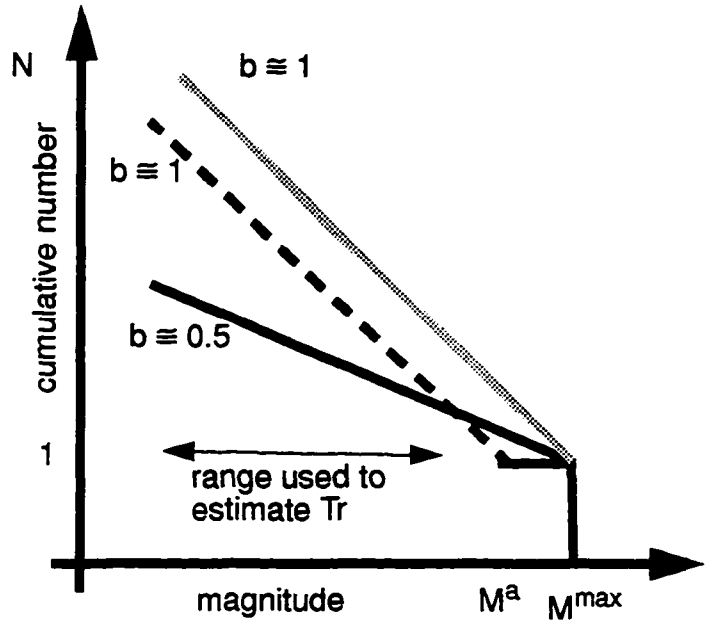

Figure 6.1. Schematic representation of the frequency-magnitude distribution models. To explain the underestimation of the rate of large events Mmax predicted by the Gutenberg-Richter relationship (gray line), the characteristic earthquake model (dashed line) assumes that a power law relationship exists only for events up to a magnitude Ma, the magnitude of the largest aftershock of the characteristic earthquake (Mmax). Based on our observations that asperities have anomalously low *b*-values (b~0.5), we propose that *Tr* of Mmax can be estimated more reliably from the frequency-magnitude relationship in asperities (solid line).

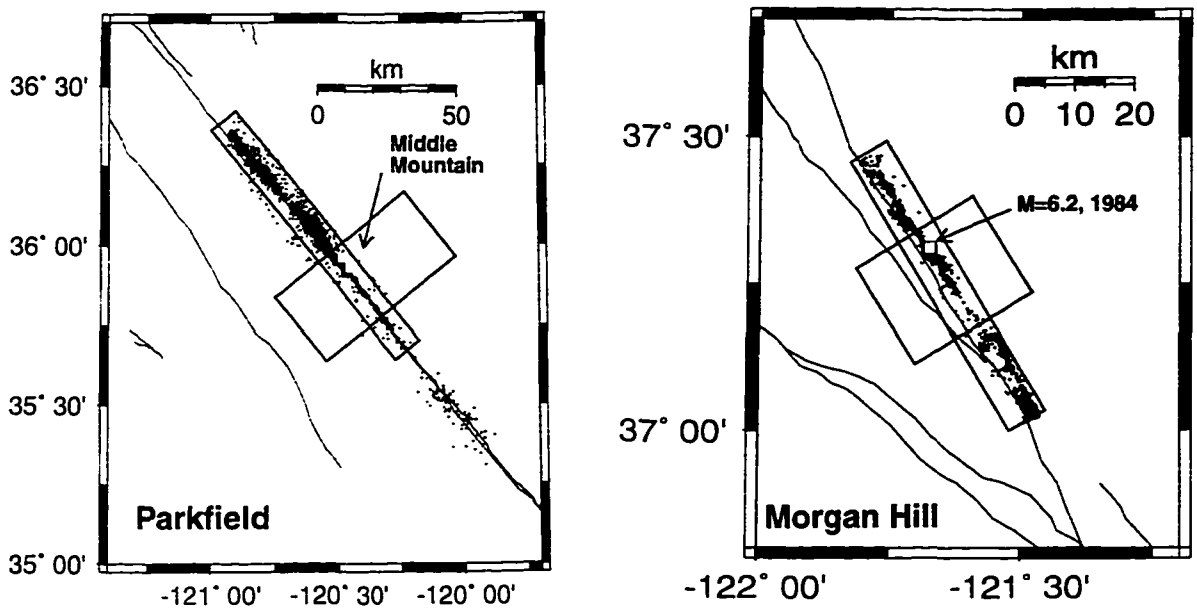

Figure 6.2. Epicenter map of the selected earthquakes along the Parkfield (left) and Morgan Hill (right) fault segments from 1980 to 1996. The location of Middle Mountain is marked. The polygons indicate the cross-sections used in Figures 6.4,6.5, 6.6, 6.10, and 6.11.

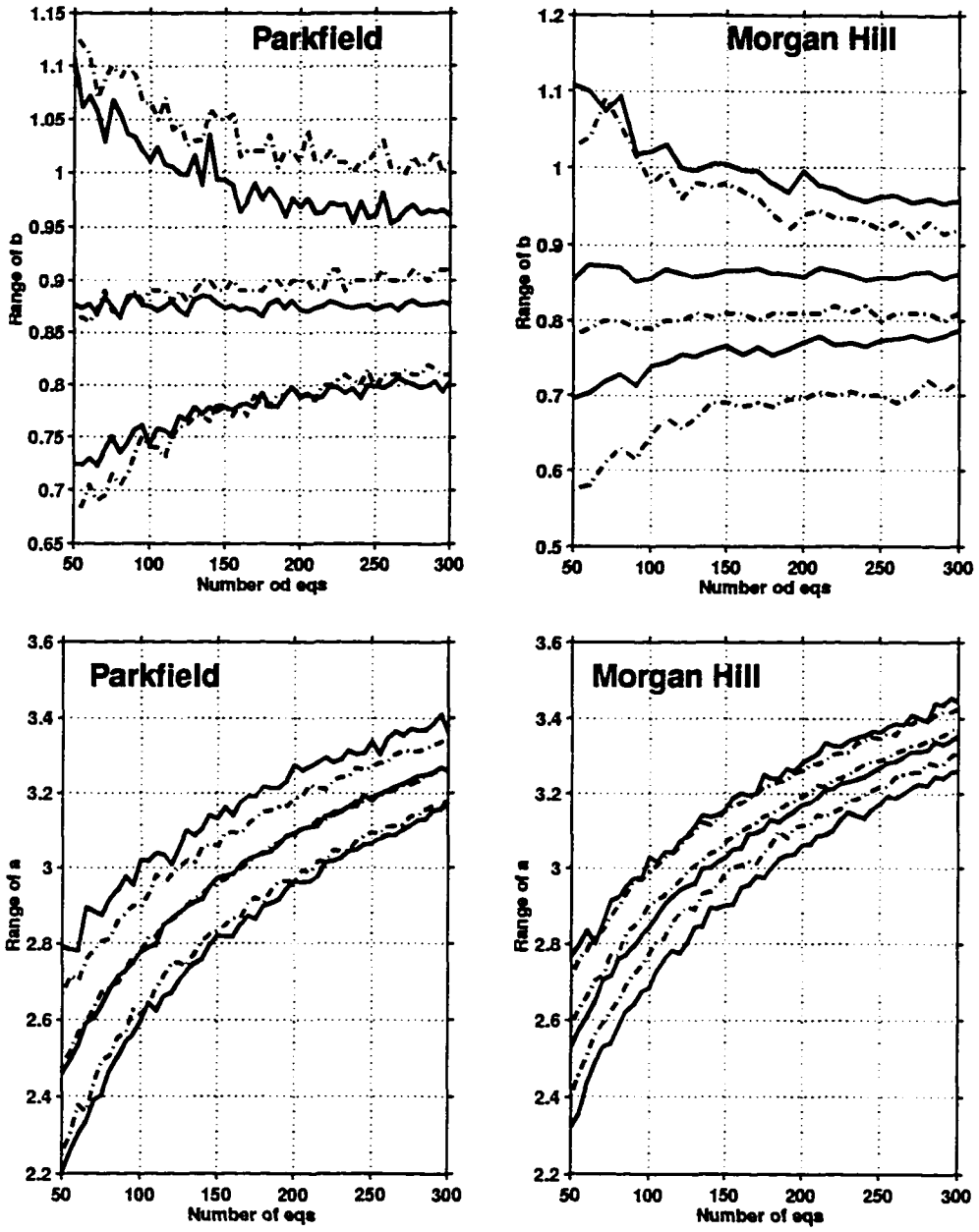

Figure 6.3. Range of *b*-values as a function of sample size N for synthetic catalogs. A sample of N magnitudes was drawn at random from the actual data-sets (left: Parkfield, right: Morgan Hill). By repeating this 300 times for each N a range of the *b*-values can be determined. Plotted are the 1, 50, and 99 percentiles using the maximum likelihood method (solid line) and the weighted least squares method (dotted line).

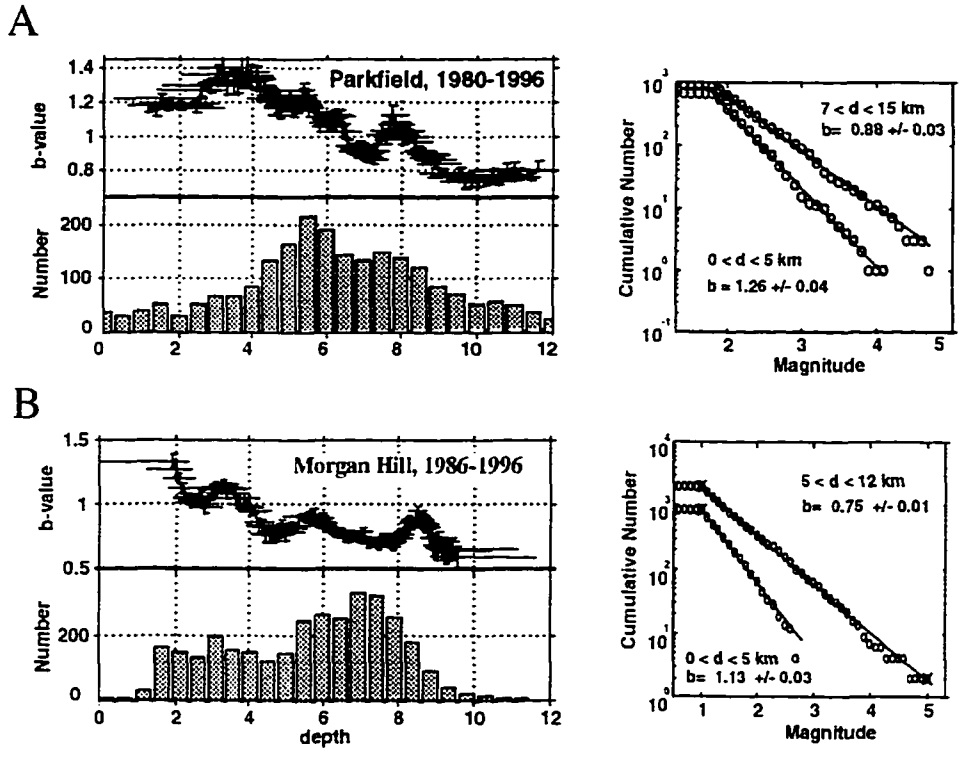

Figure 6.4. *b*-values as a function of depth for the Parkfield segment of the San Andreas fault (left frame, A). Each *b*-value was calculated for a depth slice containing 250 earthquakes. Vertical bars are the errors in b, horizontal bars indicate the depth range sampled. Bottom frame: Histogram of the number of events in 0.5 km depth bins. Right frame: Frequency magnitude distribution for two depth ranges: 0 - 5 km and 7 - 15 km. (b) same as (a) for the Calaveras fault.

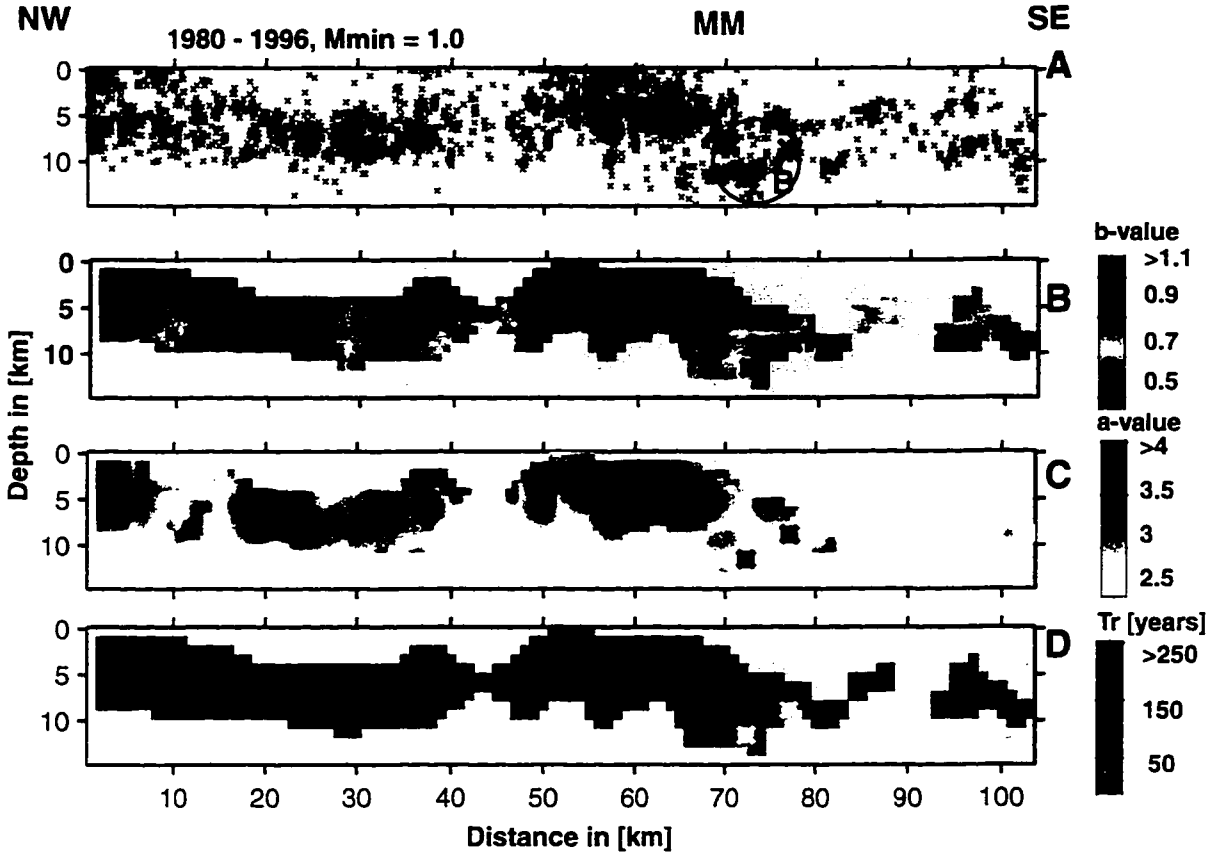

Figure 6.5. Cross-section view along strike of the San Andreas fault containing the Parkfield asperity, using data from the period 1980-1996. (a) Vertical cross-section showing the locations of hypocenters. The two largest earthquakes (M>4,5) that occurred within the Parkfield asperity are marked by 'x'. The two circles define the volumes for which the frequency magnitude distributions are shown in Figure 6.6. (b) Distribution of *b*-values along strike of the fault. Red colors indicate low *b*-values, blue high *b*-values. The color bar encompasses only the range from 0.4-1.0, larger *b*-values are shown in the same color as used for b=1.0. (c) Distribution of *a*-values (d) Recurrence time *Tr* for a M6 earthquake, calculated from the *a* and *b*-values at each node. The color bar encompasses only the range from 20 to 250 years, larger recurrence times are shown in the same color as used for 250 years.

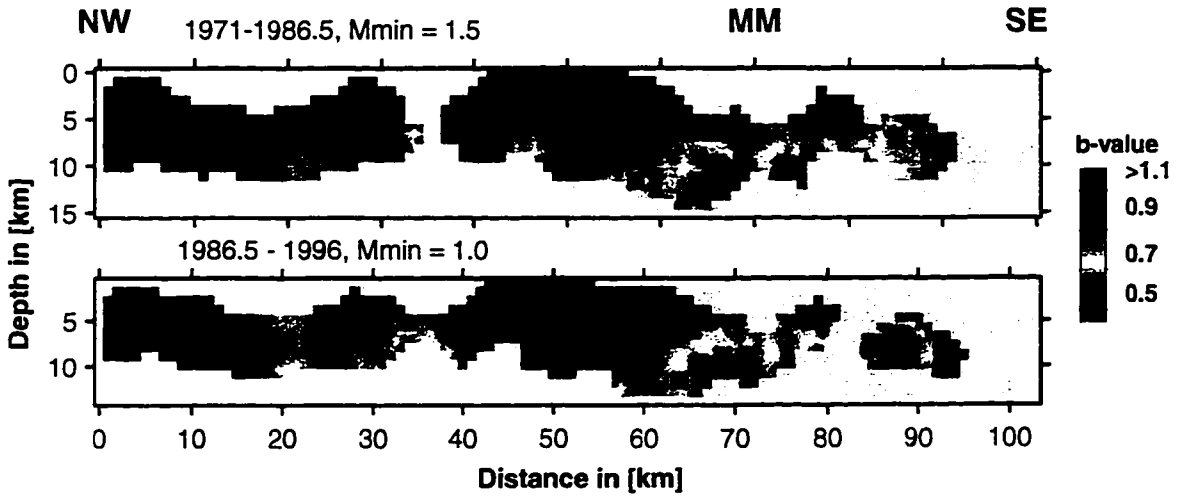

Figure 6.6. *b*-value distribution along strike of the Parkfield segment of the San Andreas fault for two periods: 1971-1986.5 with Mmin = 1.5 (top), and 1986.5-1996 with Mmin = 1.0 (bottom). For the early period, the location of the 1975 M5.1 earthquake north of Middle Mountain is marked.

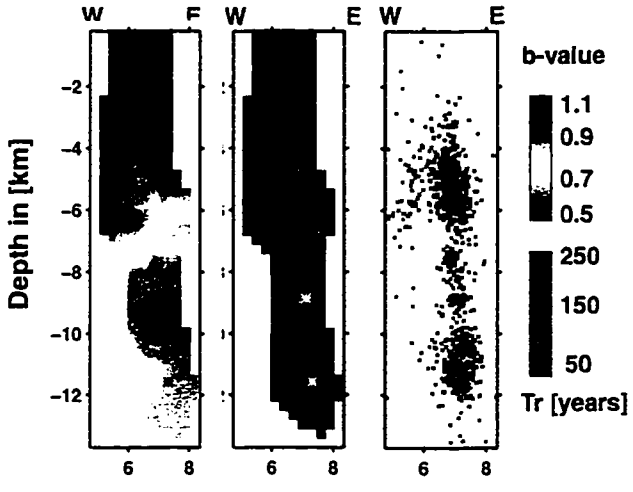

Figure 6.7. Cross-section perpendicular to the San Andreas fault. Right: Hypocenters. Middle: Distribution of *b*-values . Left: Recurrence times for an M6 earthquake, calculated from the *a*- and *b*-values at each node.

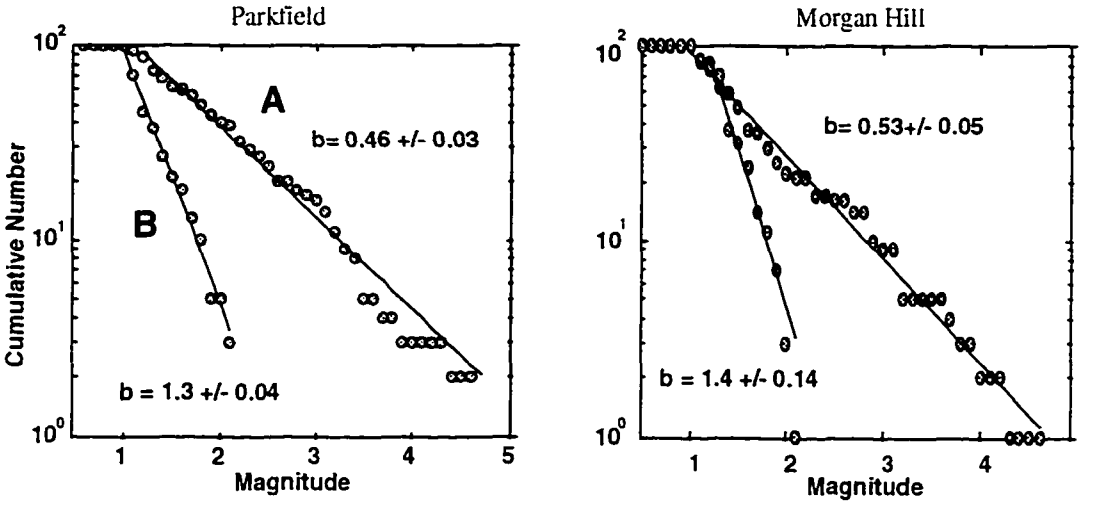

Figure 6.8. Frequency magnitude distribution for two volumes at Parkfield and Morgan Hill, each containing 100 earthquakes. The locations of the volumes from Parkfield (left) are indicated in Figure 6.5a and were chosen to represent populations with high and low *b*-values. The locations of the volumes from Morgan Hill (right) are indicated in Figure 6.10.

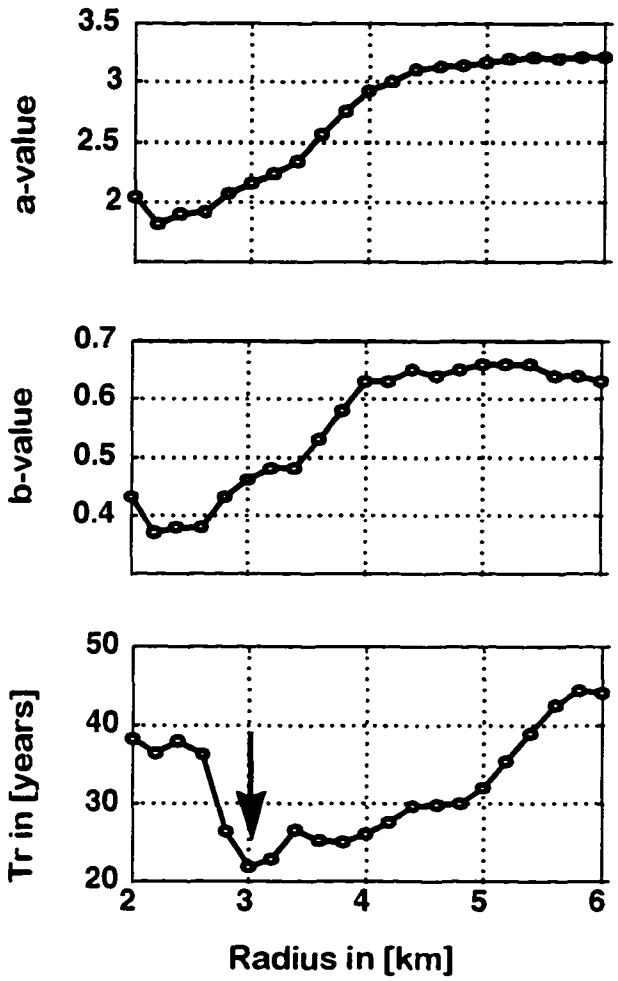

Figure 6.9. *a*-value (top), *b*-value (middle) and recurrence time (bottom)as a function of the radius sampled for the Parkfield asperity.

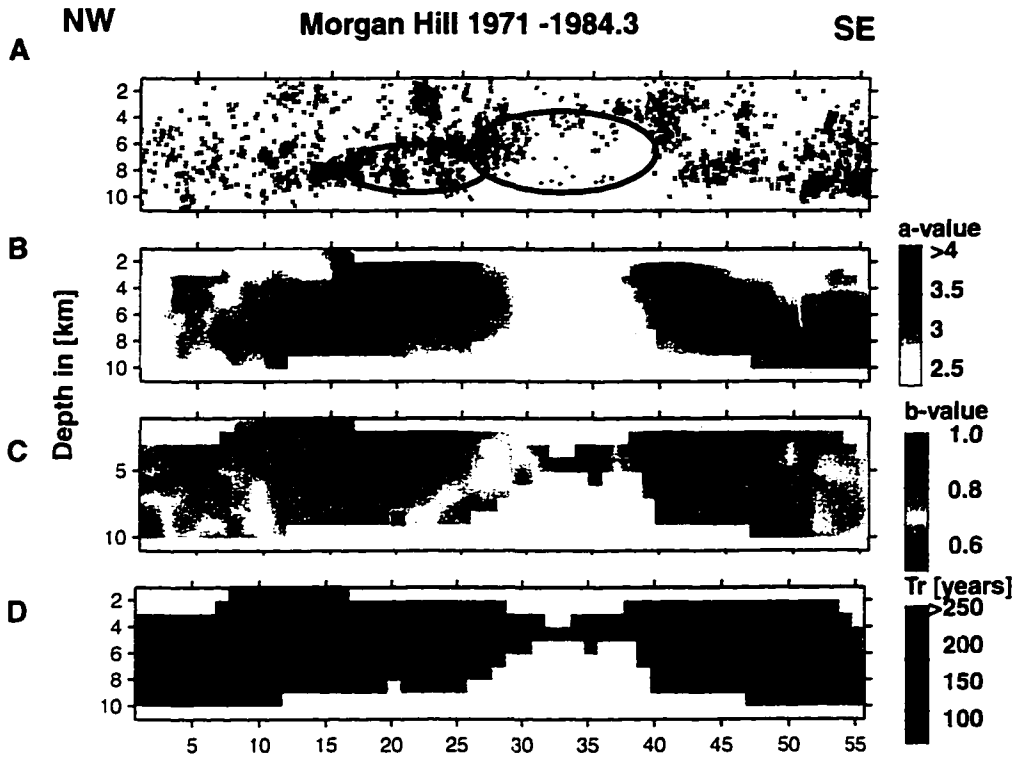

Figure 6.10. Vertical cross-section along strike of the Calaveras fault (a), showing the hypocenters from 1971 - 1984.3. The Morgan Hill main shock location is marked by 'x'. The first two weeks of aftershocks are shown as red symbols, and the two ellipses mark the approximate rupture area [*Bakun et al.*, 1986]. (b) Distribution of b-values along strike. Red colors indicate low b-values, blue high b-values. (c) Distribution of a-values. (d) Recurrence time Tr for an M6 earthquake, calculated from the a- and b-values at each node.

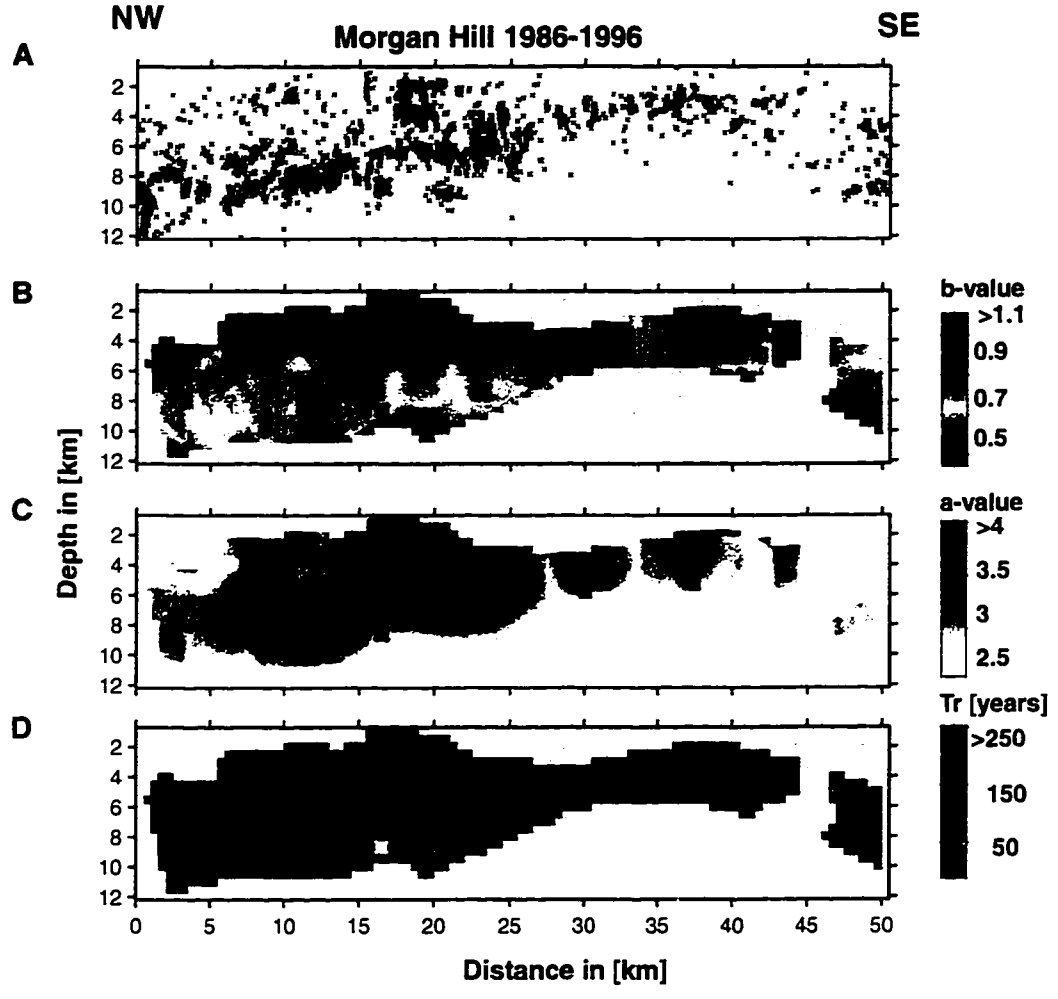

Figure 6.11. Vertical cross-section along strike of the Calaveras fault using the seismicity for the period Jan. 1986 - Jan. 1996. The location of the low *b*-value patch and the location and value for the minimum recurrence time remain stationary.

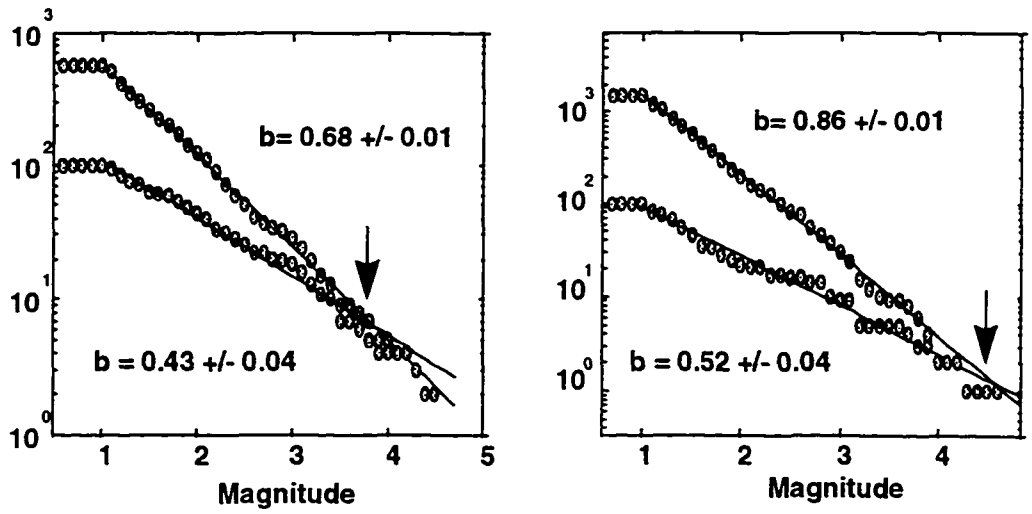

Figure 6.12. Frequency-magnitude relationship for the entire segment of the Parkfield rupture (20 x 15 km) and the asperity only (R = 3 km) (left), and for the entire segment of the Morgan Hill rupture (25 x 12 km) and its asperity (R = 3 km) (right).

Chapter 7. Frequency-Magnitude Characteristics of the Quiescence Anomalies in the Tokyo Region

7.1 Abstract

The analysis of the frequency-magnitude distribution of three current quiescences in the Tokyo region (documented by *Wyss and Wiemer* (1996) suggest that these quiescences may not terminate in ~M6.5 main shocks. This interpretation is based on the hypothesis that the occurrence of a seismic quiescence can be interpreted as a probability gain over the long term poissonian background rate. Due to the high *b*-values observed for all three quiescent volumes ($1.5>b>1.1$) this long term probability is low ($p < 5.\ 10^{-5}$ per year). Although the observed quiescence poses an (unknown) probability gain, it is reasonable to assume that probability for an M6.5 remains small in the quiet areas.

The hypothesis that large events will preferentially occur in low *b*-value volumes is substantiated by the observation that the 1990 M6.5 Izu Oshima earthquake occurred in a low *b*-value region (b~0.5) with a $p = 0.015$ per year poissonian probability for such an event. The largest event in the Tokyo region since 1990 (1996, M5.6) also occurred in a low *b*-value region (b~0.6).

7.2 Introduction

This chapter discusses the frequency-magnitude characteristics of three seismic quiescences in the vicinity of Tokyo, that where documented in a recent paper by *Wyss and Wiemer* (1996). These quiescences, termed the Saitima, Funabashi, and NW Saitima quiescences, are significant in that they potentially could be precursors to a magnitude M = 6.5 +/- 0.5 earthquake in an urban region (*Wyss and Wiemer*, 1996).

In a recent study, *Wiemer and Wyss* (1996) have performed a high resolution study of the frequency-magnitude distribution in fault zones. They found that for two well known asperities in the Parkfield and Morgan Hill areas, the asperities are characterized by anomalously low *b*-values (b~0.5). Based on this observation, *Wiemer and Wyss* (1996) proposed a new model to explain the recurrence time of M6 earthquakes. *Mori and Abercombie* (1996) investigated the dependency of the *b*-value on depth in several regions in California. They found generally a decrease of b with depth, and concluded that an event at depth (thus in a low *b*-value) region has a more than an order

of magnitude greater probability to grow into a large event.

Although no systematic study of the relationship between asperities, *b*-values, and seismic quiescence has ever been performed, a number of unpublished case studies in California and Japan support the following hypothesis:

- Precursory seismic quiescence occurs in, or in close vicinity of, the volumes of high moment release during the mainshock. The asperities, which generate the moment release, are under high stress.
- Asperities are also volumes of low *b*-value. The recurrence time of an earthquake of a given magnitude can be calculated most accurately by using the frequency-magnitude distribution of the events within the asperity. We find that he poissonian probability for a large event is several orders of magnitude higher in low *b*-value volumes than in high *b*-value volumes. This observation is substantiated by the fact that generally the maximum size of the background earthquakes in a high *b*-value region is one to two magnitude units smaller than in low *b*-value regions.
- Consequently, the occurrence of seismic quiescences in low and high *b*-value volumes should be judged differently. Quiescences in high *b*-value volumes are less likely to be within an asperity and less likely to be a precursor to a large event.

A description of the probability P for the occurrence of an earthquake could thus be given in the following way: Let λ_{lt} be the Poisson probability of an earthquake of Magnitude $M>=M_{min}$ per year estimated from the long term rate, and C_q the increase in the probability due to the occurrence of quiescence.

$$p = \lambda_{lt} C_q \qquad \text{(e.q. 7.1)}$$

C_q the probability gain, is an unknown constant ranging from 1 to $1/\lambda_{lt}$, and is likely to be dependent on the degree of quiescence, the tectonic setting, etc. λ_{lt} is a function of "*a*" and "b" (from the Gutenberg-Richter law) and can be calculated using the equation:

$$\lambda_{lt} = 10^{(a-bM)}/dT \quad \text{(e.q. 7.2)}$$

where M is the magnitude of an expected event. Although C_q is unknown, the dependency of λ_{lt} on

"*a*" and "*b*" can be studied for a particular region.

However, an alternative hypothesis is that the probability gain of all seismic quiescences does not depend on "a" or "b". The probability whether or not a specific quiescence is indeed precursory is thus a constant (e.g. 50% for a three-year period, as proposed by *Wyss and Wiemer* (1996)) and independent of the frequency-magnitude distribution. To distinguish between these hypotheses will require a number of high quality case studies, and ultimately a real time test. This chapter will explore the implications for the current quiescences in the Tokyo region under the assumption that equation (1) is valid. Evidence form the Izu-Oshima quiescence case (*Wyss et al.*, 1996) will be used to further confirm the conclusion.

7.3 Data and Results

The catalog used in this study is identical to the one described in *Wyss and Wiemer* (1996). Only night-time events are investigated, using data since 1980. The method used to estimate *b*-values in map view and cross-section has been described in detail in chapters 4 through 6.

The cumulative number plots for the three quiescent volumes are shown in Figure 7.1 and 7.2. Also shown for all three volumes are the frequency-magnitude distributions. Using the *a* and *b*-value derived from the frequency-magnitude plot, the poisson probability for a M=6.5 earthquake can be calculated using equation (7.2). To correct for the fact that only night time events were used, all probabilities are multiplied by a factor 24/12. To simplify the analysis, the 100 closest earthquakes measured from the center of the quiescence anomaly were selected. However, for all three volumes the results were almost identical when selecting a constant radius (for example R =10 km) around each anomaly. Table 7.1 summarizes the results.

1) Saitama volume ($R_{n=100}$ = 11 km): The *b*-value is 1.22 +/- 0.08, which is high compared to the average in this tectonic region (*b*=0.8-1.0). No event with M > 2.5 occurred in this volume over the past 16 years. The poissonian probability for a magnitude 6.5 event is about 7.5×10^{-6} per year.

2) Funabashi volume ($R_{n=100}$ = 9.4 km): The *b*-value is high (*b*=1.13 +/- 0.09). The largest event over the past 16 years was a magnitude 3.8, and the probability for a magnitude 6.5 event in this location is 5×10^{-5} per year.

3) NW Saitama volume ($R_{n=100}$=14 km): The *b*-value is also high (*b*=1.49), the largest event was a M2.6. The probability for a M6.5 event is 1.6×10^{-7} per year.

Table 7.1: *b*-values, *a*-values, and probabilities for a M≥6.5 earthquake per year

	Saitama	Funabashi	NW Saitama	M5.6	Izu-Oshima
b-value	1.22	1.13	1.49	0.72	0.49
a-value	3.7	3.7	4.0	2.8	2.5
P [M>=6.5/ yr]	$7.5\ 10^{-6}$	$5.0\ 10^{-5}$	$1.6\ 10^{-7}$	0.002	0.015
M_{max}	2.5	3.8	2.6	4.8	4.1

In order to test the hypothesis that large events occur in volumes of low *b*-value, the largest event in the study region was investigated (M=5.6, March 1996). Only seismicity prior to this main shock was used. The seismicity was gridded using a 3 km grid spacing, and the 100 closest events with M>= 1.5 were used around each node in order to calculate a *b*-value. This image of the distribution of *b*-values (Figure 7.3) supports the findings for the individual volumes investigated. All three quiescent areas are in red areas, indicating high *b*-values, whereas the 1996 M5.6 event (marked by a 'x') occurred in a low *b*-value (*b*~0.6) region. The frequency magnitude distribution and cumulative number plots of the 100 earthquakes surrounding the hypocenter are shown in Figure 7.2. Using this frequency-magnitude distribution, recurrence times for an event of magnitude M >=5.6 and M>= 6.5 were calculated as 110 yrs and 450 years respectively. Neighboring volumes within this dense cluster of seismicity have recurrence times for a M5.6 event as short as 15-20 years. When selecting a constant radius of 10 km around the event, the recurrence time turns out to be about 35 and 220 years for M5.6 and M6.5 events, respectively.

A comparison of two volumes representing extreme *b*-values is shown in the frequency-magnitude distribution in Figure 7.4. The first volume contains the hypocenter region of the M=5.6 event, and the second volume samples the Saitama seismic quiescence. The frequency-magnitude distributions are clearly different to the eye, and can be distinguished at the 99% confidence limit using *Utsu's* (1992) test.

7.3.1. The Izu-Oshima Case

The seismicity in the vicinity of the 1990 M6.5 Izu-Oshima mainshock has been studied in detail by *Wyss et al.* (1996). Their study revealed the existence of precursory seismic quiescence centered on the hypocenter of the Izu-Oshima event, and lasting for about three years. However, they did not investigate the frequency-magnitude distribution of the seismicity in the region.

Analyzing the seismicity in the vicinity of the Izu-Oshima event is complicated because of a number of volcanic swarms close-by and the lack of a sufficient number of events in the immediate rupture area prior to the main shock. Using the same data-set described by *Wyss et al.* (1996) the frequency-magnitude distribution was analyzed in map view and cross-section. Figure 7.3 shows the frequency-magnitude distribution of the 70 events that occurred within a 5 km wide cross-section centered on the fault plane and during the period 1980-1990. The b-value for this population is low (b~0.5), the a-value is 2.5, and the recurrence time for a magnitude M6.5 event is calculated to be about 70 years (p=0.015 per year). The largest event in this group was a M4.1. The map view of the distribution of b-values (Figure 7.3) shows that indeed the Izu-Oshima event occurred within the area of lowest b-values (b~0.5).

7.4 Conclusions

- The Saitama, Funabashi, and NW Saitama quiescences all occur in high b-value regions (b>1.1) compared to the average of b=0.8 for the region. Based on the Gutenberg Richter model, probabilities for occurrence of an M6.5 event are between 5×10^{-5} and 1.6×10^{-7}. The maximum event size in these volumes for the last 16 years was between 2.5 and 3.8 (night events only).
- No volumes of low b-value that could indicate the existence of highly stressed asperities could be found in map view or cross-section of the currently quiescent volumes.
- The largest earthquake in the studied catalog (M5.6 1996) did occur in a volume of low b-value, thus complying with the hypothesis that low b-value regions have a higher probability for a large earthquake than high b-value regions.

- The Izu-Oshima M6.5 earthquake occurred in a low *b*-value regime. The probability for this event based on the frequency-magnitude distribution of the background seismicity in the rupture area was 0.015 per year.
- The hypothesis that a seismic quiescence represents a probability gain of a large event by a unknown factor *Cq* above the long term background rate was presented. If this hypothesis is assumed to be valid, the likelihood for a magnitude M6.5 +/- 0.5 event in any of the three quiescent volumes is low, due to the extremely low long term probabilities, and the fact that no low *b*-value asperities can be identified.
- To decrease the number of false alarms and to better understand the physics of precursory seismic quiescence, a detailed study of the relationship between frequency-magnitude distribution and seismic quiescence is needed.

7.5 References

Mori J., and R. Abercombie, Depth dependency of earthquakes frequency-magnitude distributions in California: Implications for the rupture initiation, in preparation, 1996.

Utsu, T., On seismicity. In: Report of the Joint Research Institute for Statistical Mathematics. 34, Institute for Statistical Mathematics, Tokyo, 139-157, 1992.

Wiemer, S. and J. Benoit; Mapping the *b*-value anomaly at 100 km depth in the Alaska and New Zealand Subduction Zones, Geophys. Res. Lett., 23, 1557-1560, 1996.

Wiemer, S. and S. McNutt; Mapping the magnitude-frequency distribution in two volcanic regions: Mt. St. Helens (1988-1995) and Mt. Spurr (1991-1995), submitted to Geophys. Res. Lett., 1996.

Wiemer, S., and M. Wyss, Mapping the frequency magnitude distribution in asperities: an improved technique to calculate recurrence times?, submitted to J. Geophys. Res., 1996.

Wyss, M. and S. Wiemer, Two current seismic quiescences within 40 km of Tokyo, Geophys. J. Int., in press, 1996.

Wyss, M., K. Shimazaki, and T. Urabe, Quantitative mapping of a precursory seismic quiescence to the Izu Oshima 1990 (6.5) earthquake, Japan, Geophys. J. Int., in press, 1996.

7.6 Figures

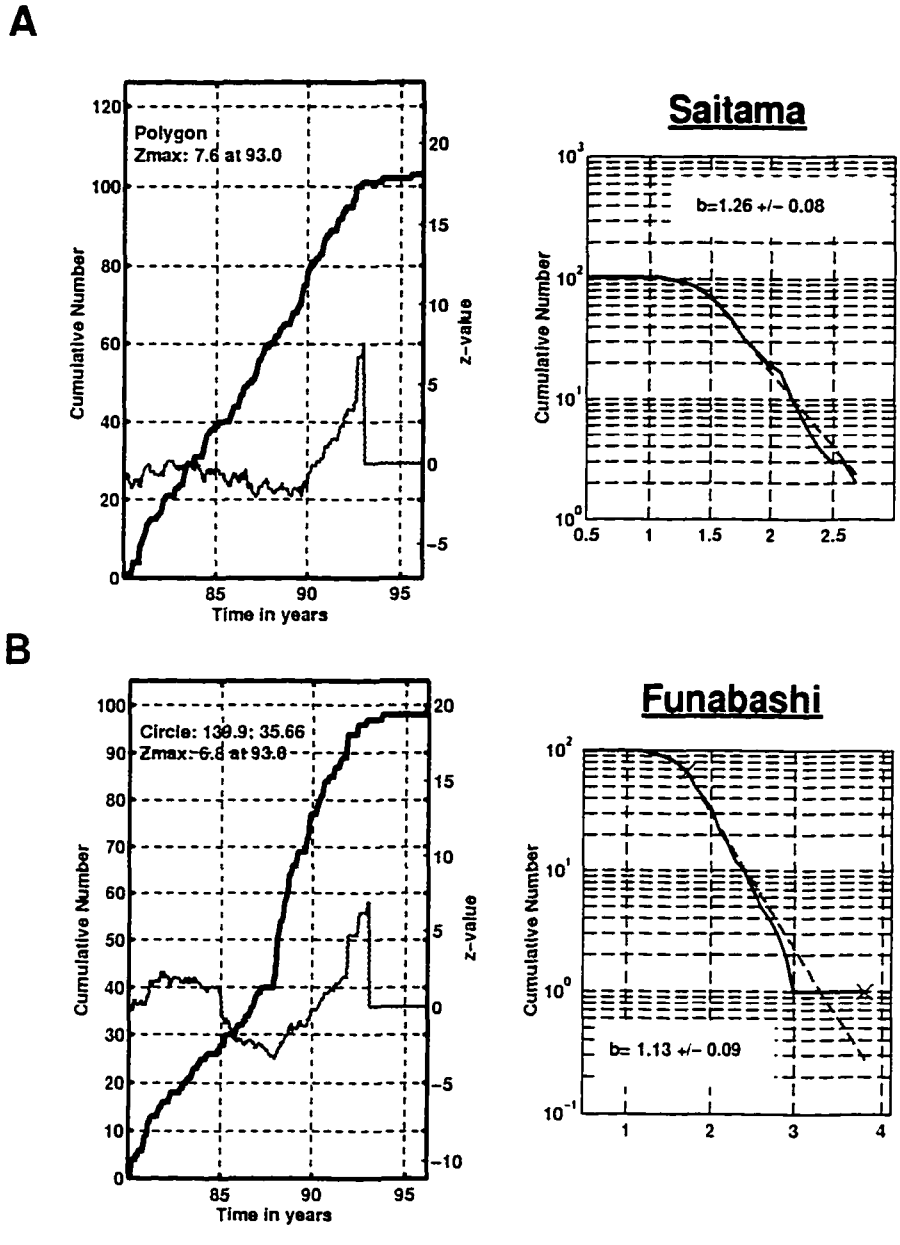

Figure 7.1. Cumulative number of earthquakes for the Saitama volume (A, left) and frequency-magnitude distribution for the same population of events (right). (B) Same for the Funabashi volume.

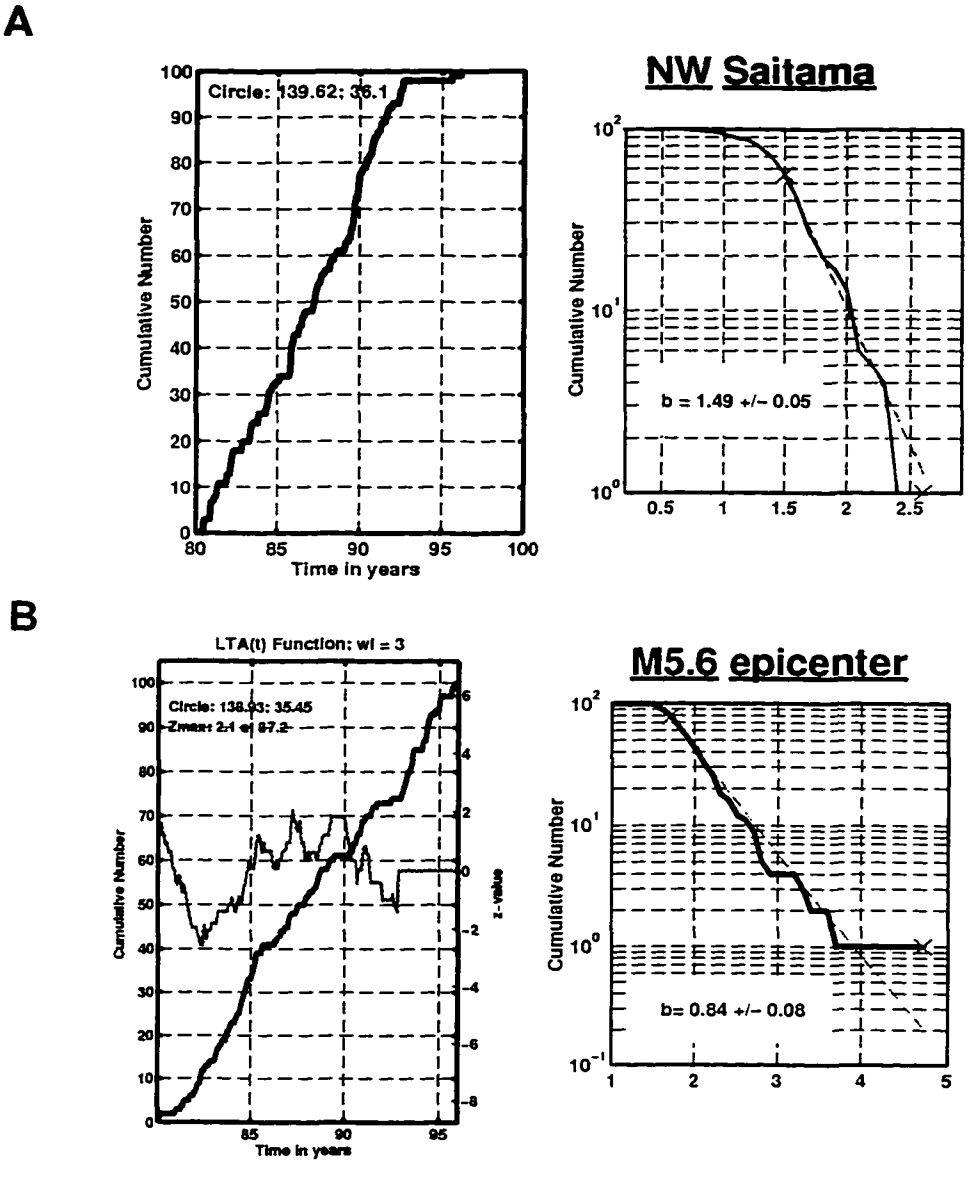

Figure 7.2. Cumulative number of earthquakes for the NW Saitama volume (A left) and frequency-magnitude distribution for the same population of events (right). (B) Same for the seismicity in the vicinity of the largest event in the investigated region (M5.6, 1990).

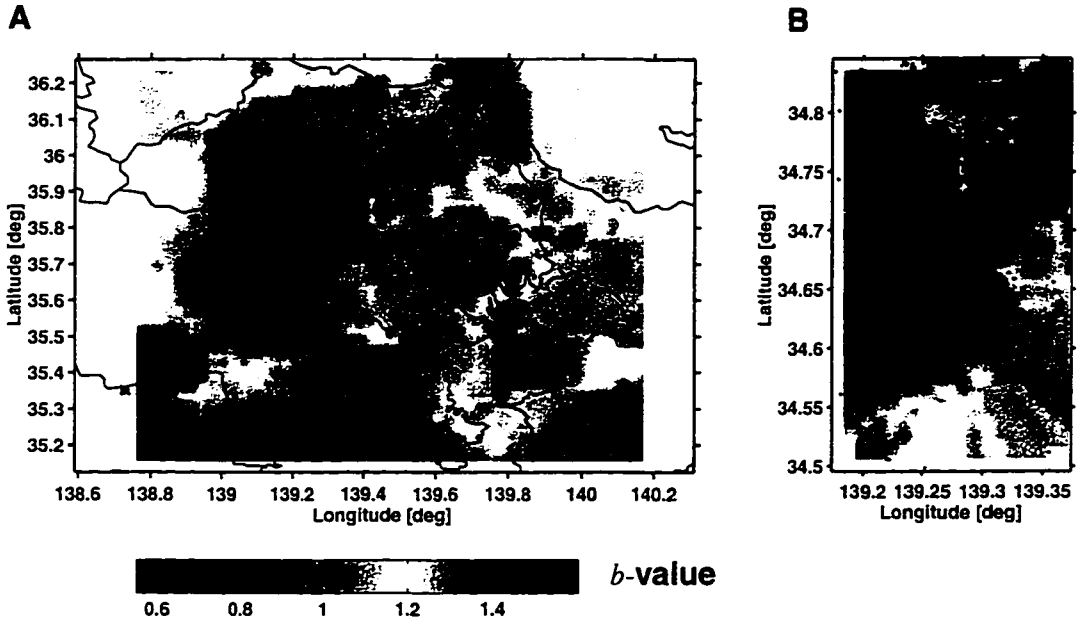

Figure 7.3. *b*-value maps for the Tokyo and Izu-Oshima area. Left: Tokyo, high *b*-values are shown in red, low *b*-value in blue. The seismicity was sampled using a 2 km grid, and the 100 closest events to each grid point were used to estimate the *b*-value. Right: *b*-value map showing the distribution of *b*-values in the Izu-Oshima region. The seismicity was sampled using a 2 km spaced grid, and the 70 closest events to each grid point were used to estimate the *b*-value. The epicenter of the M6.5 Izu Oshima event is marked by a cross.

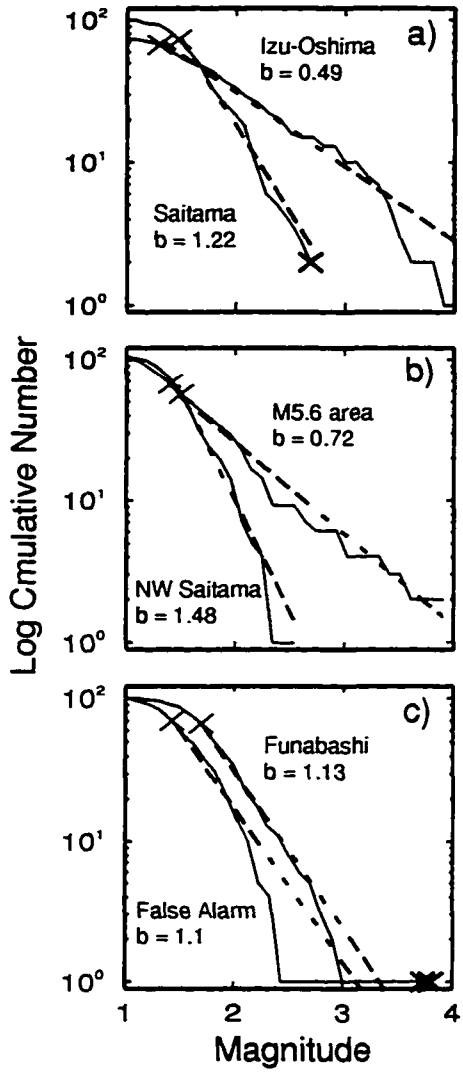

Figure 7.4. Frequency-magnitude distributions for quiescent volumes near Tokyo. (a) Central Saitama compared to Izu-Oshima, (b) NW Saitama compared to the source volume of the largest earthquake in the data set (March 96), (c) Funabashi compared to the false alarm volume near Yokohama (Fig 13 in Wyss and Wiemer, 1996). Map showing the distribution of *b*-values in the Izu-Oshima region. High *b*-values are shown in red, low *b*-value in blue. The seismicity was sampled using a 2 km spaced grid, and the 70 closest events to each grid point were used to estimate the *b*-value. The epicenter of the M6.5 Izu Oshima event is marked by a cross.

Chapter 8. Conclusions

Some seismologists consider seismicity studies based on earthquake catalogs an almost useless enterprise. They suggest that the information which can be deduced from this kind of study has been exhausted since we know the location of the faults and their seismicity rates fairly well by now. Others remark that the errors in location and magnitude are so large that a more detailed analysis cannot reveal much useful information.

However, the results presented in this thesis and other recent studies (*Wyss et al.* 1996ab; *Wyss and Wiemer*, 1996ab) suggest that there continues to be a wealth of valuable information that can be harvested from earthquake catalogs. Through more sophisticated analysis techniques and due to improvements in the quality and quantity of data available, we are today able to study seismicity through innovative ways and in unprecedented detail. Following the development in many other scientific disciplines, visualizing and visually exploring data has become an integral element of seismicity analysis. The combination of gridding techniques and statistical tools makes it possible to map seismicity parameters in an efficient and unbiased fashion in a multi-dimensional space (3-space dimensions, time, and magnitude).

8.1 Precursory Seismic Quiescence and Earthquake Prediction

Does precursory seismic quiescence exist and can this phenomena eventually be used for intermediate-term earthquake prediction? This is an important and still unresolved question in seismology, addressed in detail in chapters 2, 3 and 7. The case studies presented suggest that the answer to this question is more complex than a simple yes or no. There is no question that seismic quiescence exists, but there remains the question if and how it relates to the failure process of large earthquakes. Significant progress in the techniques available to analyze seismic quiescence has been made, as demonstrated in chapters 2, 3, and 7. Using z-value maps (e.g. Figures 2.5 and 3.4) all of space-time for a large region can now be searched for seismicity rate changes. No seismicity rate decrease above a given significance threshold will be missed by the alarm cube method (chapter 3), enabling us to identify all false alarms. By using z-value maps or cross-sections we can now visualize the change in seismicity rate prior to a mainshock in much more detail than previously possible, enabling us to study the behavior of different patches on the fault and correlate these

results with other geophysical parameters such as the moment release or slip during an earthquake (chapter 3). This is important because it allows further constraints of the physical mechanisms causing precursory seismic quiescence. The limited data from a number of earthquakes (Landers [chapter 3], Morgan Hill, Coyote Lake, Adak 1986 [unpublished]) currently points at dilatancy hardening (*Scholz*, 1988) rather then slip softening (*Rudniki*, 1988) as the most likely physical mechanism.

Reasenberg and Matthews (1988) conducted a systematic survey of mainshocks in California, and concluded in their preliminary evaluation of the quiescence hypothesis that precursory seismic quiescence does not precede a significant percentage of mainshocks. They sampled the seismicity in a single circle of 2-25 km radius around each of the epicenters, where the radius depended on the magnitude of the mainshock. However, as presented in this thesis (chapters 2 and 3), we discovered that, when using higher resolution analysis techniques, most of the seismic quiescences show a 80-100% decrease in the center of the anomaly. This almost complete shut-off of the seismicity occurs typically in volumes of 5-10 km diameter or less (Figures 2.7, 2.9, 3.2, and 3.3). Previous analyses using arbitrarily chosen polygons or larger circles centered on the epicenter would not necessarily have been able to identify the center of the anomaly. By sampling a population of earthquakes from both inside and outside the anomaly one would see a less significant rate decrease, or, in the case of a seismicity increase on the outskirts of the anomaly, one would detect no rate change at all. We have also learned to appreciate that quiescence can be limited to certain depth ranges, and only by using cross-section images of the seismicity rate decrease can we separate volumes that do or do not participate in the quiescence. These more sophisticated analysis techniques make it worthwhile to revisit the survey conducted by *Reasenberg and Mathews* (1988) in the near future.

Perhaps the largest obstacle when analyzing seismic quiescence remains artificially introduced changes in the reporting history of earthquake catalogs (*Zúñiga and Wyss*, 1995; *Zúñiga and Wiemer*, 1995; *Habermann*, 1982, 1983, 1986, 1987). Caution and skepticism need to be applied when analyzing seismic quiescence, and investigators need to show that, to the best of their knowledge, the decrease was not caused by a change in the network configuration, the data processing, or other human interference. Investigating the seismicity in all magnitude bands using magnitude signatures (*Habermann*, 1983) allows one to split a seismicity rate decrease into three basic com-

ponents: 1) a rate change (factor); 2) a magnitude shift; and 3) a magnitude stretch (*Zúñiga and Wyss*, 1995). Detailed mapping of the extent of the decrease in space-time might deliver additional clues to identifying artificially introduced rate changes. However, even after all these possibilities have been carefully investigated, one can never entirely rule out that a rate change was caused by humans rather than nature.

Precursory seismic quiescence clearly does not precede all earthquakes, and for many earthquakes we will not be able to detect it given the current level of seismic monitoring. For example, in the case of the Northridge, (California, 1994) and Kobe, (Japan, 1995) events, only a handful of earthquakes occurred on the fault in the 15 years prior to the mainshock, making it virtually impossible to detect a trace of precursory seismic quiescence in the rupture area. (Interestingly, this low seismicity rate makes a lot more sense when one assumes low *b*-values and long recurrences times for the fault, as proposed in chapter 6). Other areas, such as the Aleutian Chain, unfortunately remain poorly monitored. This makes it virtually impossible to detect seismic quiescence. *Kisslinger* (1988) was able to document a unique case of seismic quiescence prior to a large subduction earthquake (the 1986, Mw=8.1 Adak earthquake) by using a regional seismic network. However, this network was removed in 1991, and the current monitoring of earthquakes relies mainly on teleseismic detection with a magnitude of completeness of about M~5. As a result it is now virtually impossible to investigate whether or not seismic quiescence preceded the recent gap-filling event (June 9th 1996, Mw=7.9) in the neighboring segment of the 1986 rupture zone. Because geoscientists, unlike experimental physicists, are forced to wait for nature to perform an experiment, every missed case study is a missed opportunity to advance our understanding of the preparation process to a large earthquake.

Several authors have suggested that precursory seismic quiescence exists for a larger region, hence a decrease in the seismicity rate in a volume several times larger than the fault dimensions (e.g. *Zschau*, 1995). For this pattern it is much more difficult to establish a causal relationship between the mainshock and the observed seismicity decrease. It is also difficult to envision a physical mechanism causing such a regional quiescence. The case studies presented in chapter 2, 3 and 7 focused on a local scale, where the dimensions of the quiescent volume are typically a fraction of the eventual rupture length. However, the analysis techniques presented in this thesis also can be applied to study quiescence regionally.

We have documented in detail a number of case studies of precursory seismic quiescence. The Landers earthquake sequence (chapters 2 and 3; *Wiemer and Wyss*, 1994) provided the first case study of precursory seismic quiescence using these more sophisticated techniques to map out seismic quiescence. Others followed, using data from a variety of seismic networks and tectonic regimes (e.g., *Wyss et al*, 1996; *Wyss and Wiemer*, 1996ab). What is lacking is a more systematic search for all periods of quiescence, covering a large region such as all of northern California, and including a documentation of all successes, false alarms and missed events. For each volume investigated, the quiescence hypothesis will have to be tested against the best estimate of the Poissonian background rate of large earthquakes. The ultimate, truly unbiased evaluation of the seismic quiescence hypothesis will, in my opinion, have to be performed in a real time approach. After three years of software development we now have most of the necessary software implemented to perform such real time testing (chapters 2 and 3; *Wyss and Wiemer*, 1996a,b).

The current seismic quiescences within 20 km of Tokyo, Japan, documented by *Wyss and Wiemer* (1996b; see also chapter 7) illuminate the dilemma that investigators face when analyzing seismicity patterns in real time. The fact that damaging earthquakes can indeed occur in the Tokyo region is well known. The uncertainties (in probability of occurrence, location, magnitude, and time) of a 'prediction' based on the seismic quiescence hypothesis are currently such that the seismic quiescence hypothesis is of only academic interest and clearly of no use for any practical earthquake prediction. For the Tokyo quiescence, *Wyss and Wiemer* (1996b) used the results presented in chapter 7 to conclude that it is unlikely that the observed quiescences are precursors to potentially damaging earthquakes. However, the general public and the media are, of course, immensely interested in any study or 'predictions' of potentially hazardous earthquakes. I believe that denial and secrecy when dealing with the public and media is counterproductive and non-scientific. Seismologists have to choose an extremely cautious and conservative approach when dealing with the sensitive issue of earthquake prediction. It is always tempting to use the public and the media to create additional leverage to ensure continuing funding. Yet unsupported optimism and sensationalism can seriously jeopardize the reputation and credibility of individual scientists and science as a whole. Earthquake prediction has also always been an attractive field for pseudo-scientists, fortune tellers, and charlatans. I consider it as vital to draw a clear distinction between serious scientific studies aimed at understanding precursory phenomena and pseudo-science, and to explain this distinction to the public. Scientists have to enforce a strict regime of self-discipline.

peer review, quantitative analysis, and objectivity - which in the past was not always the case when evaluating precursory phenomena. In this respect the effort made by the IASPEI sub-commission to evaluate precursory phenomena (*Wyss*, 1991) can only be applauded.

The optimism and enthusiasm of the early 1970's, where routine and reliable earthquake prediction seemed only a stone's throw away, has been replaced at least in the USA with pessimism and skepticism. The pendulum of opinions has gone through a full swing. Predicting earthquakes has turned out to be a much more difficult task than scientists had expected in the 1970's, and the more we learn about the complexity of the earthquake failure process, the more we appreciate the difficulty of the task. The non-occurrence of the Parkfield earthquake has further undermined hopes of seismologists. Inspired by chaos theory, fractals, and self similar systems, a number of seismologist believe now that earthquake predictions are inherently impossible, and that no precursory phenomena can be detected. At any given time, any small event can grow into a big one with a certain probability. One can object to this view that indeed many large earthquakes are preceded by fore-shocks, clearly a precursory phenomenon. For California, *Abercombie and Mori* (1996) found that 44% of all earthquakes are preceded by one or more foreshocks. We are currently unable to identify foreshocks as such until the mainshock has actually occurred, but their sheer existence suggests that the segment of the fault which will ultimately rupture in the mainshock does indeed undergo a preparation cycle and 'knows' when it is close to final failure. It is thus not unreasonable to propose that this final stage of the seismic cycle can indeed be detected, and that other precursory phenomena might exist. These precursory phenomena, however, will generally take place at several kilometers depth and thus may be difficult to detect directly at the surface of the earth. This is why seismicity analysis attempts to use the earthquakes in the vicinity of the fault plane as 'stress-indicators', as indirect evidence that the fault is approaching the final stage before a large event.

The last chapter in this thesis, chapter 7, proposes a step towards a multiple-parameter approach to earthquake prediction. The hypothesis that earthquakes preferably occur in low *b*-value regions is presented, and combined with the seismic quiescence hypothesis. The goal is to achieve a more accurate assessment of the probability of an earthquake occurring due to the observation of a seismic quiescence. In the future we hope to be able to take this approach one step further, and factor in the fact that many large earthquakes show foreshocks. Thus the occurrence of a

foreshock like sequence of events within or near a quiescent volume and within a low *b*-value region should indicate the highest possible probability gain over the constant poissonian background rate. In the future, we may find that factoring in other parameters (such as the *p*-value of the foreshock-sequence, the depth of the anomalies, etc.) can provide additional constraints for a more accurate probability assessment.

8.2 Investigating the Frequency-Magnitude Distribution

Studies of the frequency-magnitude distribution have for many cases been controversial. But is most of it just "*much ado about 1.0*" as Frohlich and Davis (1993) provocatively suggested when investigating teleseismic variations in the *b*-value?

Clearly, one has to be careful when investigating the frequency-magnitude distribution. Inherently the slope of the logarithmic frequency-magnitude distribution is a sensitive parameter to measure, and much thought has been given by a number of authors to the correct way to measure *a*, *b* and their confidence limits (*Shi and Bolt*, 1982; *Bender*, 1983). Most likely there have been many studies of the frequency-magnitude distribution that discuss only numerical noise. One has to be cautious not to over-interpret variations. As seen in Figure 6.3, the estimates of the *b*-value can vary up to 30% by chance. Additional complication comes from the fact that unambiguously interpreting the observed variations in the frequency-magnitude distribution is not possible, since several parameters have been shown to impact the slope of the frequency-magnitude distribution.

Yet, despite all these complications, there is little doubt in my mind that variations in the frequency-magnitude distribution can indeed tell us much about the physical properties and environmental conditions in which they occur. The differences in the frequency-magnitude distribution for the different patches on the San Andreas fault are so striking, that they cannot be explained as numerical uncertainties or statistical fluctuations when measuring the slope of the frequency-magnitude distribution. In order to explain these differences as related to systematic problems with the location or magnitude estimation, complex, almost esoteric arguments need to be constructed. The obvious correlation of the lowest *b*-value region and the Parkfield asperity is intriguing. We have argued that elevated stress is the likely cause for the low *b*-values observed. By comparing the *b*-values with the results from stress tensor inversions we hope to be able to support this hypothesis in more detail.

The research presented in chapter 5, 6 and 7 suggest that high resolution studies of the spatial variability of the frequency-magnitude distribution can reveal so far unnoticed features of subduction zones, volcanoes, and faults. Using the imaging capabilities of ZMAP, the heterogeneity of the frequency-magnitude distribution can be studied at a number of different scale lengths. In subduction zones (chapter 5), our method had a resolution of 10-20 km and we could use earthquakes with a magnitude of completeness M_{comp} = 2-3. Along the strike-slip faults of California we study anomalies measuring 1-5 km, using events above M=1. For volcanoes, very dense seismic networks make it possible to study features of sub-km dimension by using events of M > 0.1-0.4. Thus it can be concluded that variability in the frequency-magnitude distribution exists over several scale lengths, mirroring the complexity and heterogeneity of the earth's crust.

It is important to understand the physical causes of the described *b*-value anomalies, including the perturbation of the fractal distribution of rupture lengths. Constraints for models of these perturbations may be found by correlating *b*-value anomalies with differences in other geophysical parameters. For example, under volcanoes we have found that anomalously high *b*-values correlate with the locations of active magma chambers (*Wiemer and McNutt*, 1996; *Wyss et al*, 1996b). For a part of central Japan where a resistivity model derived from magneto-telluric data is available we found some suggestion of correlation of high *b*-values with low-resistivity crust in a preliminary survey (more pervasive fracturing may be the physical explanation of both types of anomalies). Along the San Andreas fault another preliminary investigation suggests that there may exist a correlation with the orientation of the stress tensor (derived by inversion from focal mechanisms) and with Vp/Vs anomalies. High quality data sets recorded under controlled conditions such as in mines need to be investigated to put further constraint on the physical mechanism causing the variability in the frequency-magnitude distribution.

8.3 References

Abercombie and Mori (1996). Occurrence patterns of foreshocks to large earthquakes in the western United States, Nature, 381, 303-307.

Bender, B. (1983). Maximum likelihood estimation of b-values for magnitude grouped data, Bull. Seism. Soc. Am., 73, 831-851.

Gephart, J.W., and D.W. Fortyth (1984). An improved method for determining the regional stress tensor using earthquake focal mechanism: application to the San Fernando earthquake sequence, J. Geophys. Res., 9305-9320.

Habermann, R.E. (1982). Consistency of teleseismic reporting since 1963, Bull. Seism. Soc. Am. 72, 93-112.

Habermann, R.E. (1983). Teleseismic detection in the Aleutian Islands arc, J. Geophys. Res., 88, 5056-5064.

Habermann, R.E. (1986). A test of two techniques for recognizing systematic errors in magnitude estimates using data from Parkfield, California, Bull. Seism. Soc. Am., 76, 1660-1667.

Habermann, R.E. (1987). Man-made changes of seismicity rates, Bull. Seism. Soc. Am., 77, 141-159.

Frohlich, C., and S. Davis (1993). Teleseismic b-values: or, much ado about 1.0, J. Geophys. Res., 98, 631-644.

Kisslinger, C. (1988). An experiment in earthquake prediction and the 7 May 1986 Andreanof Islands earthquake, Bull. Seism. Soc. Am., 78, 218-229.

Scholz, C.M. (1988). Mechanism of seismic quiescence, PAGEOPH, 126, 701-707.

Shi, Y., and B. Bolt (1982). The standard error of the magnitude frequency b value, Bull. Seism. Soc. Am., 72, 1677-1687.

Reasenberg, P.A., and M.V. Matthews (1988). Precursory seismic quiescence: A preliminary assessment of the hypothesis, PAGEOPH, 126, 373-406.

Rudnicki, J.W. (1988). Physical Models of earthquake instability and precursory processes, PAGEOPH, 126, 531-554.

Wesnousky, S. G. (1994). The Gutenberg-Richter or characteristic earthquake distribution, which is it?, Bull. Seism. Soc. Am., 84, 1940-1959.

Wiemer, S., and J. Benoit (1996). Mapping the b-value anomaly at 100 km depth in the Alaska and New Zealand subduction zones, Geophys. Res. Lett., 23, 1557-1560.

Wiemer, S., and S. McNutt (1996). Variations in the magnitude-frequency distribution in two volcanic regions: Mt. St. Helens (Washington) and Mt. Spurr (Alaska), submitted to Geophys. Res. Lett..

Wiemer, S., and R. F. Zúñiga (1994). ZMAP - a software package to analyze seismicity, Supplement to EOS, Transactions, Fall Meeting, AGU, 75, 456.

Wiemer, S. and M. Wyss (1996). Mapping the frequency magnitude distribution in asperities: an improved technique to calculate recurrence times?, submitted to J. Geophys. Res.

Wiemer, S. and M. Wyss (1994). "Precursory seismic quiescence", Supplement to EOS, Transactions, AGU, 75, 44, 454.

Wyss, M. (1991). Evaluation of Proposed Earthquake Precursors, Edited by M. Wyss, Published by AGU in cooperation with IASPEI. Special Publication, 94 pages.

Wyss, M. and S. Wiemer (1996a). Two Precursory Seismic Quiescences near Priest Valley, California, Bull. Seism. Soc. Am., in press.

Wyss, M. and S. Wiemer (1996b). Two current seismic quiescences within 40 km of Tokyo, Geophys. J. Int., in press.

Wyss, M., K. Shimazaki, and S. Wiemer (1996a). Mapping active magma chambers by b-values, J. Geophys. Res., 101, in preparation.

Wyss, M., S. Wiemer, and S. Tsuboi (1996b). Magnitude distribution anomalies in the WBZ beneath Japan, J. Geophys. Res., in preparation.

Zschau, J. (1995). SEISMOLAP: A quantification of seismic quiescence and clustering, IUGG. XX1 General Assembly, Abstracts. A, A389.

Zúñiga, R., and M. Wyss (1995). Inadvertent changes in magnitude reported in earthquake catalogs: Influence on b-value estimates, Bull. Seism. Soc. Am., 85, 1858-1866.

Zúñiga, F.R. and S. Wiemer (1995). Variaciones artificiales de sismicidad y su aplicación. Algunos ejemplos en México. In "La Sismologia en México", Monograph No.2, Unión Geofisica Mexicana. F. Medina, G. Suarez and L. Delgado, editors, pp 100-110.

Appendix A: The Seismicity Analysis Software ZMAP

A.1 What is ZMAP?

One of the most valuable products of this thesis is the software developed while studying seismicity. This software has been bundled into a package, ZMAP, that enables the user to interactively perform a number of standard and innovative tasks to investigate seismicity. The capabilities of ZMAP are described in some detail below. By making ZMAP available to interested scientists via anonymous ftp, we ensure that other research groups can benefit from our software development and at the same time re-evaluate our analysis. We have also written a 100 page users-guide, that is available either as a post-script file or HTML document.

One main application of ZMAP is the study of the seismic quiescence hypothesis. ZMAP is a tool uniquely suited to detect seismicity rate changes prior to major earthquakes - either after the fact or applied in 'real time'. ZMAP identifies seismicity rate changes in earthquake catalogs and helps also to investigate the characteristics of changes.

ZMAP can be used to investigate or monitor the health of a seismic network. The user can address questions like: Did the detection threshold change in a particular area for a certain time? Did the meaning of magnitude change? A long list of artificial changes in earthquake catalogs has by now been documented (e.g. *Habermann* 1983, 1987, 1991; *Wyss*, 1991). These artificial changes of the reporting rate can be introduced by modifications to the network configuration, the software or hardware used, the calibration of seismic stations, etc.. Artificial changes can either mask natural changes in the seismicity or, worse, be misinterpreted as natural changes. Using magnitude signatures and *b*-value curves, one can attempt to unravel the reporting history of earthquake catalogs.

Here, in a nutshell, is a list of features that ZMAP provides:

- Display of standard plots such as maps, cross-sections, time-series, time-magnitude, time depth, 3-dimensional view of the seismicity, histograms (Figure A.1).

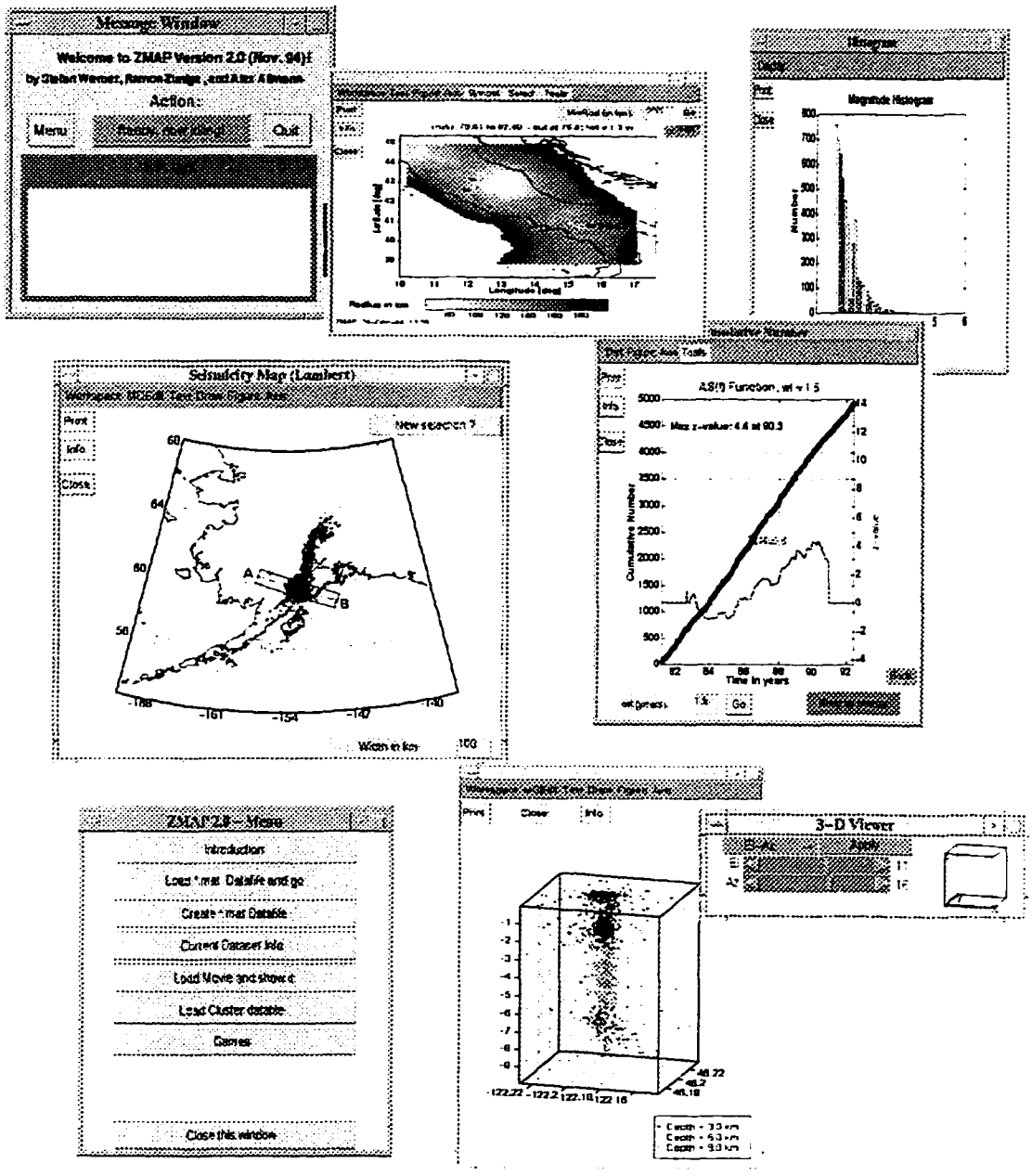

Figure A.1. A number of example windows of ZMAP

- Interactive event selection in polygons of any shape.

- Separation of the dependent and the independent part of the seismicity (declustering), based on *Reasenberg's* (1985) algorithm. The properties of the clusters, such as the *b*- and *p*-val-

ues, histograms, rate changes) can be investigated for individual clusters as well as groups of clusters.

- Evaluation of seismicity rate changes as a function of space and time, using maps, cross-sections, or movies of the standard deviate z. The standard deviate z describes the significance of a rate change (Figure A.2).

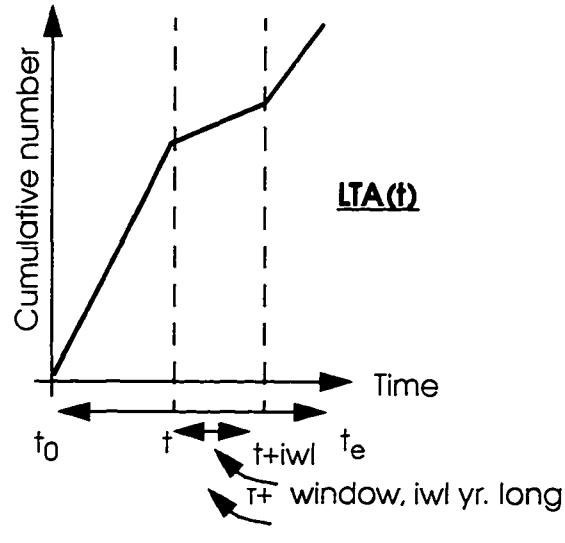

Figure A.2. Schematic explanation of the LTA function

- Identification of all occurrences of seismicity patterns in space time by using alarm cubes. An alarm is declared when a specified pattern (for example a seismic quiescence) has been identified at a certain significance level (Figure A.3)

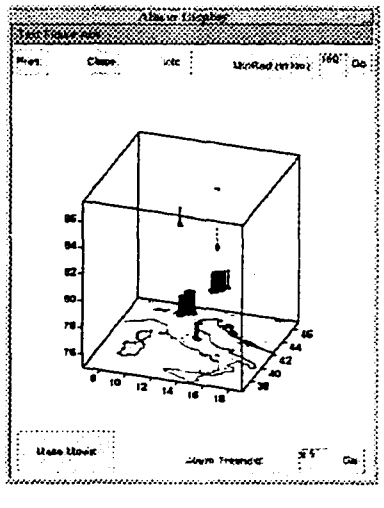

Figure A.3. Alarm cube for Italy

- Evaluation of the significance of a seismic quiescence as compared to the randomized catalog or under the assumption of a Poissonian seismicity distribution.

- Enables the user to study the characteristic of the frequency-magnitude distribution of events in space and time. Maps, cross-sections, and a number of space-time projections of the *b*-value can be computed. The *b*-value and its confidence limits are estimated using both a weighted least squares and maximum likelihood method. The magnitude of completeness can also be analyzed spatially.

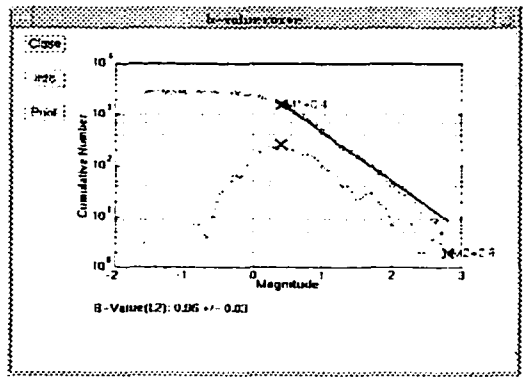

Figure A.4. Example of the frequency-magnitude distribution. •

- Evaluation of the confidence limits of the a and *b*-value estimates as a function of sample size.

- Interactive estimation of the p-value of an aftershock sequence from Omori's law.

- Calculation of the recurrence time for a magnitude M event from the frequency-magnitude distribution.

- Investigation of the properties of seismicity rate changes using magnitude signatures and GENAS (first introduced by *Habermann*, 1983). This approach evaluates seismicity rate changes in different magnitude bands. Magnitude shifts, stretches, and rate changes can be identified and modeled.

- Performs a time to failure analysis based on accelerated moment release. *Varnes* (1989) and

Bufe et al. (1993) suggested that the moment release accelerates in the 10-20 years prior to a major earthquake.

- Inverts for the stress direction using *Gephart's* (1984) algorithm. Using fault plane solutions the principal stress directions and their 95% confidence limits can be calculated for an interactively selected subset of data. In addition, the implementation of the cumulative misfit method by *Lu and Wyss* (1996) allows the identification of regions with a homogeneous stress direction. Maps or cross-sections of the cumulative misfit and the stress tensor directions can be displayed (UNIX version only).

In addition, ZMAP features:

- Built in on-line help (Figure A.5), HTML users guide, and a 100 page manual.

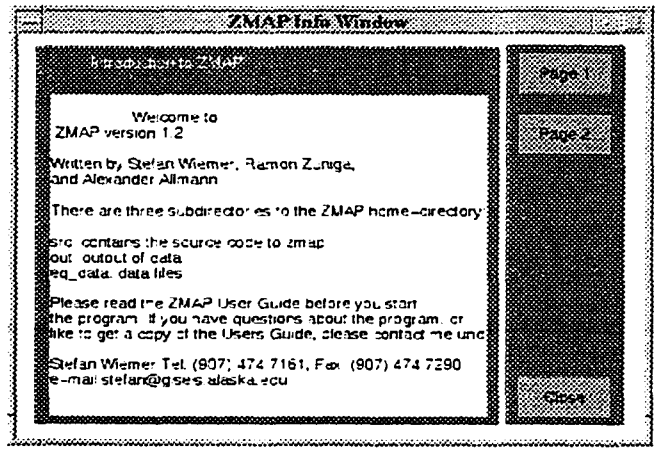

Figure A.5. Example window showing the on-line help available.

- User friendly, interactive interface (Figure A.6)

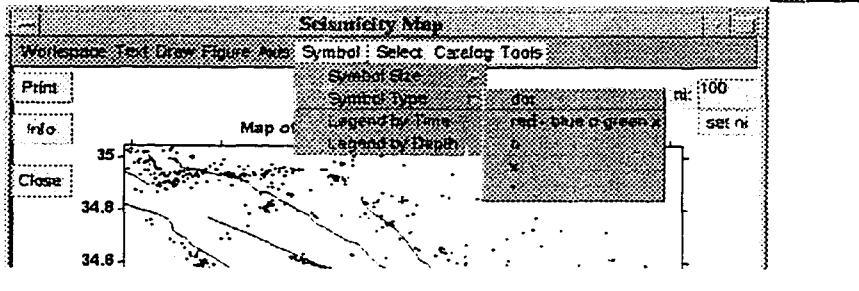

Figure A.6. Example window showing the pull-down menu capability of ZMAP.

- Open system architecture, making it easy to add new components without having to re-compile the entire program.
- Automatic downloading of the latest version via anonymous ftp.
- Graphics output in many different formats.
- Data import from a number of catalogs formats (Hypoinverse, Hypoellipse)

A.2 HTML Users Guide

This Users Guide is distributed as a postscript file and as a HTML document. You can point your web browser (such as Mosaic) to the file <zmaphome>/wwwdoc/wmworks/www/ug.book_1.html and you should be able to browse through the Users Guide. This allows fast access, saves paper, and shows all the figures in color.

A.3 Obtaining ZMAP

ZMAP is freeware and available for a number of operating systems (UNIX, PC, MAC). As mentioned above, ZMAP is a collection of MATLAB scriptfiles, and you do need a version of MATLAB (4.1 or higher) to run ZMAP. The latest version of ZMAP and the Users Guide can be obtained via anonymous ftp:

ftp eq.giseis.alaska.edu
password: anonymous

To get the **UNIX** version as a compressed tar file type

cd pub/zmap/unix
binary
get zmap.tar.Z
get manual.tar.Z

To get the **PC** or Macintosh version as a compressed zip file:

cd pub/zmap/pc
binary
prompt off
*mget **

Read the file install.txt to find out how to install ZMAP. If you don't have access to ftp, send fax or e-mail to Stefan Wiemer, stefan@giseis.alaska.edu, fax (907) 479 7290. I will mail you a floppy or CD with the source code and a hardcopy of the UsersGuide.

A.4 Sample Data

You can also retrieve a number of sample data sets via ftp. Log in via anonymous ftp as described above and cd into the directory pub/zmap/data. Set the file type to binary. There will be a list of data sets in this directory, among them:

- landers.mat: Seismicity prior to the Landers and Big Bear earthquake (see *Wiemer and Wyss*, 1994)
- red8995.mat: Seismicity in the vicinity of Redoubt, Alaska. This time-period includes all of the 89-90 eruptions. Only VT events are listed.
- ak8994.mat: AEIC earthquake catalog for Alaska.

A.5 References

Bufe, C. G., Nishenko, S. P., and Varnes, D. J. (1994). Seismicity Trends and Potential for Large Earthquakes in the Alaska-Aleutian Region, PAGEOPH. V, 142, 83-99.

Gephart, J.W., and D.W. Fortyth (1984). An improved method for determining the regional stress tensor using earthquake focal mechanism: application to the San Fernando earthquake sequence, J. Geophys. Res., 9305-9320.

Habermann, R.E. (1982). Consistency of teleseismic reporting since 1963, Bull. Seism. Soc. Am, 72, 93-112.

Habermann, R.E. (1983). Teleseismic detection in the Aleutian Islands arc, J. Geophys. Res., 88, 5056-5064.

Habermann, R.E. (1987). Man-made changes of seismicity rates, Bull. Seism. Soc. Am., 77, 141-159.

Habermann, R.E. (1991). Seismicity rate variations and systematic changes in magnitudes in teleseismic catalogs, Tectonophysics, 193, 277-289.

Lu, Z., and M. Wyss (1996). Segmentation of the Aleutian plate boundary derived from stress direction estimates on fault plane solutions, J. Geophys. Res., 101, 803-816.

Reasenberg, P.A., and M.V. Matthews (1988). Precursory seismic quiescence: A preliminary assessment of the hypothesis, PAGEOPH, 126, 373-406.

Varnes, D.J. (1989). Predicting earthquakes by analysing accelerating precusory seismic activity, PAGEOPH, 134, 661-686.

Wyss, M. (1991). Reporting history of the central Aleutians seismograph network and the quiescence preceding the 1986 Andreanof Island earthquake. Bull. Seism. Soc. Am., 81, 1231-1254.